LIGHTNING-INDUCED COUPLING OF THE RADIATION BELTS TO GEOMAGNETICALLY CONJUGATE IONOSPHERIC REGIONS

William Cargill Burgess

March, 1993

LIGHTNING-INDUCED COUPLING OF THE RADIATION BELTS TO GEOMAGNETICALLY CONJUGATE IONOSPHERIC REGIONS

A DISSERTATION
SUBMITTED TO THE DEPARTMENT OF ELECTRICAL ENGINEERING
AND THE COMMITTEE ON GRADUATE STUDIES
OF STANFORD UNIVERSITY
IN PARTIAL FULFILLMENT OF THE REQUIREMENTS
FOR THE DEGREE OF
DOCTOR OF PHILOSOPHY

By
William Cargill Burgess
March, 1993

I certify that I have read this dissertation and that in my opinion it is fully adequate, in scope and quality, as a dissertation for the degree of Doctor of Philosophy.

Umran S. Inan (Principal Advisor)

I certify that I have read this dissertation and that in my opinion it is fully adequate, in scope and quality, as a dissertation for the degree of Doctor of Philosophy.

Robert A. Helliwell

I certify that I have read this dissertation and that in my opinion it is fully adequate, in scope and quality, as a dissertation for the degree of Doctor of Philosophy.

Thomas M. Cover

Approved for the University Committee on Graduate Studies:

This dissertation is dedicated to my mother and father

Clotilde Frances *and* John Cargill Burgess

and to my grandmother

Helen Lenox Burgess

Abstract

Very-low-frequency (VLF) radio observations in Antarctica and North America provide the first evidence that bursts of energetic electrons from the Earth's radiation belts commonly precipitate into geomagnetically conjugate ionospheric regions in response to lightning. The electrons, with energies ranging from tens of keV to over one MeV, appear to be scattered out of their otherwise stable trap in the Earth's magnetic field by magnetospheric interactions with a regularly observed class of transient, lightning-generated VLF radio waves known as ducted whistlers. The precipitating electrons ionize atmospheric molecules at altitudes between 40 and 90 km, creating transient enhancements of ionization levels in conjugate locations. These ionospheric disturbances can be detected by their characteristic perturbations, sometimes called "Trimpi events," of the amplitude and phase of VLF transmitter signals propagating subionospherically within 200–250 km of the disturbed areas. The first detailed, one-to-one comparison of such signal perturbations, monitored in conjugate regions, with the multipath structure, arrival azimuths, and predicted electron scattering of simultaneously observed ducted whistlers suggests that every ducted whistler precipitates bursts of radiation belt electrons. If so, the estimated rate at which ducted whistlers contribute to radiation belt losses is comparable to that predicted for plasmaspheric hiss, a different class of magnetospheric wave that is often considered to control the structure of the belts. Lightning could therefore play a significant role in the maintenance of radiation belt equilibrium.

Preface

It was from stacks of National Geographics, preserved in my parents' home, that I learned an aspiration to discover the Earth for myself, not just as a tourist, but as an explorer. So much was in that magazine, though, that it sometimes seemed there might be nothing new left to discover, that every nook and cranny of our planet had already been combed for knowledge. But gradually, as I read further, the existence of new places and ways to explore became clear; and of all these modern explorations, none captured my spirit and imagination more than that of Antarctica [*Matthews*, 1971].

So the desire struck, at the age of eight, to join the modern explorers and to visit and work in the Antarctic. For many years to follow, these hopes, which in moments of conformity I dismissed as whimsical, lay dormant. Now, whimsical or not, they are fulfilled! Yet, while I feel very lucky to have lived the stuff of my childhood wonder, it would have been impossible without the guidance and support of some exceptional people.

My thesis advisor, Umran Inan, has been irrepressibly energetic, enthusiastic and positive. He showed me the challenges and rewards of modern geophysics and demonstrated the power of optimism over pessimism. His encouragement and excitement gave me confidence to accomplish this work and to report it in front of scientific audiences from San Francisco to Vienna.

Discussions were always heartening and illuminating with Bob Helliwell, my associate advisor who showed me the benefits of brainstorming; with Don Carpenter, whose interest

helped propel this research; and with Ron Bracewell, whose good cheer and joy in scientific prospecting was infectious. Martin Walt of Lockheed kindly and generously went out of his way to counsel me on this work, and offered me an invaluable “outside perspective.” Tim Bell, Tony Fraser-Smith and Vikas Sonwalkar were quick to advise and encourage when I needed help. In the office, Gayle Walker, Jenny Xu, June Wang and the late Norissa Leger gladly assisted with administrative legwork.

Learning experimental engineering and field techniques at the bench of Bill Trabucco has been a constant pleasure. Bill’s experienced support for my Antarctic missions contributed immeasurably to their success, and his sense of tact and humor was a model for thriving in the lab as well as in the field; I will never forget how his fast work with signal generators one lunchtime set me to laughing all day (at the expense of a painter’s sanity). Others who made the applied aspects of this research a delight include Jerry Yarbrough, whose signal processing talents helped me out of many a jam; Ev Paschal and Mike Dermedziew, who always had time for a neophyte learning the ropes; and John Katsufrakis, who made it clear to me that I belonged.

My fellow graduate students during my time at Stanford have moved and impressed me with their good-heartedness and capability, and it has been a great pleasure to have had such fine people as contemporaries. In particular I would like to thank Dave Shafer, who steadied me during my first Antarctic voyage with its inevitable mixture of surprise, disappointment and awe; Juan Rodriguez, whose reassuring comments during our research and articulate companionship during our British excursion made both more rewarding; everyone responsible for the *I.n.C.* party; and my longtime officemate Lee Poulsen, with whom conversation was ever a joy.

The support of those close to me has been a treasured source of strength, energy, and renewed determination. The generous spirit of friends, too many to list here, who have remembered me despite my troglodytic tendencies during the last few years humbles and honors me. The contribution of my family is beyond words; I cannot imagine this work

or indeed my life being the same without the love of my grandmother Helen Burgess, my sister Elizabeth, my brother John, and of my mother and father Frances and John Burgess.

William C. Burgess

Menlo Park, California
March 9, 1993

This research was made possible by the people of the United States through the sponsorship of the Polar Programs Division of the National Science Foundation under grant DPP-9020687. Data acquisition was supported at Huntsville and at Lake Mistissini by the Atmospheric Sciences Division of the National Science Foundation under grant ATM-9113012, and at Arecibo by the Office of Naval Research under grant N00014-82-K-0489. Construction and installation of the Huntsville observatory was accomplished with the support of the National Aeronautics and Space Administration under grant NAG8-778.

Contents

Tables

Illustrations

1

Introduction

In spite of over thirty years of research, the processes by which the Earth's radiation belts gain and lose their constituent particles are still not well understood. This dissertation examines the contribution of one particular loss process, the precipitation of belt electrons due to scattering by a class of lightning-generated magnetospheric radio waves known as "ducted whistlers." This chapter introduces the phenomena of whistlers and lightning-induced electron precipitation, explains the radio remote sensing techniques used here to study them, and discusses the contributions and applications of this research.

The reader unfamiliar with ionospheric and magnetospheric physics will find it beneficial to review the background information in Chapter 2 before continuing. The abbreviations MF, LF, VLF and ELF, used throughout this work, stand for Medium-, Low-, Very-Low-, and Extreme-Low-Frequency and designate radio frequency bands which are defined in Table 1.1 [*Wave Propagation Standards Committee*, 1977].

1.1 SCIENTIFIC CONTEXT OF THIS RESEARCH

The naturally-occurring radio signal known as the "whistling atmospheric" or *whistler* has intrigued radio engineers and scientists for over seventy years [*Helliwell*, 1965]. Most of the electromagnetic band occupied by whistlers is in the audio frequency range (Figure 1.1), a coincidence responsible for their early discovery as descending, "whistling" tones on radio

TABLE 1.1. Selected radio frequency band designations.

Band	Frequencies (kHz)	Free Space Wavelengths (km)
ELF	3 Hz–3	100 Mm–100
VLF	3–30	100–10
LF	30–300	10–1
MF	300–3 MHz	1–100 m

and telephone equipment. *Storey* [1953] explained whistlers as radio impulses generated by lightning, called *radio atmospherics* or often simply *sferics,* which had dispersed in frequency as a result of propagation through the magnetized plasma of the inner magnetosphere. Subsequent investigations showed that whistlers observed on the ground appear to have been guided along geomagnetic field lines by duct-like magnetospheric structures (Figure 1.2), thought to be localized, field-aligned enhancements of background plasma density [*Helliwell*, 1965]. Ground-observed whistlers are therefore often referred to as *ducted whistlers* to distinguish them from *nonducted whistlers* [*Edgar*, 1976] and other magnetospheric radio waves which are neither constrained to follow field lines nor observed except on spacecraft. Chapter 2 discusses atmospherics, whistlers and whistler ducts in greater detail.

In 1963, at Eights Station, Antarctica, a Stanford engineer named Michael Trimpi discovered that characteristic fluctuations in the reception of a VLF signal from a Navy transmitter in Maryland occurred at the same time as observed whistlers [*Baum*, 1963]. These perturbations of the signal's amplitude were characterized by a sudden onset and a roughly exponential recovery lasting about one minute. Similar fluctuations (Figure 1.3) were later seen on both the amplitude and phase of several subionospheric VLF, LF, and MF signals

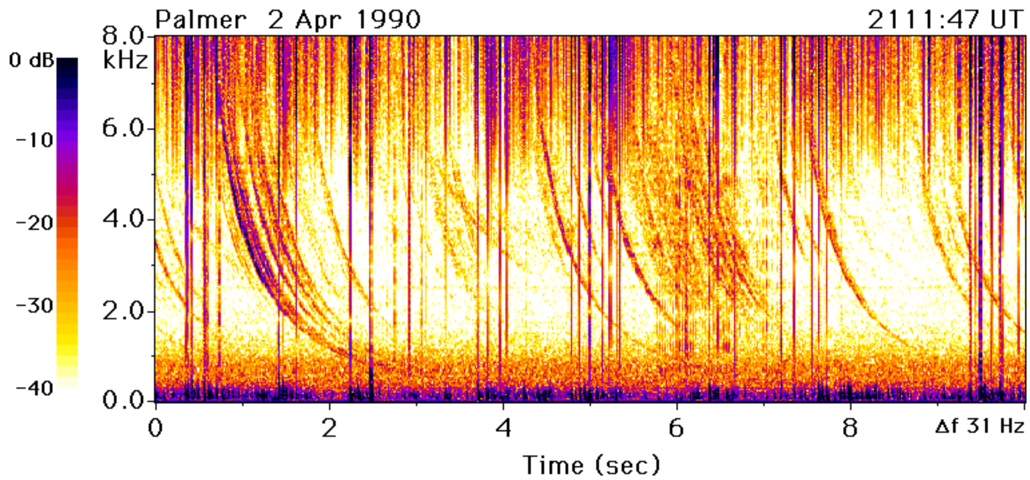

Fig. 1.1. Whistlers observed at Palmer Station, Antarctica. Because the frequencies of these natural radio signals are in the audio range, their descending, "whistling" tones can be heard with equipment as simple as a loop antenna, an audio amplifier and a speaker. The whistler occurrence rate at Palmer Station during the period shown peaked near 200 per minute. The impulsive signals which appear as vertical lines are "atmospherics" (or "sferics") radiated by lightning flashes located around the Earth.

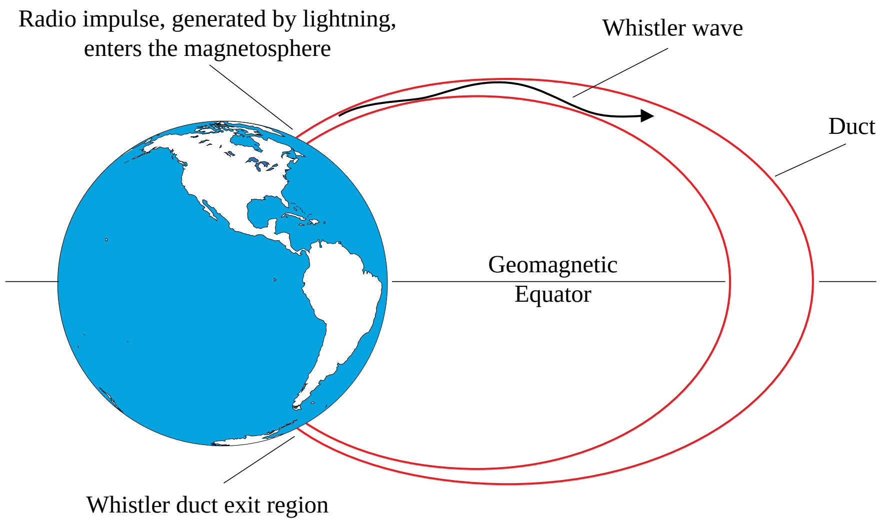

Fig. 1.2. Ducted whistler propagation. A whistler begins propagation as a radio atmospheric impulse generated by lightning. This signal becomes trapped in a tube or "duct" of enhanced electron density aligned with the geomagnetic field. The impulse is dispersed in frequency while propagating in the duct, thus appearing to a ground observer near the exit region as a descending tone. The hypothetical duct shown has been exaggerated in size for clarity; actual ducts are thought to be 200–500 km in diameter in the equatorial plane [*Angerami*, 1970].

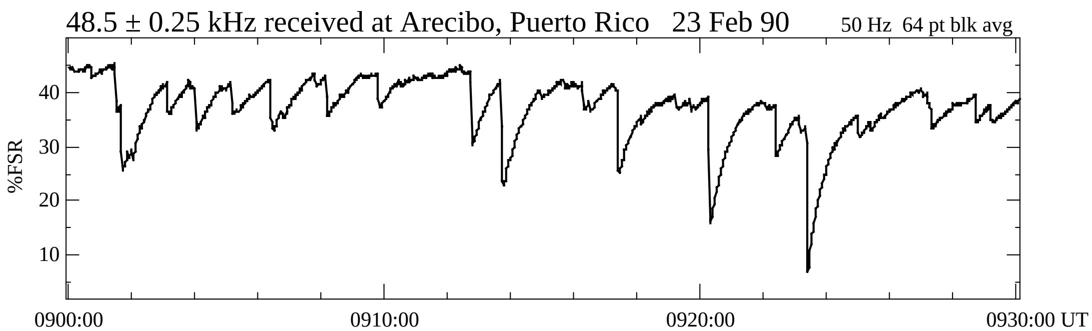

Fig. 1.3. Fluctuations in the amplitude of the subionospheric signal from a 48.5 kHz Air Force transmitter in Nebraska to Arecibo, Puerto Rico. The vertical scale is linear and measured in percent of Full Scale Range, the maximum signal strength that can be recorded by the data acquisition equipment.

received at sites in both Southern and Northern Hemispheres [*Carpenter et al.*, 1984; *Inan et al.*, 1990].

These signal perturbations, sometimes called "Trimpi" events, were attributed by *Helliwell et al.* [1973] to secondary ionization in the lower ionosphere caused by the impact of energetic radiation belt electrons which were scattered and precipitated by whistlers, a phenomenon now termed *Lightning-induced Electron Precipitation* (LEP). This hypothesis was based on an earlier experiment by *Rosenberg et al.* [1971] linking X-ray bursts to whistler-triggered emissions, and has been supported by many later ground-based studies [e.g. *Lohrey and Kaiser*, 1979; *Inan and Carpenter*, 1987] and by *in situ* observations of precipitating electrons in association with whistlers [*Rycroft*, 1973; *Voss et al.*, 1984] and with lightning [*Goldberg et al.*, 1987]. Figure 1.4 shows the sequence of events in which LEP is thought to create lower ionospheric disturbances, which in turn cause the observed perturbations of subionospheric signals.

The role played by whistler ducts in electron precipitation is less well understood. Although *Inan et al.* [1985*b*] assumed ducted wave propagation in a model of electron scattering by whistler-mode VLF transmitter signals, they found that predictions for scattering by both ducted and nonducted signals generally agreed with corresponding S81-1 satellite measurements of precipitating $\sim$18 keV electrons. A study of VLF transmitter-induced

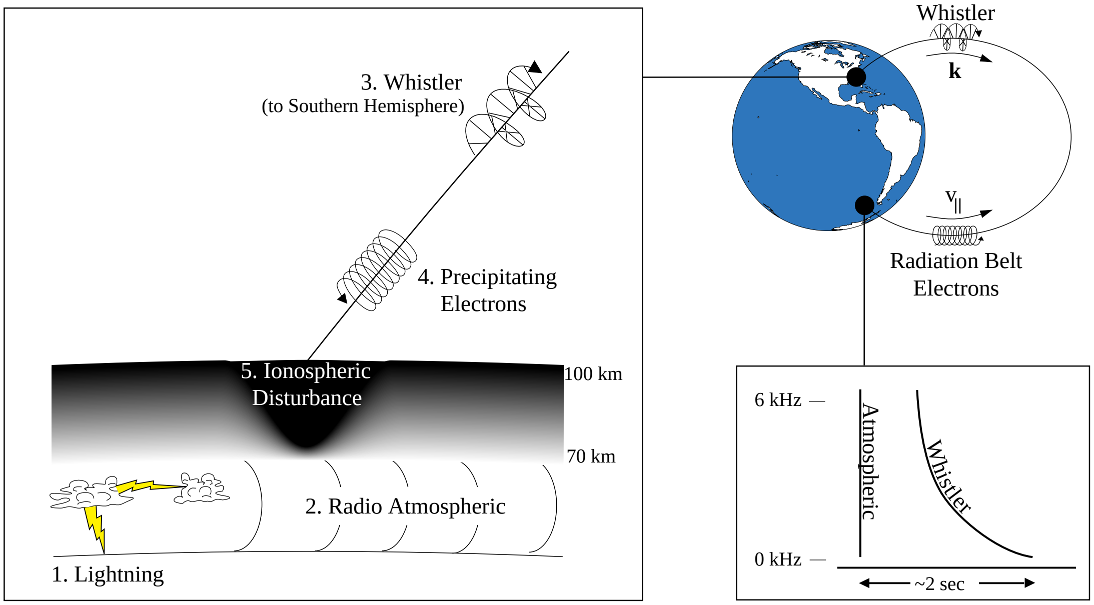

Fig. 1.4. Electron precipitation induced by ducted whistlers. A lightning discharge (1) launches a radio atmospheric, or sferic (2), which propagates in the Earth-ionosphere waveguide and is often strong enough to be detectable all over the planet. A duct can trap a portion of the sferic energy and cause it to propagate along a field line to the opposite hemisphere as a whistler (3). During its journey the circularly-polarized whistler can interact with gyrating energetic radiation belt electrons, scattering them in pitch angle so that some escape from their geomagnetic trap (4). Upon striking the ionosphere, the precipitating electrons cause significant secondary ionization (5). Meanwhile, the whistler emerges from its duct and can be observed, along with the subionospherically propagating "causative" sferic, with broadband VLF radio equipment in the opposite hemisphere.

precipitation by *Vampola* [1987] established that the distribution of 235 keV electron pitch angles observed on the S3-3 satellite was consistent with scattering either by field-aligned ducted waves above the ionosphere or by nonducted interactions very low on the field line. *Inan et al.* [1989] noted that the spatial extent of lightning-associated $>$45 keV precipitation bursts detected by the S81-1 satellite, as reported by *Voss et al.* [1984], is difficult to reconcile with scattering confined to a whistler duct.

Despite these concerns, ducted whistler waves are often assumed to be the primary scattering agent in lightning-induced precipitation of $\gtrsim$50 keV electrons. This is due in part to the efficiency with which such electrons are thought to be scattered by ducted whistlers [*Inan et al.*, 1989], but also in part to the reliable observation of ducted whistlers in association with the characteristic signal perturbations just mentioned; for example, after over three hundred comparisons of signal perturbations and broadband whistler data recorded on over twenty different days at Palmer Station, Antarctica, the author has yet to find a characteristic perturbation not accompanied by a ducted whistler. Additional evidence consistent with a cause-effect relationship between ducted whistlers and electron precipitation was presented by *Carpenter and LaBelle* [1982] and *Inan and Carpenter* [1986] in case studies of time and magnitude correlations between whistlers and signal perturbations.

This dissertation documents a new investigation of the association between ducted whistlers and electron precipitation on a global scale. The investigation begins with the discovery that whistler-associated ionospheric disturbances can occur almost simultaneously (within 1 s) in geomagnetically conjugate regions, and continues with an analysis of such disturbances using high-time-resolution conjugate recordings of subionospheric signal perturbations and comparisons with the multipath structure, arrival azimuths, and predicted electron scattering effects of associated whistlers. These analyses provide us with more comprehensive evidence of the scattering and bounce behavior of whistler-associated precipitation bursts than was heretofore available. The results of this study not only support a strong link between individual whistler ducts and conjugate ionospheric disturbances, but imply that every ducted whistler component precipitates electron bursts and that such precipitation significantly influences the equilibrium of the radiation belts.

1.2 SUBIONOSPHERIC VLF, LF, AND MF RADIO SIGNATURES OF LIGHTNING-INDUCED ELECTRON PRECIPITATION (LEP)

Precipitating bursts of energetic radiation belt electrons are thought to be induced when a magnetospheric wave propagating in the whistler mode undergoes cyclotron resonance with electrons traveling in the opposite direction, scattering them in pitch angle [*Dungey*, 1963; *Cornwall*, 1964]. ELF and VLF whistler mode signals can resonate with quasi-relativistic electrons of energies ranging from tens of keV to over 1 MeV. If scattered into the bounce loss cone, these electrons penetrate the atmosphere to altitudes between 40 and 90 km [*Rees*, 1963]. When scattered by a southbound whistler, a precipitation burst would first encounter the Northern Hemisphere ("direct precipitation"). Upon reaching the atmosphere, up to 90% of the burst electrons could backscatter due to their grazing angles of incidence [*Berger et al.*, 1974] and would return along the field line to encounter the Southern Hemisphere. If there is an asymmetry between northern and southern mirror heights, such as that caused by the South Atlantic Magnetic Anomaly, a portion of the direct burst would mirror and also return to precipitate in the south without having first reached the atmosphere in the north. Precipitation bursts made up of backscattered and mirrored electrons are termed "reflected precipitation." Repeated backscattering and mirroring in both hemispheres have been shown to extend the lifetimes of precipitation bursts to several bounce periods [*Inan et al.*, 1985*b*; *Voss et al.*, 1984].

The phenomenon of LEP described above is frequently illustrated as in Figure 1.4, shown earlier; there are, however, at least two important ways in which circumstances may vary from the diagram. First, the lightning discharge need not be near the duct entrance, and indeed could be many hundreds or even thousands of kilometers away [*Carpenter and Orville*, 1989; *Yip et al.*, 1991]; second, at the longitudes of the South Atlantic Magnetic Anomaly (approximately 95° W to 20° E) which are involved here, the first significant impact of precipitation on the atmosphere may occur in the south even for whistlers originating in the north [*Inan et al.*, 1988*c*]. Chapters 4 and 5 discuss the latter point in detail.

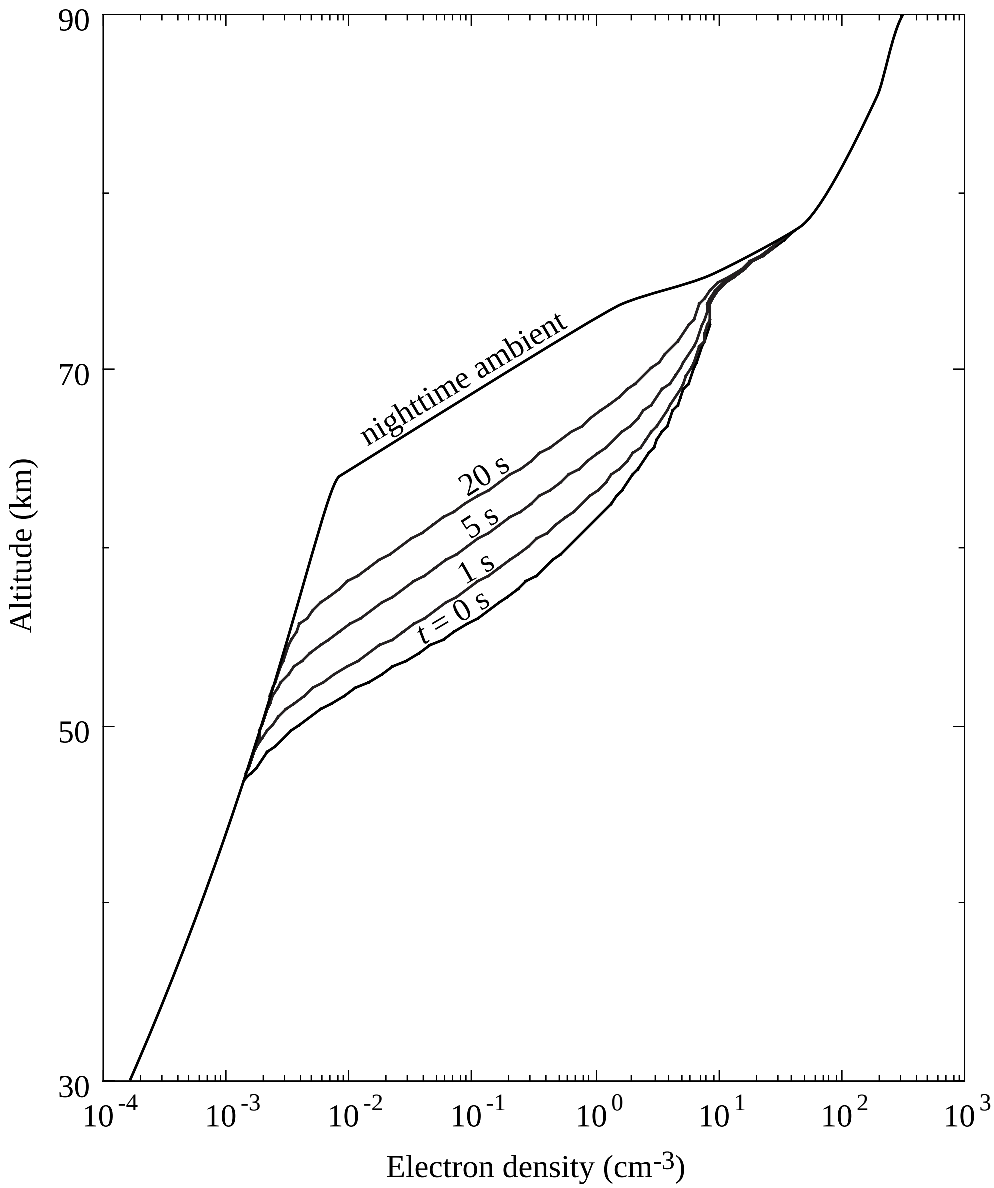

Fig. 1.5. Vertical profile of an ionospheric disturbance caused by lightning-induced electron precipitation. The $t = 0$ profile shows ionization resulting from a simulated lightning-induced electron precipitation burst, while the subsequent profiles show the recovery of the disturbance to ambient levels due to recombination and attachment processes. (After *Inan et al.*, 1988*a*.)

Upon their impact with the lower ionosphere, electron precipitation bursts produce X-rays, heating and secondary ionization, with the latter resulting in significant disturbances of ionospheric electron density. The three-dimensional structure of electron density within these ionospheric disturbances is not known, but they are thought to be less than 100 km in horizontal extent [*Carpenter and LaBelle*, 1982; *Inan et al.*, 1990] and to lie between 40 and 90 km in altitude as shown in Figure 1.5 [*Inan et al.*, 1988*a*]. Excess ionospheric electron densities at these altitudes are predicted to return to ambient levels over 10–100 s as a result of recombination and attachment processes [*Gledhill*, 1986; *Glukhov et al.*, 1992].

The transient disturbances of the lower ionosphere induced by LEP can in turn perturb VLF, LF, and MF signals propagating in the Earth-ionosphere waveguide (Figure 1.6). Such disturbances near the great circle transmitter-to-receiver path of a signal can change the relative amplitudes and phases of a signal's constituent waveguide modes, resulting in a sudden amplitude increase or decrease and/or a sudden phase advance or delay in the signal observed at the receiver [*Poulsen et al.*, 1993].

The lightning discharge with which these signal perturbations are indirectly associated (see Figure 1.4) generates a radio atmospheric which is often strong enough to be detected as an amplitude impulse on narrowband as well as broadband VLF recordings [*Inan et al.*, 1988*b*]. When this narrowband "causative sferic" can be identified, the delay between it and the onset of the associated signal perturbation is called the "onset delay." *Lohrey and Kaiser* [1979] linked onset delays to magnetospheric parameters, including *L*-shell and cold plasma electron density, which control the time required for significant whistler-electron interactions to begin. Later studies by *Chang and Inan* [1983], *Carpenter et al.* [1984] and *Inan et al.* [1985*a*] have supported this interpretation. Commonly observed onset delays range from 0.3 to 1.6 s.

The change in the signal's amplitude or phase typically reaches its maximum over a period of 0.5 to 1.5 s called the "onset duration." *Chang and Inan* [1983], *Carpenter et al.* [1984] and *Inan et al.* [1985*a*] have interpreted onset duration as an indication of the

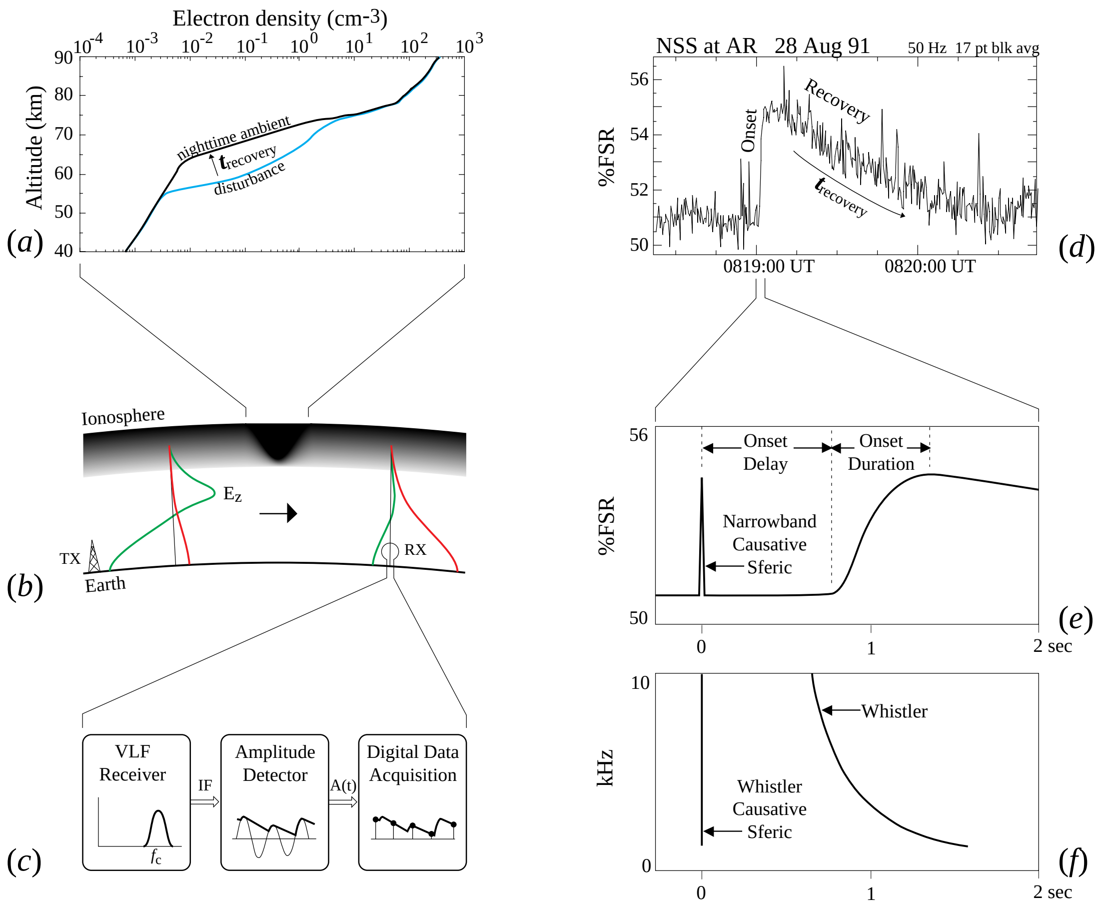

Fig. 1.6. Remote sensing of transient ionospheric disturbances using subionospheric VLF radio. (*a*) Electron precipitation disturbs the ambient nighttime density profile of the ionosphere. The profile recovers to the ambient over about one minute. (*b*) The disturbance changes the relative amplitudes and phases of the Earth-ionosphere waveguide modes which constitute a subionospheric VLF signal propagating nearby. The vertical electric field (E_z) components of two possible modes are illustrated. (*c*) The subionospheric signal is acquired with a narrowband VLF receiver, whose intermediate frequency (IF) output is amplitude detected. The resulting signal amplitude $A(t)$ is sampled and recorded. (*d*) The signal amplitude perturbation caused by the ionospheric disturbance appears as an upgoing or downgoing onset followed by a roughly exponential recovery to the ambient signal level. When calibration is unavailable, signal amplitudes are given as a percent of the recording limit, or "full scale range" (FSR), of the acquisition system. NSS is the transmitter, AR is the receiver (see the abbreviations in Tables 3.1 and 3.2). (*e*) The causative sferic (see Figure 1.4) is often strong enough to be detectable in the narrowband record when the perturbation onset is examined closely, and provides a time reference for comparison with the associated whistler (*f*). The sferics in (*e*) and (*f*) are shown arriving at their respective receivers simultaneously, but the difference in propagation delay can be 40 ms or more when the narrowband and broadband receivers are in opposite hemispheres.

length of time during which secondary ionization is produced in the ionosphere by the burst of precipitating electrons.

Signal perturbation onsets are followed by a roughly exponential recovery to ambient signal conditions, typically within 100 s. Signal recovery signatures may allow an assessment of ionospheric chemistry at the altitudes to which precipitation bursts penetrate [*Dingle*, 1977]. *Inan et al.* [1988*a*] and *Glukhov et al.* [1992] have found agreement between observed recovery behavior and predictions from models of ionizing burst penetration altitudes and corresponding ionospheric recombination and attachment rates.

Recent work has suggested that signal perturbation data can be used to “image” the locations of ionospheric disturbances. Experimental evidence implies that signal perturbations are caused by disturbances within 100 km of the signal path [*Inan et al.*, 1990] and three-dimensional modal modeling by *Poulsen et al.* [1990] suggests that an ionospheric disturbance would not detectably perturb subionospheric VLF signals whose paths lie more than 250 km away from the disturbance center. An example of the model results is shown in Figure 1.7. As indicated in the figure, the effect of atmospheric noise on the signal receivers often means that signal amplitude perturbations less than 0.05 dB cannot be distinguished, so in practice only disturbances within $\sim$200 km of a signal path would detectably perturb it. These results suggest that the location of an ionospheric disturbance’s center can be estimated to lie within 200 km of the perturbed signal paths.

Dowden and Adams [1989, 1990] have presented an alternate hypothesis to predict the effect of ionospheric disturbances on subionospheric signals, based on the modeling of disturbances as perfectly reflecting “stalactites” which deform the top of the Earth-ionosphere VLF waveguide by 10–15 km. The stalactite model, in contrast to the density-gradient/waveguide mode model used by *Poulsen et al.* [1990], suggests that disturbances over 1000 km from the great circle path of a subionospheric signal may cause detectable signal perturbations [*Dowden and Adams*, 1990]. This conclusion is, however, inconsistent with patterns of

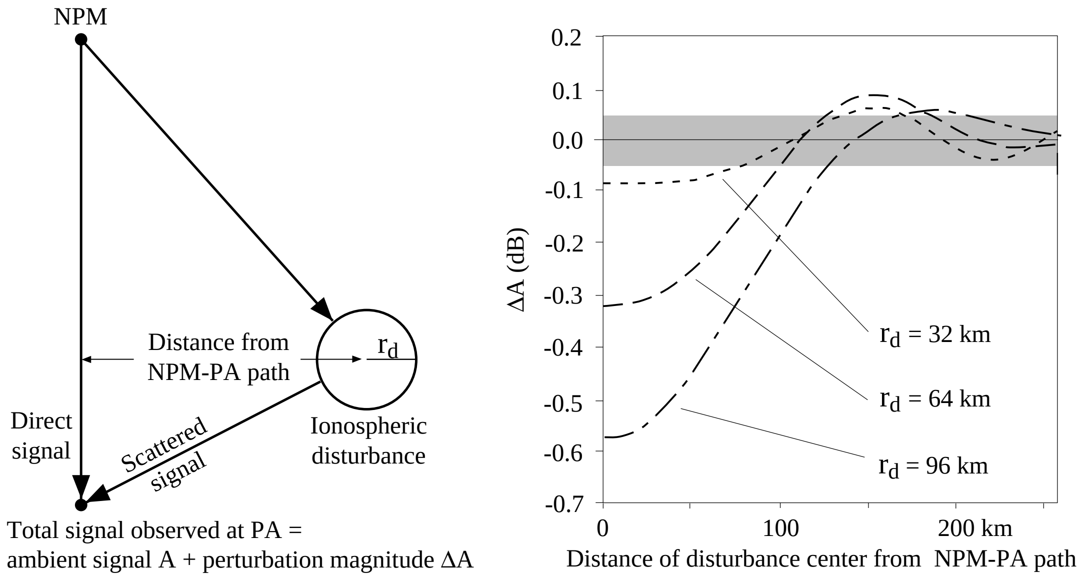

Fig. 1.7. Variation of the signal perturbation magnitude ΔA with the distance separating an idealized ionospheric disturbance from a subionospheric signal path between a VLF transmitter in Hawaii (NPM) and a receiver at Palmer Station, Antarctica (PA). Values for path-disturbance separation lay along a line perpendicular to the NPM–PA path at a distance of 3000 km from Palmer. The results are based on a theoretical model of VLF signal propagation in the Earth-ionosphere waveguide by *Poulsen et al.* [1990]. Curves are shown for three different values of effective disturbance radius r_d. Atmospheric noise tends to obscure signal perturbations smaller than about 0.05 dB, as indicated by shading in the graph. The model suggests that disturbances more than 200 km away from the signal path are unlikely to detectably perturb it.

perturbation activity observed on networks of signal paths [*Inan et al.*, 1990]. In addition, the creation of a reflecting stalactite disturbance requires the impact of ten times more precipitating energy flux than that of a density-gradient disturbance for the same observed subionospheric signal perturbation [*Bell et al.*, 1990]. Because of these concerns, and because the density gradients used by *Poulsen et al.* [1990] would seem to be a more accurate representation of ionospheric disturbances, the assumption that perturbations of a signal indicate disturbances within 200 km of the signal's great circle path appears to be justified for the purposes of this research.

1.3 CONTRIBUTIONS

The goal of this research has been to enhance our understanding of the coupling between lightning, the ionosphere and the magnetosphere. The specific scientific contributions resulting from these efforts are presented in Chapters 4–6 as follows:

Chapter 4 The discovery of simultaneous, geomagnetically conjugate ionospheric disturbances associated with individual ducted whistlers.

Chapter 5 A detailed assessment of the association between conjugate ionospheric disturbances and electron precipitation inferred to be caused by ducted whistler components, including:

- One-to-one comparisons of the exit location of ducted whistlers with the configuration of perturbed conjugate subionospheric signal paths, finding a link between duct location and the inferred location of precipitation in both hemispheres;

- High time resolution comparison of the onsets of conjugate signal perturbations with predictions for the timing of ducted-whistler-induced precipitation bursts, finding agreement with theory; and

- Explanation of anomalous signal perturbation onset behavior in terms of multiple ionospheric disturbances associated with the several components of multipath whistlers.

Chapter 6 A quantitative estimate of the effect of ducted-whistler-induced depletion on the radiation belts. Belt losses due to ducted whistlers appear to be comparable to other loss processes suggested in the literature, indicating that lightning, via the phenomenon of ducted whistlers, significantly influences radiation belt equilibrium.

1.4 PRACTICAL CONCERNS RELATED TO THIS RESEARCH

Although focused on basic geophysical questions, this research is related to several general concerns critical to our profitable understanding and use of near-Earth space. Some of these concerns are as follows:

- *Space equipment has to operate in a plasma environment.*

Manned and unmanned spacecraft operate while immersed in a space plasma. Solar panels in particular are sensitive to bombardment by radiation belt particles, losing years of anticipated life in as many days during intense geomagnetic storms. Astronauts caught in such storms risk severe radiation poisoning or death. Our understanding of space plasma processes influences the way we design spacecraft and the orbital trajectories we select for them.

- *Satellite observations are affected by the plasma environment.*

The plasma surrounding a spacecraft also affects its data and status sensors; for example, natural electromagnetic waves may cause responses on board the craft which could be misinterpreted as internal noise or as evidence of component failure. Responsible interpretation of satellite observations requires knowledge of the plasma environment.

- *Radio navigation and communication are affected by ionospheric activity.*

Changes in the ionosphere can influence long-distance transmissions which propagate between the Earth and ionosphere, including AM, FM and shortwave radio broadcasts, Omega and LORAN navigation signals, and military ELF/VLF communications. Transionospheric signals such as those from the Global Positioning System (GPS) satellites are also affected by ionospheric disturbances; GPS is especially susceptible to errors when only one of the two GPS ranging frequencies is being used [*Klobuchar and Doherty*, 1990]. Better understanding of the causes and effects of ionospheric disturbances could improve the quality of subionospheric radio communications and the accuracy of navigational location fixes using Omega, LORAN and GPS.

2

Geophysical Background

The research documented in this dissertation is not easily categorized into any one branch of science or engineering. Lightning, space plasmas, geomagnetic trapping of relativistic electrons and the structure of the geomagnetic field are all pieces of this geophysical puzzle. The radio waves studied propagate in imperfect waveguides and in anisotropic and inhomogeneous media. Data acquisition depends on analog and digital instrumentation whose behavior must be understood. Time-domain and spectral analyses of the data demand familiarity with signal processing algorithms and their limitations.

While a full treatment of these disciplines is beyond the scope of this document, this chapter provides a background in geophysics and radio science adequate to follow the dissertation's main ideas. The reader is assumed to understand basic radio and data acquisition electronics and signal processing techniques.

2.1 LIGHTNING AND RADIO ATMOSPHERICS

Lightning is the trigger which sets off the chain of events investigated in this research. Worldwide, perhaps 100 lightning flashes per second [*Orville and Spencer*, 1979], each releasing 10^9–10^{10} J of energy [*Uman*, 1987, p. 323], dissipate up to 10^{12} W into thunder, heated air, and radio waves [*Uman*, 1987, p. 31]. It is the latter effect we are concerned with here.

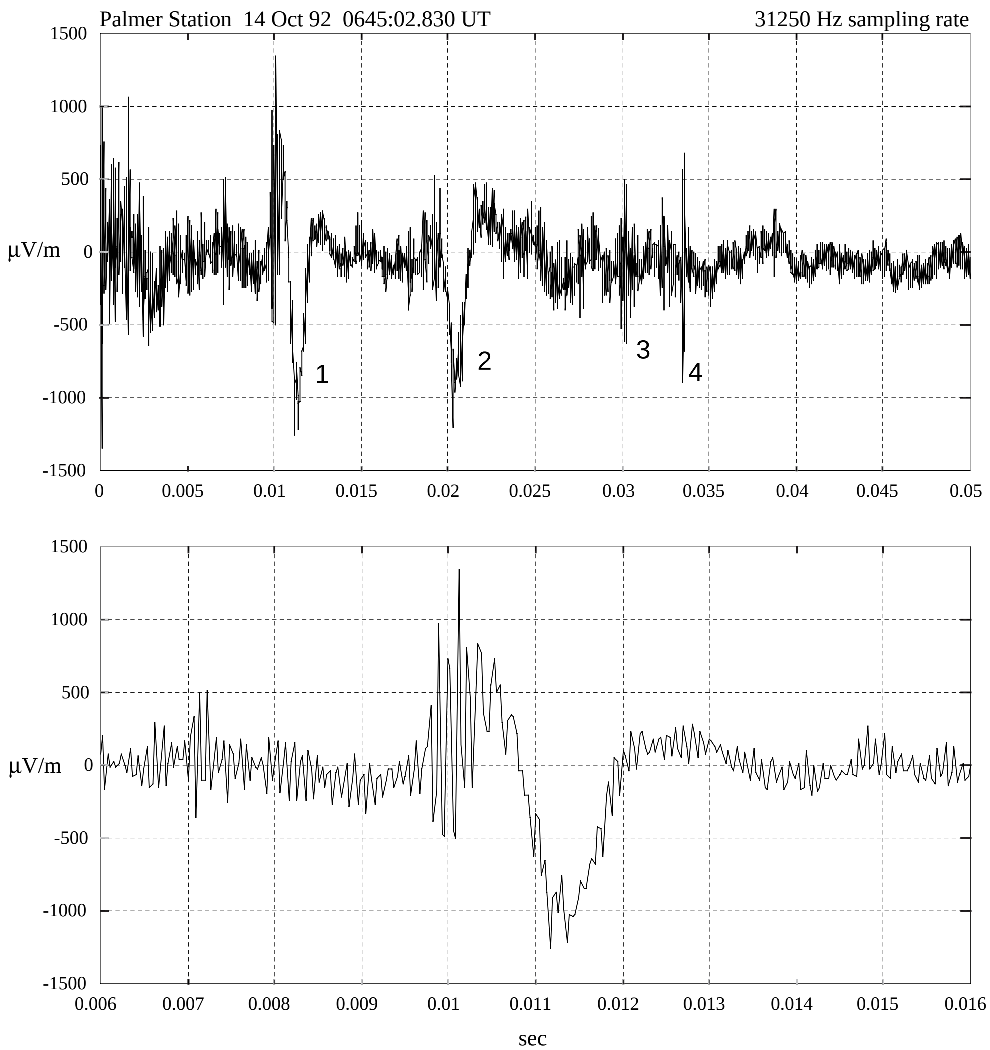

Fig. 2.1. Atmospherics observed at Palmer Station, Antarctica. The upper panel shows four atmospherics, each with different characteristics, during a 50 ms period. The lower panel shows the first atmospheric in detail.

The intense discharge currents involved in lightning, on the order of 30 kA, radiate powerful impulsive radio signals known as *radio atmospherics* or often simply *sferics*.* These signals extend from near DC up into the megahertz range, peaking in the VLF near 10 kHz [*Davies*, 1966, p. 413]. As we shall see, the VLF radio energy in sferics not only

* Two spellings of the shorthand term for radio atmospheric – “spheric” and “sferic” – are in common use. This dissertation uses “sferic” to avoid the geometric connotations of “spheric.”

finds its way around the world (Figure 2.1) but can penetrate tens of thousands of kilometers into space.

Inan et al. [1991] have recently suggested that the electromagnetic impulse generated by a lightning discharge can substantially heat the lower ionosphere above the flash, producing ionization enhancements [*Rodriguez et al.*, 1992] and optical emissions [*Taranenko et al.*, 1992].

The reader is referred to *Uman*'s [1987] monograph for a comprehensive treatment of the causes and effects of lightning.

2.2 THE IONOSPHERE

The ionosphere is an atmospheric layer, beginning at about 60 km above the Earth's surface, where "ions and electrons are present in quantities sufficient to affect the propagation of radio waves" [*Wave Propagation Standards Committee*, 1977]. The ionosphere is commonly divided into *D*, *E*, and *F regions* depending on altitude and free electron density as shown in Figure 2.2. The presence of free charge in the ionosphere is primarily due to cosmic rays and ionizing radiation from the sun.

Because the Earth's surface and the ionosphere both behave as conducting surfaces at very low frequencies and are separated by only a few VLF wavelengths, they constitute an imperfect parallel-plate waveguide for VLF signals. Signals thus guided are said to propagate *subionospherically* or in the *Earth-ionosphere waveguide*. Subionospheric VLF propagation can be very efficient: during the night, when fewer free electrons are available to cause absorption in the D-region, attenuation of signals between 15 and 20 kHz can be as low as 1 dB per 1000 km [*Davies*, 1966, p. 426]. As a result, atmospherics and man-made VLF signals can often be detected on the opposite side of the globe from their source.

Subionospheric VLF signals are usually modeled as a summation of several waveguide modes. When one takes into account the complex, anisotropic and location-variant reflection

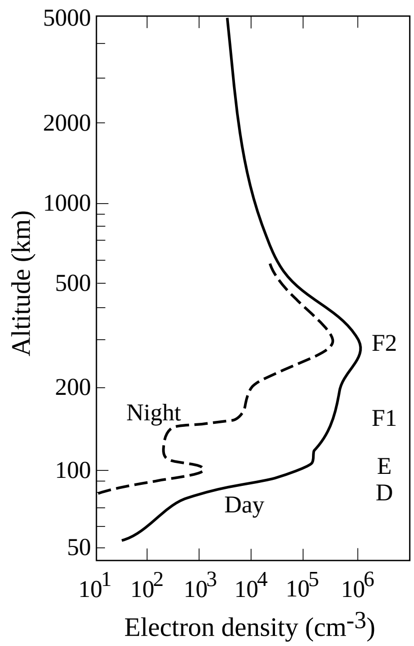

Fig. 2.2. Ionospheric nomenclature. Ionospheric layers are defined in terms of altitude and free electron number density. The lack of solar ionizing radiation at night leads to lower electron densities. Actual electron densities may vary an order of magnitude or more from those shown depending on season and solar conditions. See Figure 1.5 for an expanded profile of the nighttime D-region. (After *Davies* [1966].)

coefficients of the Earth and ionosphere, such modeling becomes difficult. The reader is referred to the Ph.D. thesis of *Poulsen* [1991] for a recent treatment of subionospheric VLF propagation. An excellent applied reference on radio waves in the ionosphere is *Davies* [1966], while *Budden* [1985] presents a more general and theoretical analysis of radio propagation. An extensive discussion of ionospheric physics is given by *Ratcliffe* [1972].

2.3 THE INNER MAGNETOSPHERE

The magnetosphere is that part of the Earth's atmosphere where the Earth's magnetic field, "as modified by the solar wind, controls the motions of charged particles" [*Wave Propagation Standards Committee*, 1977]. The magnetosphere is conceptually divided into the outer magnetosphere, where the solar wind profoundly distorts the geomagnetic field, and the inner magnetosphere (Figure 2.3), where the geomagnetic field more closely resembles a dipole.

This section discusses the structure of the geomagnetic field in the inner magnetosphere and its relation to the plasmasphere, whistler waves, the radiation belts and whistler-electron interactions. A discussion of outer magnetospheric phenomena, as well as a more complete treatment of the inner magnetosphere, can be found in *Ratcliffe* [1972].

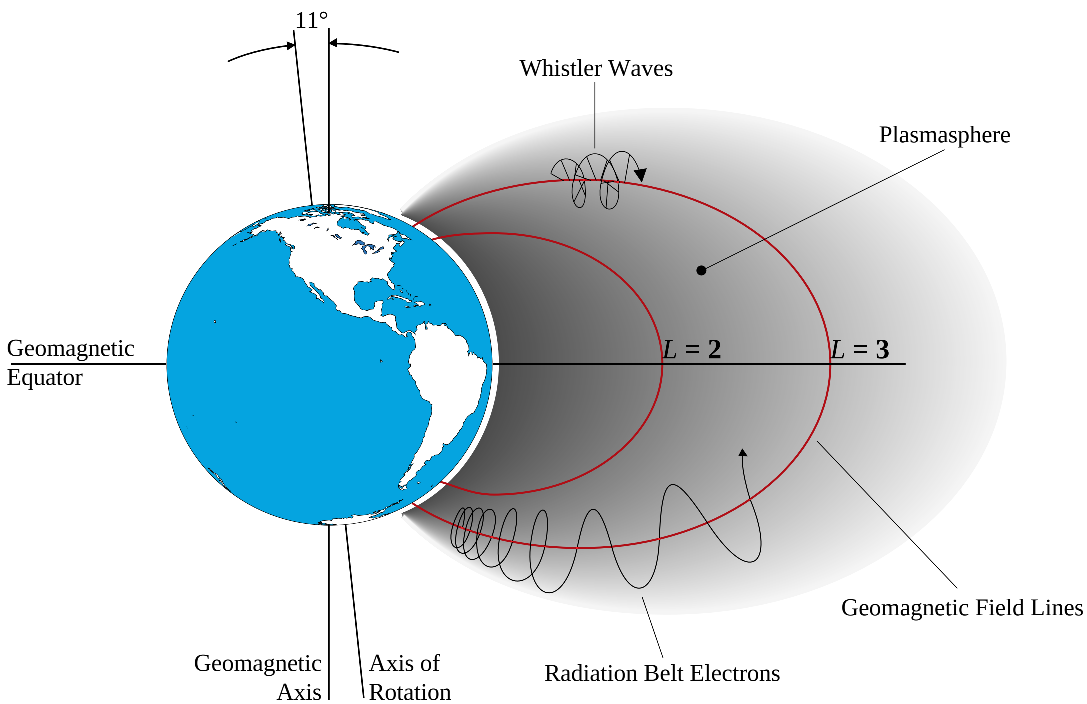

Fig. 2.3. A cross-section of the inner magnetosphere.

2.3.1 The Geomagnetic Field

Because of its dominant role in the behavior of magnetospheric plasmas and waves, the Earth's magnetic field is the frame of reference for all studies involving the magnetosphere. The total geomagnetic field is a combination of an "internal" field generated inside the Earth and an "external" field imposed by extraterrestrial sources. The internal field is often attributed to the movement of charged material in the Earth's molten core [*Merrill and*

McElhinney, 1983], while the external field depends on the solar wind as well as on the motion of vast numbers of charged particles in the magnetosphere and ionosphere. Attempts to model the geomagnetic field began four centuries ago with William Gilbert's treatise *De Magnete* [*Gilbert*, 1600] and continue today, although even now accuracy is limited by gradual ("secular") changes in the internal field and by the complexity of the external field [*Stern and Tsyganenko*, 1992]. The two models of the geomagnetic field applied in this research were the numerical model of *Tsyganenko* [1989] and the analytical centered dipole approximation.

The *Tsyganenko* [1989] model provided the locations, in opposite hemispheres, where a given field line intersects the Earth's ionosphere at 100 km altitude. Accurate determination of these location pairs, referred to in this dissertation as *geomagnetic conjugates*, was necessary to interpret data from ground stations in a geomagnetic context.

The *centered dipole* approximation was used to model magnetospheric propagation of whistler waves along the inner field lines depicted in Figure 2.3. This model represents the geomagnetic field as an infinitesimal dipole located at the center of the Earth and tilted 11° from the axis of rotation. Using this model, the field* at a given point is written [*Lyons and Williams*, 1984]:

$$B = 0.312 \times 10^{-4} \left(\frac{R_\oplus}{r}\right)^3 (1 + 3\sin^2\lambda)^{\frac{1}{2}} \quad \text{(T)} \tag{2.1}$$

where the variables are

- $R_\oplus$ mean radius of the Earth (6370 km)
- r distance from the center of the Earth
- λ magnetic latitude (0° at the geomagnetic equator).

A common parameter used to identify field lines on a given magnetic meridian is *McIlwain's* [1961] *L*, which is the distance from the Earth's center, measured in Earth radii, at

* Three metric units are in common use for specification of magnetic flux density. This dissertation uses the Tesla (T), which is equivalent to 1 N A^{-1} m^{-1}. Other popular units are the Gauss (1 Gauss = 10^{-4} T) and the Gamma (1 γ = 10^{-9} T).

which a centered dipole field line would cross the geomagnetic equator (see also *Schulz and Lanzerotti* [1974]). Because a fixed L represents the locus of points on the surface of the corresponding dipole toroid or "shell," a given value of L is often referred to as an "L-shell." When magnetospheric phenomena are monitored on the ground, knowledge of the ground station's L-shell is critical because it identifies the region of space being observed. From the dipole relation

$$\frac{r}{\cos^2 \lambda} = \frac{R_\oplus}{\cos^2 \lambda_0} \tag{2.2}$$

we can derive the relationship between L and surface magnetic latitude λ_0 (since by definition $L = r/R_\oplus$ at $\lambda = 0$, the magnetic equator):

$$L = \frac{1}{\cos^2 \lambda_0}. \tag{2.3}$$

The equatorial magnetic field B_{eq} can be determined for a given L as

$$B_{eq} = 0.312 \times 10^{-4} L^{-3} \quad \text{(T)}. \tag{2.4}$$

For convenience space scientists often use the terms *low-latitude, mid-latitude* and *high-latitude* to roughly indicate $L < 2$, $2 < L < 5$ and $L > 5$ respectively.

The applicability of the centered dipole model to this research is tempered by the presence of the South Atlantic Magnetic Anomaly, a region of the Earth's surface where the geomagnetic field is unusually low (Figure 2.4). These relatively low field strengths increase the likelihood that radiation belt electrons will strike the atmosphere over the Anomaly (see Sections 2.3.4 and 2.3.5).

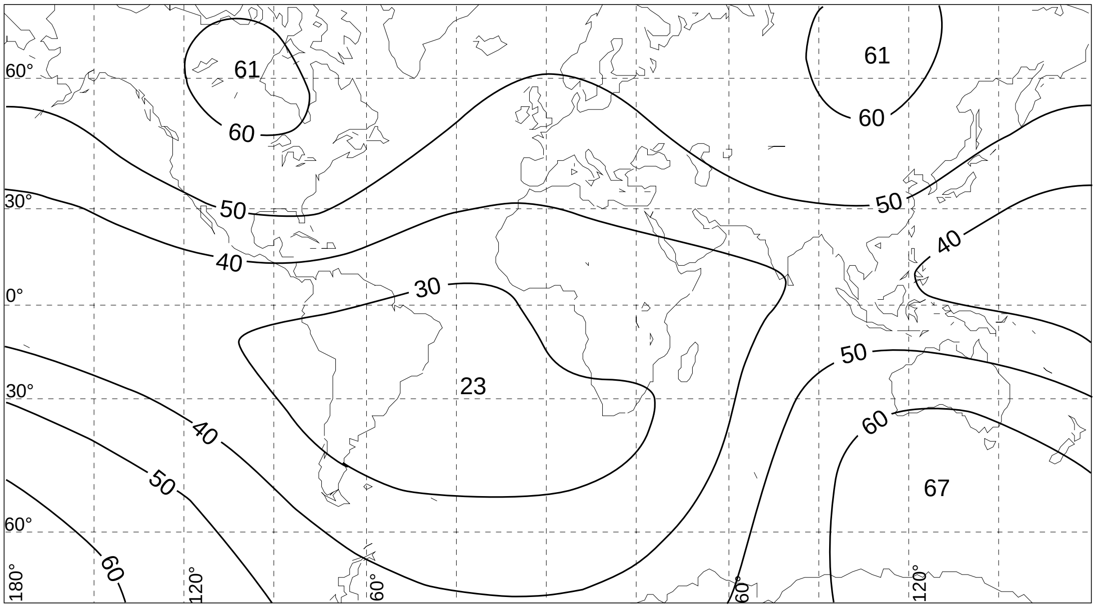

Fig. 2.4. The South Atlantic Magnetic Anomaly in 1980. The contours represent lines of constant total magnetic field intensity, in μT, on the surface of the Earth. (After *Parkinson* [1982].)

2.3.2 The Plasmasphere

The magnetosphere is populated by ions and electrons with energies on the order of 1 eV. These low-energy particles collectively form a charge-neutral material referred to as the *cold plasma*, maintained by upward diffusion of the particles from the top of the ionosphere. Cold plasma density is usually represented by the electron number density N_e and given in terms of cm^{-3}. Plasmaspheric values of N_e are commonly quoted for the geomagnetic equator (N_{eq}).

An example profile of equatorial electron density as a function of *L* is shown in Figure 2.5. The most significant feature is the *plasmapause*, an abrupt order-of-magnitude drop located in this case at L = 3.3. The location of the plasmapause ranges from L = 2 during geomagnetic disturbances to as far as L = 7 after several days of geomagnetic quiet. The region of relatively high electron densities inside the plasmapause is called the *plasmasphere*.

Electrons in a plasma are susceptible to collective oscillatory motion, alternately storing

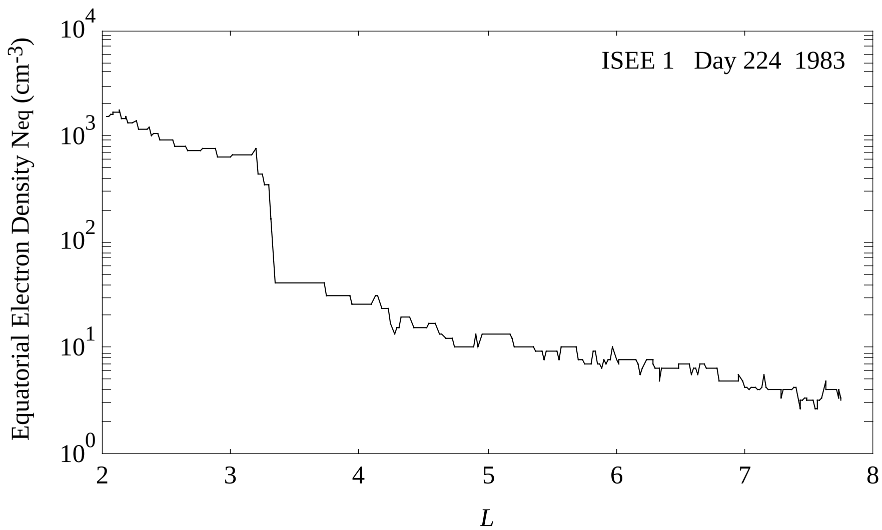

Fig. 2.5. Equatorial cold plasma electron density profile on August 12, 1983, showing the plasmapause. Although the plasmapause can move or disappear depending on solar activity, this is a typical quiet-time profile. (From satellite data presented by *Carpenter and Anderson* [1992].)

energy kinetically and in electric field potential. These oscillations are represented by the *plasma frequency* (ω_N), which is given by

$$\omega_N = \sqrt{\frac{N_e e^2}{\epsilon_0 m_e}}, \tag{2.5}$$

where ϵ_0 is the permittivity of free space, e is electron charge and m_e is electron mass.

Charged particles in a magnetic field gyrate at a *gyrofrequency* which depends on the local magnetic field strength. For electrons, the gyrofrequency ω_H can be found by equating the Lorentz force evB with the centripetal force $m_e v^2/r$, giving

$$\omega_H = \frac{eB}{m_e} \tag{2.6}$$

where B is the local magnetic field. Note that a non-relativistic particle's gyrofrequency is independent of its velocity. In this dissertation, the term "gyrofrequency" refers exclusively to electron gyrofrequency.

2.3.3 Whistlers

Magnetized plasmas support radio waves with complex propagation behavior. Wave characteristics in a magnetized plasma are described by refractive indices which are involved functions of plasma density, magnetic field, wave frequency and wavefront propagation (or *wave-normal*) vector. The reader is referred to *Ratcliffe* [1972] and *Budden* [1985] for comprehensive treatments of wave propagation in magnetized plasmas.

For wave frequencies below the local electron gyrofrequency, magnetized plasmas become very dispersive and allow only elliptically polarized waves to propagate. Since minimum (i.e., equatorial) gyrofrequencies between $L = 2$ and $L = 4$ range from 109 kHz to 14 kHz, it is below these frequencies – mostly in the VLF – that such interesting wave phenomena are found. Perhaps the best known of these phenomena is the *whistler*, the VLF radio signal of an atmospheric which has found its way into the magnetosphere and has become dispersed. Whistlers are classified as either *ducted* or *nonducted* depending on their propagation characteristics.

Ducted whistlers

The *ducted whistler* (Figure 2.6), introduced in Chapter 1, has been noted and studied by ground observers for decades. To be detected on the ground after propagation in the magnetosphere, however, these whistlers must somehow pass through the relatively high refractive indices of the lower ionosphere without suffering total internal reflection. That this occurs indicates that whistlers arrive at the ionosphere with wave-normal vectors within a “transmission cone” of only a few degrees [*Helliwell*, 1965]. To explain this phenomenon, a hypothetical magnetospheric guiding structure has been inferred called a *whistler duct* [*Helliwell*, 1965]; hence the term “ducted whistler.”

Whistler ducts are thought to be localized enhancements of cold plasma density aligned with the geomagnetic field, extending between the hemispheres and capable of guiding VLF waves with wave normal vectors nearly parallel to the field (Figure 1.2). Unfortunately, *in*

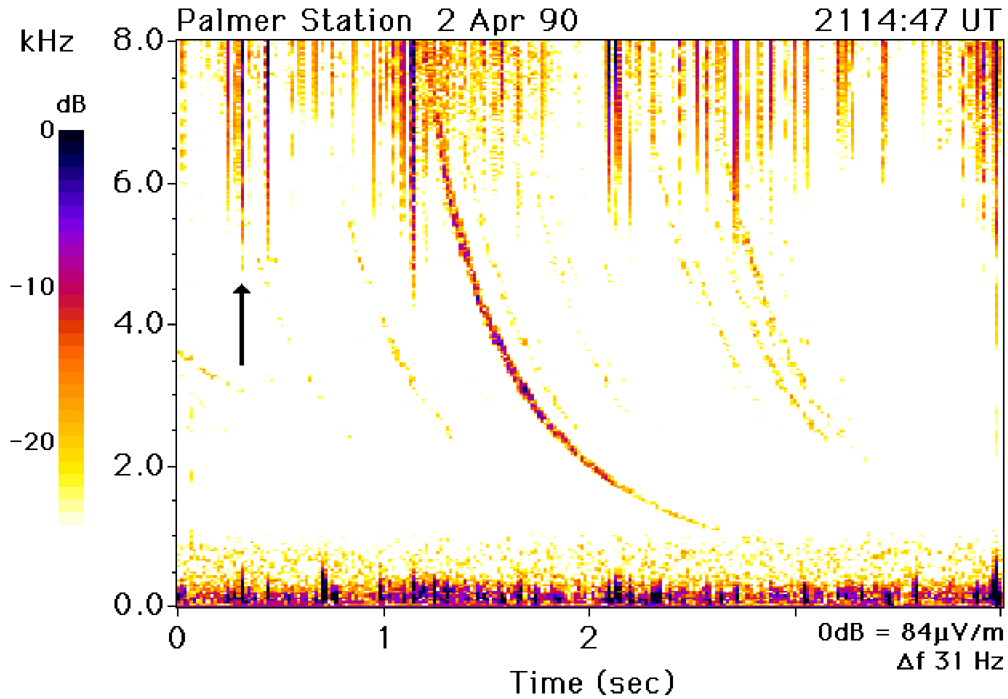

Fig. 2.6. A well-defined ducted whistler. The arrow marks the *causative sferic*, the subionospheric radio signature of the same lightning flash responsible for the whistler (Figure 1.4). The frequency dispersion of the whistler can be used to estimate the *L*-shell and the equatorial plasma density along its propagation path (Section 3.2.2). The display format is called a *dynamic spectrogram*. Several weaker whistlers can also be seen.

situ evidence of ducts is limited; ducts as currently hypothesized might be no more than 500 km in diameter at the magnetic equator, making their existence difficult to verify by satellite [*Angerami*, 1970]. The size and cross-sectional shape of whistler ducts remain unknown [*Strangeways*, 1991], although the characteristics of duct exit regions, inferred from ground measurements of signals emerging from ducts, may shed light on duct structure [*Ikeda et al.*, 1988].

Ducted whistlers sometimes “echo” between hemispheres; for example, a whistler originating in the Northern Hemisphere could be observed on the ground first in the south (a “one-hop” whistler), then in the north (two-hop), then in the south again (three-hop), and so forth. An example of a three-hop whistler can be seen in Figure 5.10.

The common observation of *multipath whistlers* (Figure 2.7) suggests that several ducts

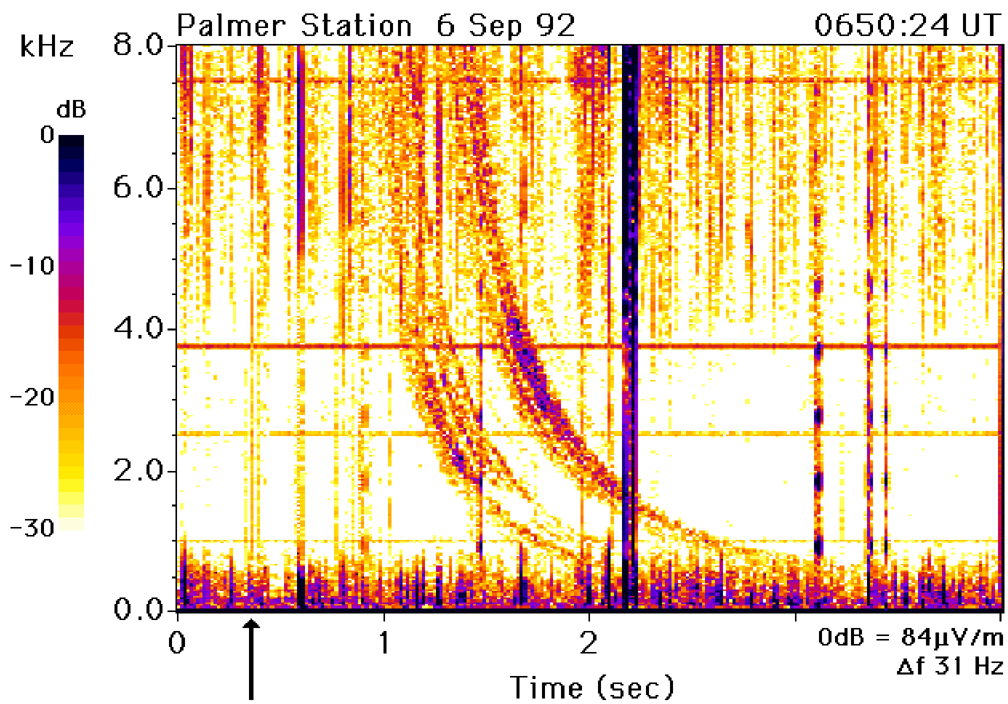

Fig. 2.7. A multipath ducted whistler. The arrow marks the causative sferic. A very strong burst of sferics obscures the whistler at $t \simeq 2.2$ s.

may be available for whistler propagation at any given time. Indeed, whistlers clearly exhibiting at least two propagation paths comprise over 95% of the several hundred whistlers the author has examined.

The reader is referred to *Helliwell*'s [1965] monograph for a thorough discussion of ducted whistlers and whistler-related wave phenomena.

Nonducted whistlers

Satellite observations have shown that whistlers which do not exhibit ducted dispersion characteristics are common inside the plasmasphere [*Edgar*, 1976]. These *nonducted* whistlers (Figure 2.8) appear to propagate along gradually bending paths determined by the geomagnetic field and by cold plasma density gradients in the plasmasphere. During propagation, the wave-normal vectors of nonducted whistlers reach angles of up to 90° from their wave group

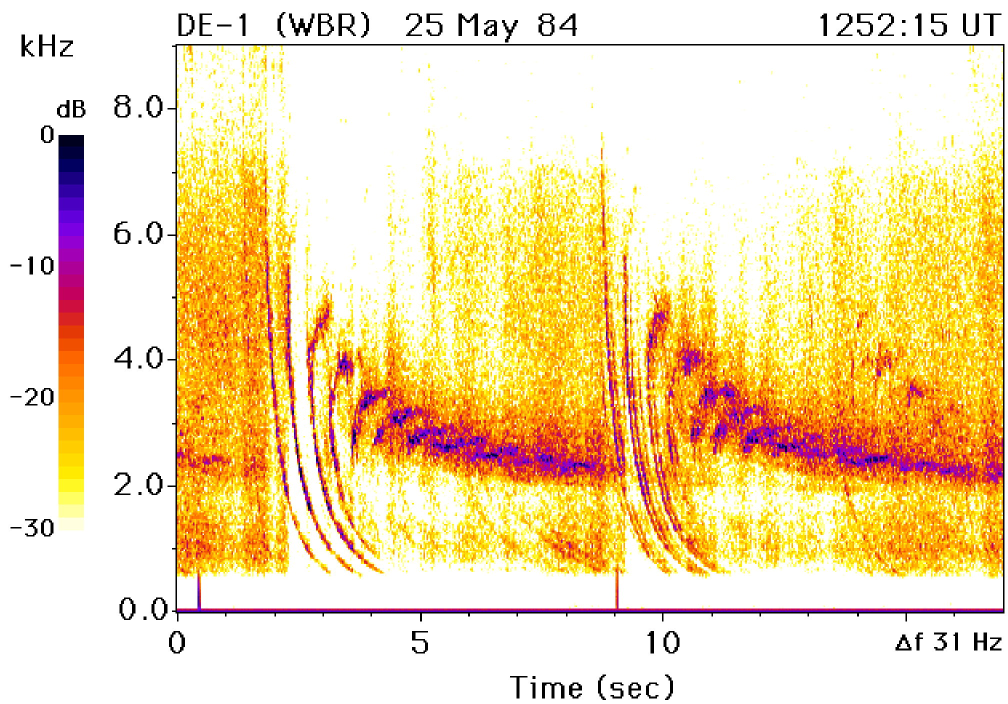

Fig. 2.8. Nonducted whistlers. Broadband data acquired with a 200 m electric field dipole antenna on the Dynamics Explorer 1 satellite [*Shawhan et al.*, 1981]. Each sequence of magnetospherically reflected whistlers is triggered by a single lightning flash. (After *Gurnett and Inan* [1988].)

propagation (or *ray*) vectors. These high wave-normal vectors lie outside the transmission cone and generally prevent nonducted whistlers from being monitored on the ground.

The propagation path of nonducted whistlers depends on the location of the plasmapause and on the *L*-shell at which the causative sferic couples into the magnetosphere [*Jasna et al.*, 1990]. Though not restricted to propagation along magnetic field lines, nonducted whistlers tend to become field-aligned after multiple reflections within the plasma which occur alternately on either side of the geomagnetic equator. Many such reflections can take place before the whistler is absorbed in the cold plasma, as shown in Figure 2.8.

2.3.4 The Radiation Belts

The radiation belts of the Earth, sometimes called the Van Allen belts after the Iowa scientist who discovered them in 1958 [*Van Allen et al.*, 1959], are composed of energetic electrons and ions ("radiation") which are trapped in the geomagnetic field. The solar wind and the Earth's atmosphere are thought to be the source of these particles, which appear to be newly trapped (or *injected*) at much higher rates during solar-induced geomagnetic disturbances than during solar quiet times [*West et al.*, 1981].

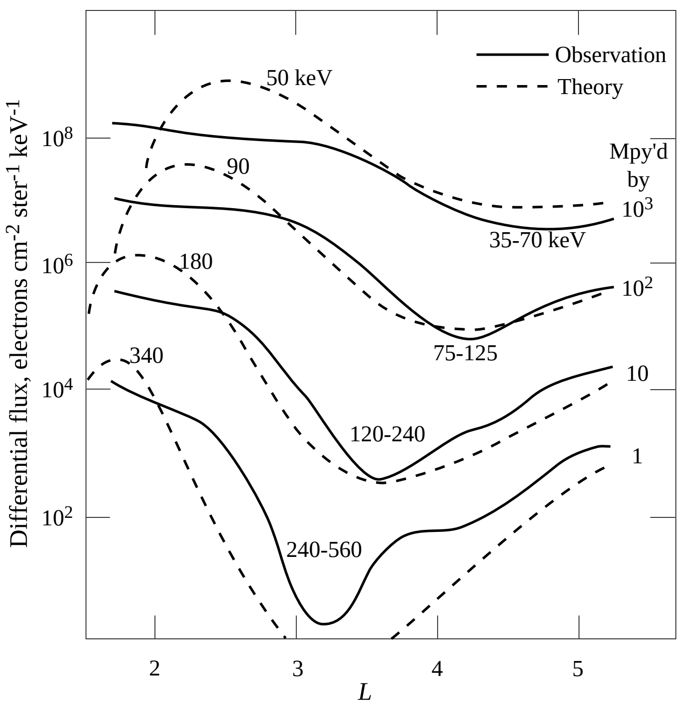

Fig. 2.9. Equatorial equilibrium profiles of radiation belt electron flux observed by Explorer 45 on December 15, 1971, compared with theoretical predictions. The theoretical profiles, shown for energies corresponding to the geometric mean of the four Explorer 45 energy channels, were obtained from the model of *Lyons and Thorne* [1973]. The 180-, 90-, and 50-keV curve pairs have been multiplied by 10^1, 10^2, and 10^3 respectively to more clearly display the data. (After *Lyons and Williams* [1975*a*].)

When the geomagnetic field has remained undisturbed for a few days, spatial and energy distributions of radiation belt particles tend towards an equilibrium structure that has been monitored by satellites for several years [e.g. *Lyons and Williams*, 1975*a*, 1975*b*; *West et al.*, 1981]. This population structure, characterized by an *inner belt* and *outer belt* separated by a local minimum known as the *slot region*, can be clearly seen in Figure 2.9. Less clear, however, are the reasons for this equilibrium structure and the relative significance of the various source and loss processes that lead to it. Chapter 6 takes up these issues in greater depth.

The energies of radiation belt electrons range from a few keV to over one MeV, corresponding to relativistic velocities (Figure 2.10). One consequence of such velocities is that a group of electrons scattered by a magnetospheric radio wave tends to continue moving as a localized burst, despite a possibly wide range of constituent energies.

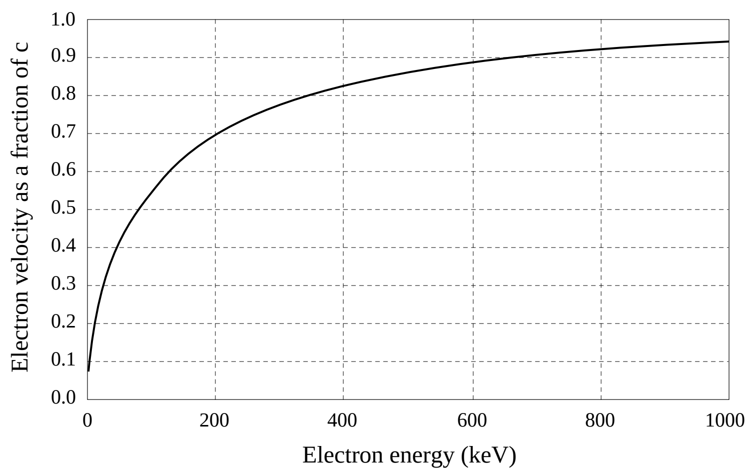

Fig. 2.10. Relativistic electron velocity as a function of energy. At relativistic speeds, electrons with very different energies can possess similar velocities.

Radiation belt dynamics

A charged particle trapped in the geomagnetic field is described by its kinetic energy E (usually expressed in eV), its L-shell, and its *equatorial pitch angle* α_{eq}. Pitch angle α is defined as the angle of the particle's helical trajectory relative to field line on which the particle is trapped, where $\alpha = 0°$ represents a particle moving parallel to the field line and $\alpha = 90°$ represents a particle moving in a circle perpendicular to the field line (Figure 2.11). The equatorial pitch angle α_{eq} is the pitch angle of the particle when crossing the geomagnetic equator.

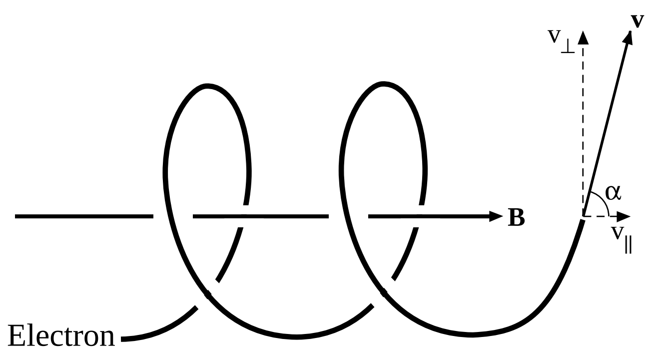

Fig. 2.11. Nomenclature for particle dynamics. The velocity **v** of a particle gyrating in the reference frame of a constant magnetic field **B** can be decomposed into a field-parallel component ($v_{||}$) and a field-perpendicular component ($v_\perp$). The angle α between **v** and **B** is called the pitch angle. The diagram shows the behavior of an electron; the sense of gyration is opposite for positively charged particles.

Under the influence of the geomagnetic field, the charged particles of the radiation belts *gyrate* in a helical motion, *bounce* between the Northern and Southern Hemispheres, and *drift* azimuthally around the Earth. This dissertation is mainly concerned with the gyration and bounce behavior of radiation belt electrons; the reader should consult *Roederer* [1970] for a comprehensive treatment of radiation belt dynamics.

Electrons are trapped in a bouncing motion between hemispheres by the increase in geomagnetic field strength as they near the Earth. The converging magnetic field lines

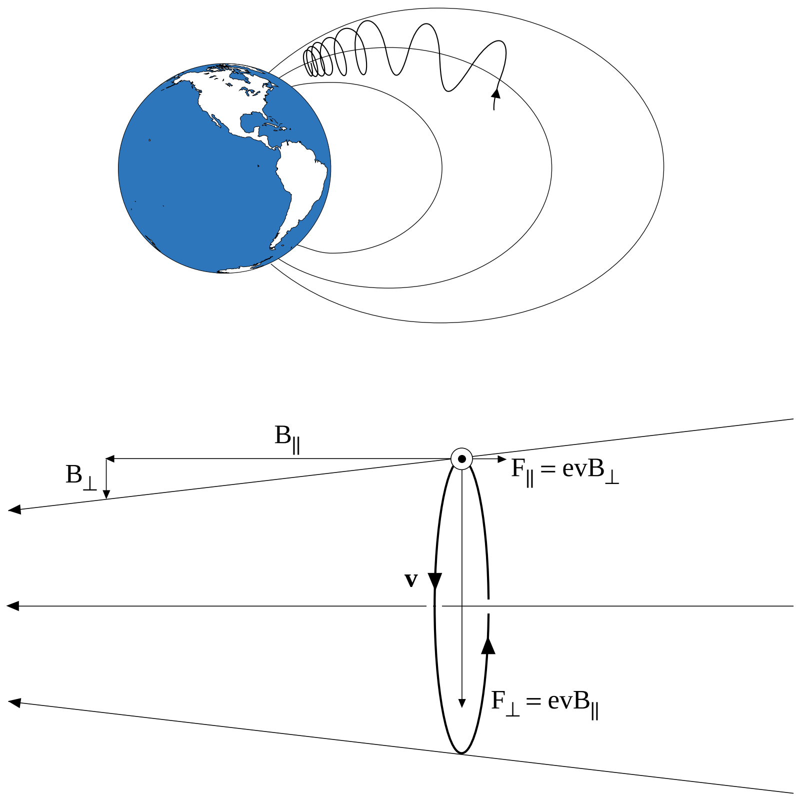

Fig. 2.12. Magnetic trapping of a charged particle. Converging magnetic field lines exert a force $F_{\parallel}$ on a gyrating particle, eventually causing it to "mirror" and return towards the opposite pole, where the same process will occur again. Particles thus trapped can remain in the radiation belts for decades. The behavior of a positively charged particle is shown here.

result in a force on the gyrating electrons which eventually brings their pitch angle to 90°, and then sends them back along the field lines to encounter the opposite hemisphere (Figure 2.12). This process is called *mirroring* and occurs when the magnetic field reaches a given strength, known as the *mirror field* (B_m), which in turn depends on the electron's equatorial pitch angle. The mirror field for a particle with a given equatorial pitch angle and on a given field line is

$$B_m = \frac{B_{eq}}{\sin \alpha_{eq}^2}. \tag{2.7}$$

The altitude above the Earth's surface corresponding to this mirror field is called the *mirror height* (h_m).

2.3.5 Electron Precipitation

Radiation belt electrons with low equatorial pitch angles have mirror heights near or in the atmosphere. Electrons whose mirror heights are below about 100 km altitude suffer collisions with atmospheric molecules on every bounce. Each encounter with the atmosphere scatters these electrons in pitch angle and prevents a portion of them from returning to the radiation belts [*Berger et al.*, 1974]. After several bounces most of these electrons are lost from the belts. This process is known as *electron precipitation* (Figure 2.13).

The maximum equatorial electron pitch angle for which precipitation is likely to occur is called the equatorial *loss cone* angle (α_{eq}^{lc}) and is illustrated in Figure 2.14*a*. Using ζ to represent mirror height as a fraction of Earth radius

$$\zeta = \frac{R_\oplus + h_m}{R_\oplus}, \tag{2.8}$$

the loss cone in a dipole field can be expressed in terms of mirror height as [*Inan*, 1977]

$$\alpha_{eq}^{lc} = \sin^{-1}\left(\frac{\zeta^3}{L^2\sqrt{4L^2 - 3\zeta L}}\right)^{\frac{1}{2}}. \tag{2.9}$$

For example, for $L = 2$ and $h_m = 100$ km, $\alpha_{eq}^{lc} = 16.8°$; however, because the geomagnetic field is not perfectly dipolar even at the Earth's surface (Figure 2.4), true loss cones may differ from these dipole estimates as shown in Figure 2.14*b*.

2.3.6 Whistler-Electron Interactions

Dungey [1963] and *Cornwall* [1964] independently recognized that cyclotron resonance would be possible between circularly polarized whistler waves and gyrating electrons moving in the opposite direction along a field line. During such an encounter, the electron "sees" a doppler-shifted wave frequency equal to its own gyrofrequency. This case of cyclotron resonance, sometimes called *gyroresonance*, was expressed for relativistic electrons by *Cornwall* [1964] as

$$\omega_H = \gamma\omega - \gamma k_\parallel v_\parallel \tag{2.10}$$

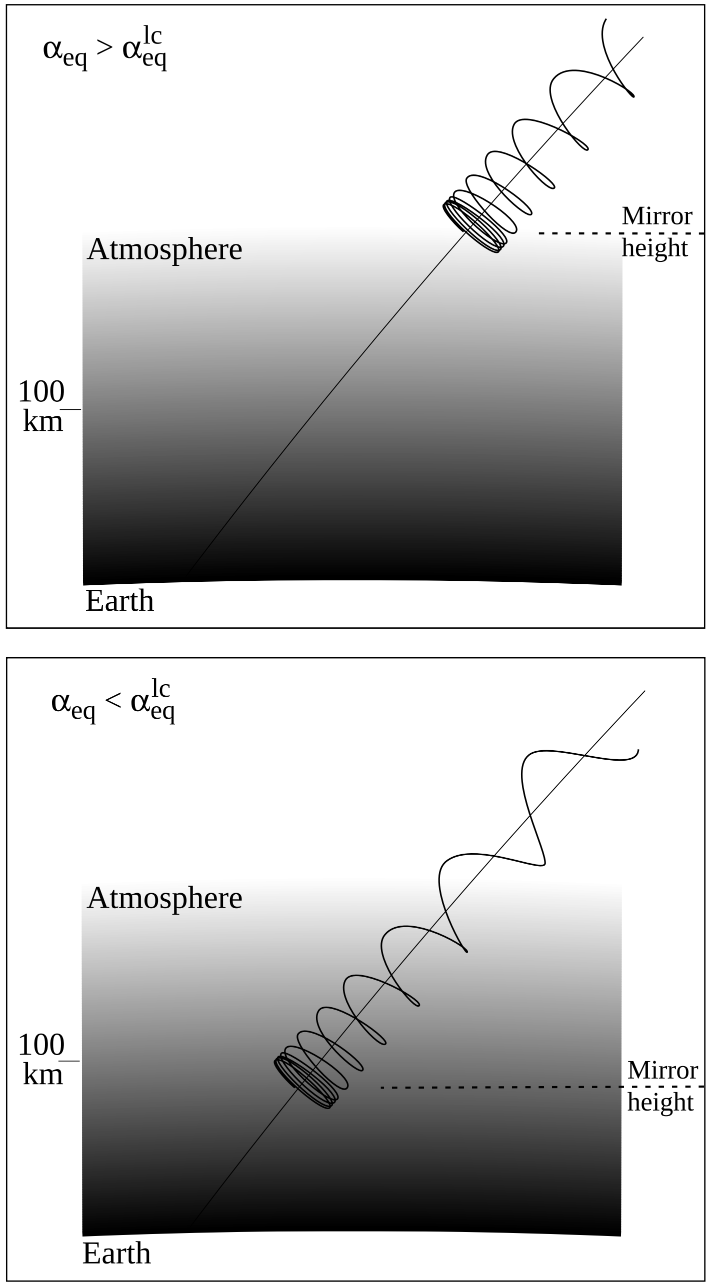

Fig. 2.13. Electron precipitation. Due to repeated collisions with atmospheric molecules, radiation belt electrons with mirror heights below about 100 km altitude are not stably trapped in the belts and are lost after several bounces, depositing their energy in the atmosphere. The equatorial electron pitch angle (α_{eq}) below which an electron will thus precipitate is called the *loss cone* angle (α_{eq}^{lc}).

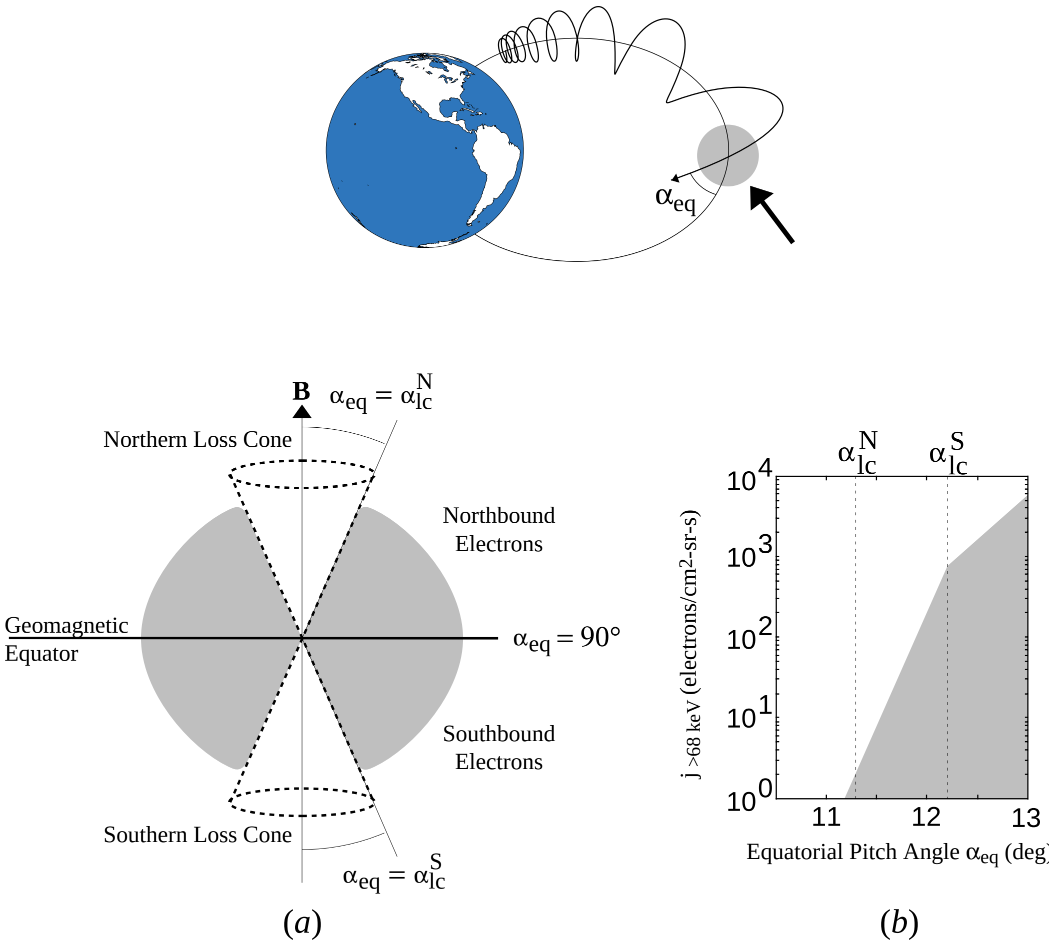

Fig. 2.14. The loss cone. Precipitation removes from the radiation belts those electrons with equatorial pitch angles less than the loss cone angle α_{eq}^{lc}. (*a*) pictorially represents the resulting equatorial distribution of electron pitch angles. The asymmetry of the geomagnetic field at the longitudes of the South Atlantic Magnetic Anomaly (Figure 2.4) narrows the northern loss cone relative to the southern. This asymmetry leads to equatorial pitch-angle distributions which exhibit two cut-off points (*b*).

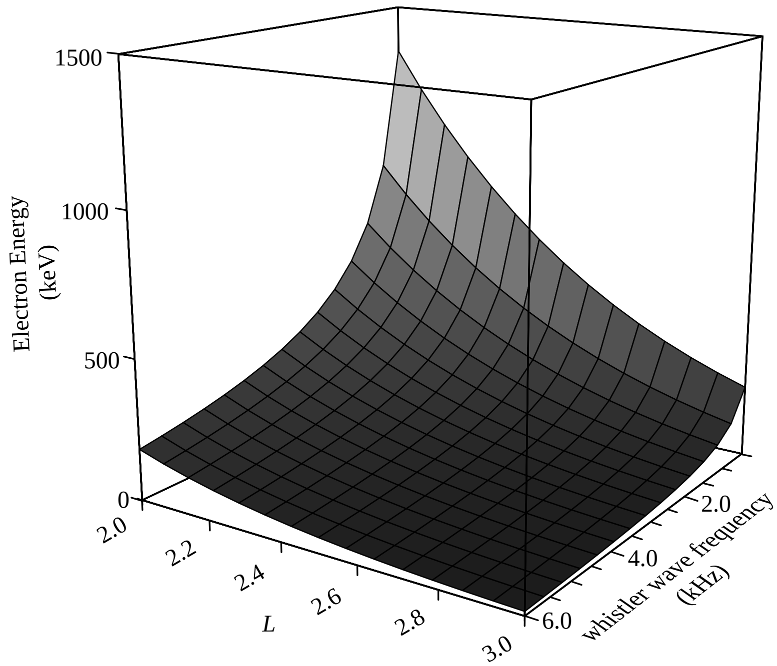

Fig. 2.15. Equatorial resonant energies of near-loss-cone electrons.

where the variables are

ω_H	local electron gyrofrequency
ω	whistler wave frequency
$k_\parallel$	component of the whistler wave number k parallel to the magnetic field
$v_\parallel$	component of electron velocity parallel to the magnetic field and opposite to $k_\parallel$; $v_\parallel$ is related to total velocity v and pitch angle α by $v_\parallel = v \cos \alpha$
γ	relativistic factor, equal to $1/\sqrt{1 - v^2/c^2}$.

Whistler-electron cyclotron resonance is capable of scattering electrons in pitch angle [*Inan*, 1987]. Electrons whose pitch angles are scattered into the loss cone will precipitate (Section 2.3.5); whistlers can therefore cause radiation belt losses. Since typical whistler-induced pitch angle scattering is expected to be small – less than 3° [*Inan et al.*, 1989] – only electrons with pitch angles on the edge of the loss cone, or *near-loss-cone electrons*, are likely to be scattered into it by a whistler.

It is useful to know the energy of scattered and precipitating electrons, because their energy determines the effects of their impact on the ionosphere. The energy of resonant near-loss-cone electrons can be determined from (2.10), and depends on the gyrofrequency and wave frequency in the region where resonance takes place. While whistler-electron resonance can occur well away from the geomagnetic equator [*Helliwell et al.*, 1990, and references therein], an estimate of resonant near-loss-cone electron energies can be obtained by assuming equatorial resonance. Further assuming a dipole field, we can find the energy of a whistler-resonant near-loss-cone electron as a function of whistler frequency and L as shown in Figure 2.15. The result indicates that whistler-resonant energies for mid-latitude near-loss-cone electrons are relativistic, being on the order of 100 keV to 1 MeV.

Cyclotron resonance can also take place between electrons and nonducted whistlers (e.g. *Inan and Bell* [1991]). Although the resonant electron energies are much lower than those for ducted whistlers, a much larger quantity of electrons appear to be scattered: recent analysis by *Jasna et al.* [1992] indicates that the total energy deposited in the atmosphere by 100 eV electrons precipitated by nonducted whistlers could be up to 30 times greater than the total energy deposited by relativistic electrons precipitated by ducted whistlers. Precipitation associated with nonducted whistlers would be difficult to detect with subionospheric VLF radio as was discussed in Section 1.2, however, because the particle energies would be too low for penetration into the Earth-ionosphere VLF waveguide.

3

Data Acquisition and Analysis

The data presented in this dissertation consist of broadband VLF recordings of whistlers and sferics from Palmer Station, Antarctica, and simultaneous narrowband recordings of subionospheric signal amplitudes observed at Palmer and at other sites. This chapter explains the methods used for the acquisition and subsequent analysis of these data.

3.1 DATA ACQUISITION

All broadband and narrowband data depend on the Geostationary Operational Environmental Satellites (GOES) for time-of-day with an accuracy of $\pm$2.0 ms. Radio observations at Palmer Station were made with two orthogonal 78 m^2 loop antennas aligned to local magnetic north-south and east-west, while other sites relied on single, smaller loop antennas. A photograph of the monitoring facility at Palmer Station is shown in Figure 3.1.

3.1.1 Narrowband Measurements

A block diagram of the narrowband data acquisition system used at Palmer is shown in Figure 3.2; similar systems were used at other sites. VLF and LF signals were monitored using narrowband receivers [*Wolf*, 1990], whose 500 Hz bandwidth passes most of the energy in minimum-shift-keying (MSK) and frequency-shift-keying (FSK) modulated signals [*Carlson*, 1986]. MF (AM radio) signals were acquired with narrower (200 Hz) filtering to

Fig. 3.1. The author in front of the VLF observatory at Palmer Station, Antarctica. The 468 MHz helical antenna mounted to the tower at left is for reception of the GOES time-of-day signal.

isolate the AM carrier. The detected envelopes of all receiver outputs were sampled at 100 Hz, then averaged on site for recording with lower effective sampling rates of 10, 20, or 50 Hz [*Shafer*, 1988].

The communication and navigation transmitters whose subionospheric VLF, LF and MF signals were monitored for this research are listed in Table 3.1, while the sites at which these signals were observed are listed in Table 3.2. In the following chapters, signal paths are referred to by abbreviation; for example, NPM–PA denotes the NPM to Palmer signal path. All signal paths referred to are assumed to describe a great circle arc (Figure 3.3).

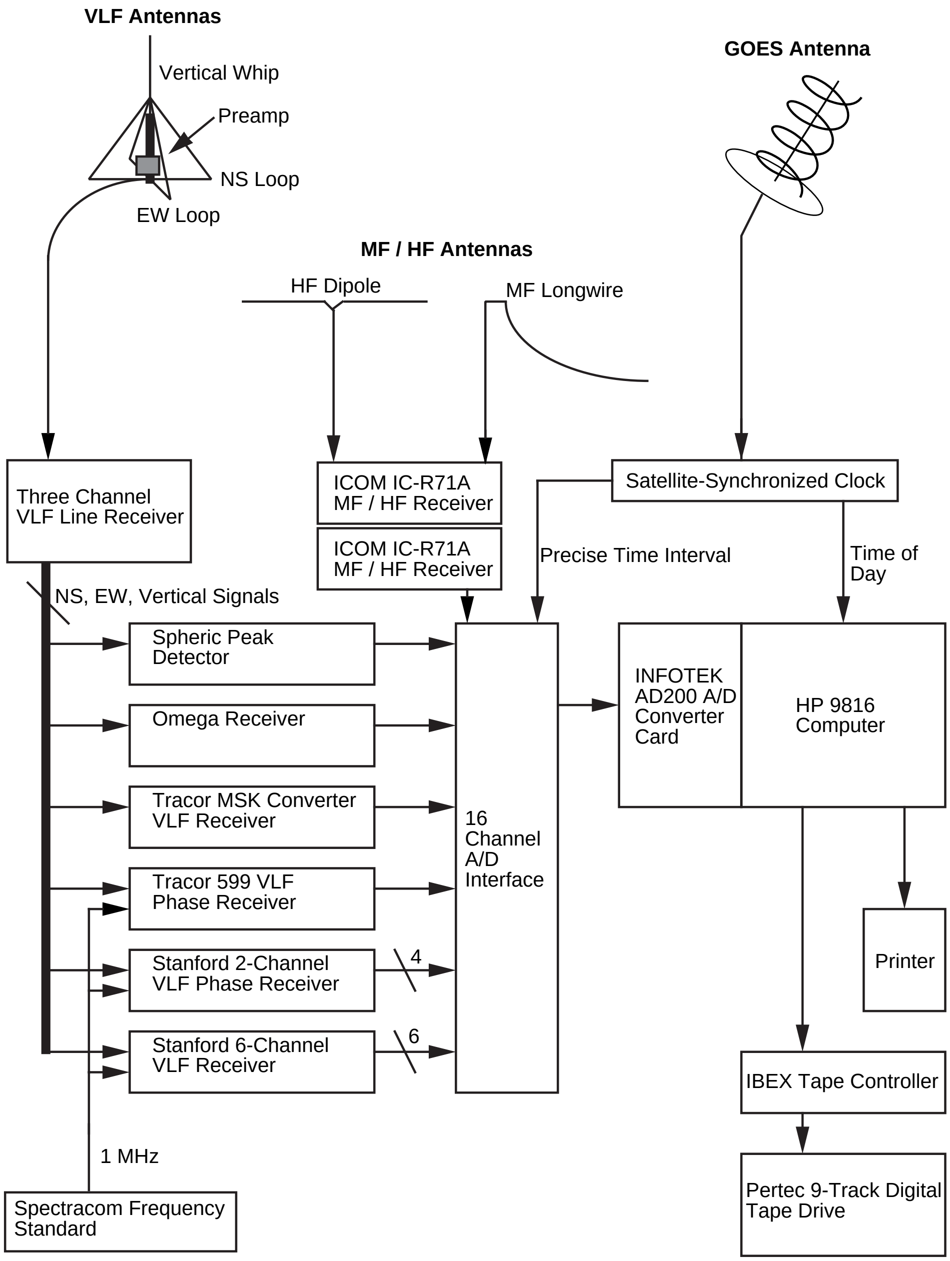

Fig. 3.2. The narrowband data acquisition system in use at Palmer Station. The 1988–1990 configuration is shown. The Tracor equipment was removed in 1990, and the MF/HF receivers were retrograded for repair in 1992.

TABLE 3.1. Transmitters.

Call Sign	Transmitter	Mod.	Carrier (kHz)	Position	azimuth at PA[b]
	Ω Argentina	CW[a]	12.9	43°S 65°W	357.8°
NSS	USN Maryland	MSK	21.4	39°N 76°W	350.1°
NPM	USN Hawaii	MSK	23.4	21°N 158°W	275.9°
NAA	USN Maine	MSK	24.0	45°N 67°W	357.6°
NLK	USN Washington	MSK	24.8	48°N 122°W	318.5°
NAU	USN Puerto Rico	MSK	28.5	18°N 67°W	[c]
	USAF Nebraska		48.5	42°N 98°W	[c]
LU14	Río Gallegos, Argentina	AM	830	52°S 69°W	345.8°
CD96	Punta Arenas, Chile	AM	960	53°S 71°W	339.9°

[a] ten second cycle of eight pulses, four on frequency shown
[b] in degrees clockwise from true north, assuming great circle propagation
[c] signals as observed at Palmer were weak, not used in azimuth study

TABLE 3.2. Receivers.

Site	Location	L	Position	Transmitters monitored
AR	Arecibo, Puerto Rico	1.34	18°N 67°W	NSS,NPM,NAA,NLK,NAU,48.5
HU	Huntsville, Alabama	2.13	35°N 87°W	NSS,NPM,NAA,NLK,NAU,48.5
LM	Lake Mistissini, Québec	4.71	50°N 75°W	NSS,NPM,NAA,NLK,NAU,48.5
PA	Palmer Station, Antarctica	2.42	65°S 64°W	NSS,NPM,NAA,NLK,ΩARG,LU14[a],CD96[b]

[a] LU14 was off the air for all cases in this dissertation except 2 April 1990.

[b] NAU and 48.5 were also monitored at PA but were too weak for useful analysis.

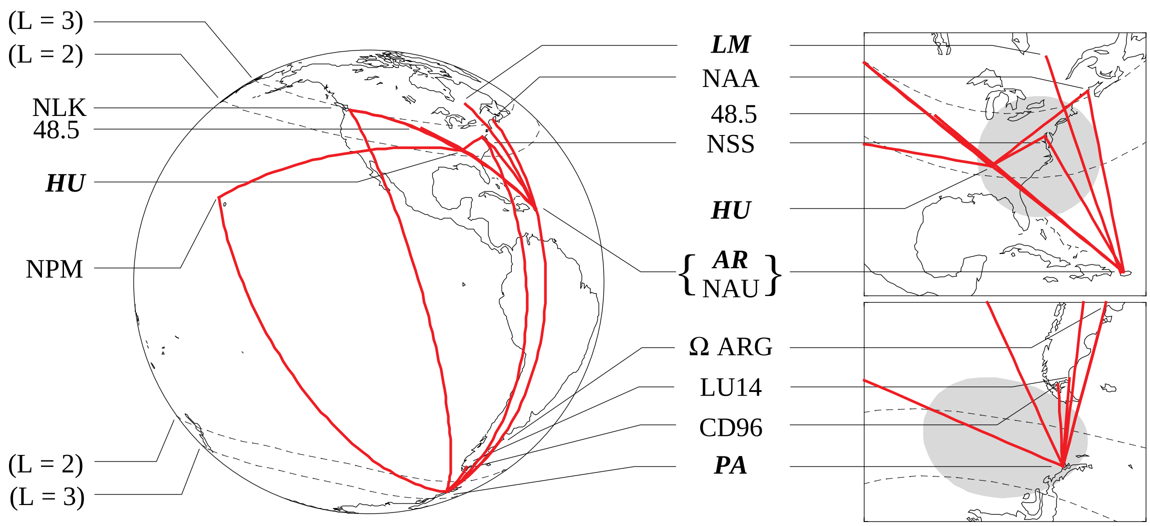

Fig. 3.3. The great-circle paths of signals monitored for this experiment. The transmitters are listed in Table 3.1, and the receivers are listed in Table 3.2. The right-hand panels show closeups of the path segments discussed in this dissertation. The shaded areas indicate a 2000 km diameter region in the Northern Hemisphere and its geomagnetic conjugate in the Southern Hemisphere, representing zones which have a relatively high "conjugate coverage" of monitored signal paths.

3.1.2 Broadband Measurements

A block diagram of the broadband data acquisition system used at Palmer is shown in Figure 3.4. The implementation of the antennas, preamp and line receiver is described by *Paschal* [1977], while *Paschal* [1988] discusses the design of broadband VLF systems in general. Until May of 1992 all broadband data were recorded with a -20 dB filter above 9 kHz to protect the analog tape from saturation by strong 10–14 kHz navigation signals from the nearby Omega Argentina transmitter. The improved dynamic range ($\sim$90 dB) of the digital Pulse-Code-Modulated (PCM) tapes, used almost exclusively since May 1992, makes this filtering unnecessary.

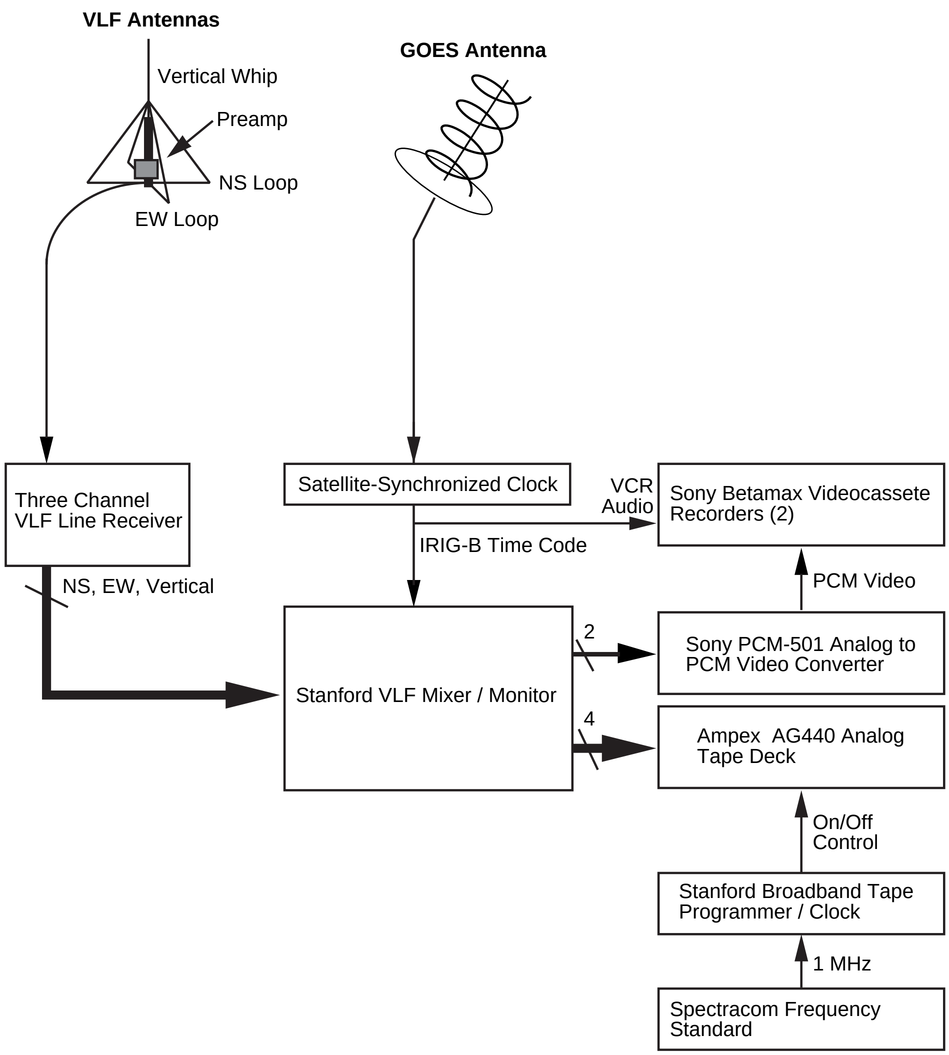

Fig. 3.4. The broadband data acquisition system in use at Palmer Station. The vertical whip antenna has been disconnected since October 1990 due to interference.

3.2 WHISTLER ANALYSIS

This dissertation includes analysis of three major characteristics of ducted whistlers observed on the ground: intensity, dispersion, and arrival azimuth. The following explains how these whistler characteristics were measured and interpreted.

3.2.1 Whistler Intensities

Whistler intensity measurements were made using data from the magnetic north-south loop antenna. All intensity values quoted in this dissertation represent the peak magnetic field intensity of whistlers between 3 and 6 kHz measured with a frequency resolution (Δf) of 61 Hz and with an error of $\pm$25%. Unless otherwise indicated, the intensity given for a multipath whistler is that of the strongest component.

3.2.2 Whistler Dispersion Analysis

Carpenter and Smith [1964] pioneered the systematic use of whistler dispersion analysis to estimate the *L*-shell and equatorial electron density (N_{eq}) associated with whistler ducts. The technique has been corroborated by comparison with satellite observations [*Carpenter and Anderson*, 1992].

The present research obtained *L* and N_{eq} from broadband VLF whistler dispersion measurements using the analytical approach of *Daniell* [1986*a*, *b*], applied in a Marquardt least squares parameter estimation [*Press et al.*, 1988]. The adoption and development of the Daniell/Marquardt method was motivated by the author's inability to obtain meaningful results for $L \lesssim 2.2$ whistlers using existing software, including the popular "sferic-and-two-point" method of *Bernard* [1973] and *Tarcsai et al.*'s [1975] Marquardt curve-fitting program, which relies on *Bernard*'s [1973] algorithm.

The analytical dispersion approximation of Daniell

In the following exposition any mention of *Daniell* will refer to both of G. J. Daniell's 1986 articles, which were published back-to-back in the same journal issue and essentially form one paper. *Daniell*'s term for equatorial gyrofrequency has been changed from $f_{H_{min}}$ to $f_{H_{eq}}$ for consistency, and a number of algebraic errors have been corrected. This exposition seeks to clarify *Daniell*'s results for future reference but does not attempt to prove them, since proof and interpretation are given in his articles. For brevity the discussion will also neglect the ionospheric contribution to dispersion [*Bernard*, 1973], although it has been included in all whistler analyses reported here.

Because whistler dispersion depends on the geomagnetic field B and the plasma density N_e encountered by the whistler while propagating (Figure 3.5), analysis of dispersion can be used to estimate those quantities. Defining dispersion in terms of time t as

$$D(f) \equiv t\sqrt{f}, \tag{3.1}$$

where $t = 0$ represents the time an atmospheric begins magnetospheric propagation as a whistler, *Helliwell* [1965] showed that

$$D(f) = \frac{1}{2c}\int_{path} \frac{f_H f_N}{(f_H - f)^{3/2}} \mathrm{d}s \tag{3.2}$$

where the variables are

- s distance along field-aligned whistler propagation path
- f_H gyrofrequency as a function of s, in Hz, related to geomagnetic field by equation (2.6)
- f_N plasma frequency as a function of s, in Hz, related to plasma density by equation (2.5)
- f signal frequency, in Hz.

While the geomagnetic field and hence the gyrofrequency can easily be determined anywhere along a dipole field line (equation 2.1), the distribution of plasma density results

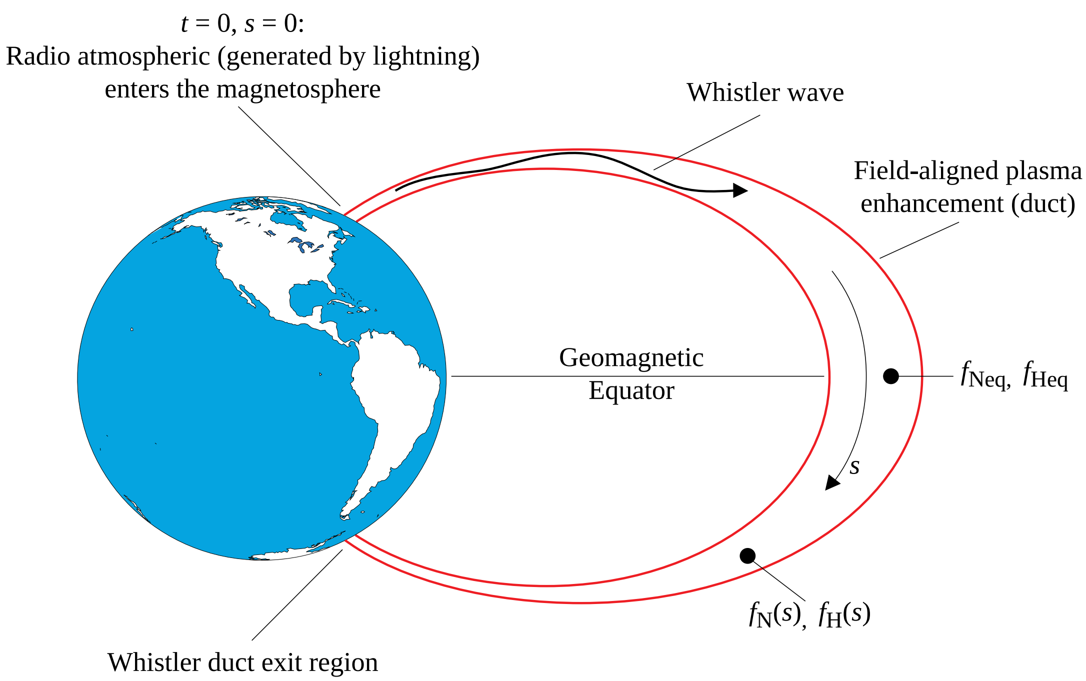

Fig. 3.5. Ducted whistler propagation. Frequency dispersion of a whistler propagating along a path s, guided by localized, geomagnetic-field-aligned enhancements of plasma density (ducts), depends on the plasma frequency $f_N(s)$ and the gyrofrequency $f_H(s)$ encountered. These characteristics depend in turn on plasma density and on geomagnetic field intensity, respectively. The hypothetical duct shown has been exaggerated in size for clarity; actual ducts are thought to be 200–500 km in diameter in the equatorial plane [*Angerami*, 1970].

from the diffusive equilibrium of plasma constituents [*Angerami and Thomas*, 1964] and an analytical expression for the variation of plasma frequency with s is more difficult to formulate. *Daniell* proposed the use of a *plasma variable* $G(\xi)$, defined as

$$G(\xi) \equiv \frac{1}{c\sqrt{f_{Heq}}} f_N(\xi)(1+\xi^2)\mathrm{d}s/\mathrm{d}\xi, \tag{3.3}$$

where the *pseudo-latitude* ξ is related to geomagnetic latitude via the expression

$$f_H = f_{Heq}(1+\xi^2). \tag{3.4}$$

Using this plasma variable and another variable η defined as

$$\eta \equiv 1 - \frac{f}{f_{Heq}}, \tag{3.5}$$

Daniell recast the dispersion integral as

$$D(\eta) = \int_0^\infty \frac{G(\xi)}{(\xi^2 + \eta)^{3/2}} \mathrm{d}\xi, \tag{3.6}$$

whose solution has the form

$$D(\eta) = \frac{\delta_1(\eta)}{\eta} + \delta_2(\eta) \ln \eta \tag{3.7}$$

with unknown functions $\delta_1(0) \neq 0$ and $\delta_2(0) \neq 0$. *Daniell* showed that the dispersion function $D(\eta)$ is fixed when the value of $\delta_1(0)$ and the function $\delta_2(\eta)$ are known.

By understanding the physical and analytical constraints on $G(\xi)$, $\delta_1(0)$ and $\delta_2(\eta)$, one can seek an integrable approximation for the integrand in (3.6) which can in turn lead to specification of $\delta_1(0)$ and $\delta_2(\eta)$ and thus to a useful expression for $D(\eta)$. One condition demonstrated by *Daniell* is that

$$\delta_1(0) = G(0), \tag{3.8}$$

representing plasma density at the equator. The dispersion integral imposes a second condition that, for large η, $D(\eta) \propto \eta^{-3/2}$, from which *Daniell* inferred that $\delta_2(\eta) \propto \eta^{-3/2}$ as well. These constraints led *Daniell* to suggest that $G(\xi)$ be represented as

$$G(\xi) \simeq G_0 + \frac{G_1 \xi^2}{(1 + \alpha\xi^2)} \tag{3.9}$$

where G_1 and α represent variation of plasma density with distance from the equator. Integrating (3.9) in (3.6) gives $\delta_1(0) = G(0) = G_0$ and $\delta_2(\eta) = -G_1/2(1 - \alpha\eta)^{3/2}$ which satisfy the above constraints on δ_1 and δ_2. If we assume further that $\alpha\eta \ll 1$ and $\alpha\xi^2 \ll 1$ for slowly varying plasma densities near the equator, and let $G_2 = -G_1/2$, then

$$G(\xi) \simeq G(0) - 2G_2\xi^2. \tag{3.10}$$

The constant G_2 thus expresses the small-scale second-order variation of plasma density near the equatorial plane.

Given the above expressions for δ_1 and δ_2, *Daniell* suggested that dispersion can be characterized for very small α and an intermediate constant a as

$$D(\eta) \simeq \frac{G(0) + a\eta}{\eta} + G_2 \ln \eta \tag{3.11}$$

or, in terms of frequency,

$$D(f) \simeq D_0 \frac{(f_{Heq} - A_D f)}{(f_{Heq} - f)} + G_2 \ln\left(1 - \frac{f}{f_{Heq}}\right), \tag{3.12}$$

where D_0 is the zero-frequency dispersion and A_D is a propagation path coefficient defined as

$$A_D \equiv 1 - \frac{G(0)}{D_0}. \tag{3.13}$$

Obtaining L *and* N$_{\mathrm{eq}}$

Visual inspection of a whistler in the frequency-time plane allows determination of (t, f) points along the whistler trace which represent its dispersion characteristic $D(f)$. Time $t = 0$ corresponds to the "causative" sferic (see Figure 1.4), which is identified visually from its consistent occurrence in a superposition of neighboring whistler-sferic examples, and is corrected for estimated subionospheric propagation delay to indicate the time the sferic originally coupled into the whistler duct in the opposite hemisphere. A propagation delay of 39 ms, the mean delay from North America to Palmer Station, was assumed for all causative sferics in this research. Dynamic frequency-time spectrograms from which the (t, f) pairs were scaled, such as those shown in Figures 2.6 and 2.7, were generated using the Fast Fourier Transform; however, recent work by *Mihovilović and Bracewell* [1992] suggests that a chirplet transform may allow more accurate discrimination between closely spaced components of multipath whistlers and thus more precise estimates of $D(f)$.

Given a whistler's $D(f)$ from inspection and curve-matching for the parameters in (3.12), one can obtain L from f_{Heq} using the relation

$$L = \left(\frac{f_{Heq}}{f_{H_\oplus}}\right)^{-\frac{1}{3}} \tag{3.14}$$

where $f_{H_\oplus}$ is the equatorial gyrofrequency at the Earth's surface. Combining the equatorial ($\xi = 0$) dipole field approximation $\mathrm{d}s/\mathrm{d}\xi = \sqrt{2}R_\oplus L/3$ with (3.3) and (3.13), we can find equatorial plasma frequency in terms of f_{Heq}, D_0 and A_D as

$$f_{Neq} = \frac{3c\sqrt{f_{Heq}}}{\sqrt{2}R_\oplus L} D_0(1 - A_D) \tag{3.15}$$

from which equatorial plasma density N_{eq} can be obtained with (2.5).

An approximation for G$_2$

Matching dispersion $D(f)$ as given by (3.12) to observed whistlers can be made easier by expressing G_2 in terms of D_0 and A_D, reducing the number of coefficients to match from four to three. Combining (3.3) and (3.10), we first express G_2 in terms of $f_N(\xi)$:

$$G_2 \simeq -\frac{G(0)}{2f_N(0)}\left(f_N(\xi) - \frac{f_N(0) - f_N(\xi)}{\xi^2}\right). \tag{3.16}$$

In the vicinity of the geomagnetic equator l'Hôpital's Rule can be applied to the final term (twice, assuming plasma frequency is symmetric about the equator so that $\mathrm{d}f_N(\xi)/\mathrm{d}\xi = 0$ for $\xi = 0$)

$$\lim_{\xi\to 0} \frac{f_N(0) - f_N(\xi)}{\xi^2} = -\frac{1}{2}\frac{\mathrm{d}^2}{\mathrm{d}\xi^2} f_N(\xi) \tag{3.17}$$

but for $\xi = 0$ we can expect that $\frac{\mathrm{d}^2}{\mathrm{d}\xi^2} f_N(\xi) \ll f_N(0)$, so that at the equator we have simply $G_2 \simeq -G(0)/2$ or, using (3.13),

$$G_2 \simeq -\frac{1}{2} D_0(1 - A_D). \tag{3.18}$$

Predetermination of $\mathrm{A_D}$

Attempts to fit coefficient A_D to low *L*-shell whistlers often fail due to inadequate whistler dispersion. Since A_D does not change rapidly with *L*, when analyzing whistlers in a small *L* range one can use fixed values of A_D determined *a priori* from existing dispersion models. These models predict the *L*-dependent behavior of Λ_n, the ratio of whistler nose frequency (i.e. the frequency of minimum whistler travel time [*Helliwell*, 1965]) to equatorial gyrofrequency:

$$\Lambda_n \equiv \frac{f_n}{f_{H_{eq}}}. \tag{3.19}$$

The following approach for obtaining a reasonable value of A_D as a function of Λ_n is very similar to the technique *Bernard* [1973] used to determine his A coefficient. Noting that at the whistler nose frequency

$$\left(\frac{\mathrm{d}D}{\mathrm{d}f}\right)_{f_n} = \frac{D_n}{2f_n}, \tag{3.20}$$

(3.12) and (3.18) can be rewritten at the nose frequency as

$$A_D = \frac{\frac{3\Lambda_n - 1}{\Lambda_n(1+\Lambda_n)} + \frac{(1-\Lambda_n)^2}{2\Lambda_n(1+\Lambda_n)}\left[\frac{2\Lambda_n}{1-\Lambda_n} + \ln(1-\Lambda_n)\right]}{1 + \frac{(1-\Lambda_n)^2}{2\Lambda_n(1+\Lambda_n)}\left[\frac{2\Lambda_n}{1-\Lambda_n} + \ln(1-\Lambda_n)\right]}. \tag{3.21}$$

Expression (3.21) has been cast in this form to show that the first term in the numerator is identical to *Bernard*'s [1973] expression for A.

Possible discrepancies between whistler exit L *and whistler duct* L

Above $L = 3$, *Strangeways et al.* [1982] observed discrepancies between whistler *L* values determined from dispersion analysis on the one hand and from direction-finding measurements on the other. While they attributed these discrepancies to whistler leakage from the sides of ducts in the vicinity of the duct exit regions, they also noted that the effect appeared to diminish with decreasing *L*. Since our data were obtained near $L = 2$, we will assume for the purposes of this dissertation that ducted whistlers remain at the same *L*-shell along their entire path.

3.2.3 Determination of Whistler Arrival Azimuth

The first goniometer measurements of whistlers by *Watts* [1959] opened the door to three decades of research on the determination of whistler arrival azimuths (also referred to as whistler direction finding or DF). While the goniometer continues to prove useful, several other techniques have also been developed and applied. These techniques include *lissajous analysis*, the four-parameter *A* and *B* methods, the *non-polarization error* method, the *DF tracking receiver* and the *Fourier goniometer* method used in this research.

The goniometer

Given signals $V_{NS}(t)$ from one loop antenna and $V_{EW}(t)$ from an orthogonal loop antenna, the goniometer simulates the output $V_g(t)$ of a rotating loop:

$$V_g = V_{NS}\cos(\omega t) + V_{EW}\sin(\omega t) \tag{3.22}$$

where ω is the simulated antenna rotation rate. Inspection of $V_g(t)$ for signal maxima and minima reveals the arrival azimuth of the signal subject to a 180° ambiguity. After its initial use on whistlers by *Watts* [1959], *Crary* [1961] extended the goniometer technique to include the signal $V_v(t)$ from a vertical antenna sensitive to the wave electric field, thereby eliminating azimuth ambiguity:

$$V_g = V_{NS}\cos(\omega t) + V_{EW}\sin(\omega t) + V_v. \tag{3.23}$$

Goniometer results become difficult to interpret in the presence of strong interfering signals with differing arrival azimuths, as is the case with multipath whistlers. Time resolution can also be poor, depending on the effective antenna rotation rate. Despite such problems, VLF goniometers have been successfully applied to whistler observations [*Bullough and Sagredo*, 1973; *Sagredo and Bullough*, 1973; *Strangeways et al.*, 1982].

Lissajous analysis

Lissajous analysis [*Crary*, 1961] involves direct X-Y observation of the voltages induced on orthogonal loops by the passage of radio waves. While suitable for observation of strong, stable signals such as VLF transmissions [*Cousins*, 1972], lissajous analysis is confusing and cumbersome to record for transient or weak signals such as whistlers.

The A and B methods

Cousins [1972] introduced the four-parameter *A* and *B* methods, which he designed for optimal application to horizontally-incident, vertically polarized waves and to sky waves with complex polarization, respectively. Both cases require the use of a vertical electric field antenna. He compared these methods analytically to goniometer techniques and suggested that the *B* method was most suitable for whistler analysis.

Cousins [1972] was the first to use digital signal processing to estimate whistler arrival azimuths. These efforts inspired the analysis and display methods used in the present research.

The Non-Polarization Error (NPE) method

The non-polarization error method was developed by *Tsuruda and Hayashi* [1975]. The goal of the method is the rejection of wave components which are not vertically polarized or horizontally incident on a crossed-loops-and-vertical antenna array, thereby removing polarization error from crossed-loop measurements. The method depends on elliptically polarized waves to perform correctly, and, ironically, does not respond well to signals which are already vertically polarized and horizontally incident, such as signals from distant VLF transmitters [*Leavitt et al.*, 1978]. *Tsuruda and Hayashi*'s [1975] implementation of the NPE method involved real-time analysis using a narrowband receiver, and was not well suited to investigation of frequency-varying signals.

Okada et al. [1977] offered another whistler DF approach called the "field-analyzing-method" which they likened to the work of *Crary* [1961]. Both the NPE method and the field-analyzing method were shown by *Strangeways* [1980] to be theoretically identical to the B method of *Cousins* [1972].

The tracking DF receiver or Poynting method

The tracking DF receiver of *Leavitt* [1975] provided easily recordable azimuth information for coherent VLF signals, and proved useful in analysis of ducted transmissions from Siple Station, Antarctica [*Leavitt et al.*, 1978]. The receiver determined the instantaneous Poynting vector components of the monitored signal in the horizontal plane, a technique since referred to as the Poynting method [*Strangeways*, 1980]. Although this receiver measured arrival azimuth in a narrow band, like those of *Tsuruda and Hayashi* [1975] and *Okada et al.* [1977], its tracking ability allowed it to follow coherent frequency-varying signals; it was, however, difficult to tune, gave inconsistent results in the presence of multipath, and could only track one signal at a time.

Strangeways [1980] showed that the Poynting method is theoretically identical to the A method of *Cousins* [1972].

Analyses of direction-finding methods

Systematic errors in the various DF methods when applied to ducted signals have been evaluated by several authors. *Tsuruda and Ikeda* [1979] compared azimuth results yielded by the goniometer, NPE and Poynting methods using ducted signals from Siple Station as input, but their conclusions were limited by lack of information on the source and propagation characteristics of the real signals used. *Strangeways and Rycroft* [1980] assumed point sources for duct exit regions and modeled subionospheric VLF propagation in terms of rays in order to estimate azimuth errors due to polarization and multiple ray paths. *Nagano and Mambo* [1989] predicted these errors using a spatially-spread source and full wave propagation theory.

While *Tsuruda and Ikeda* [1979] found that averaging in the time domain eliminated discrepancies among the three DF methods, *Strangeways and Rycroft* [1980] and *Nagano and Mambo* [1989] agreed that systematic azimuth errors are substantially reduced by averaging results over frequency in a $\sim$2 kHz bandwidth. *Strangeways and Rycroft* [1980] suggested that frequency averaging reduces errors to less than 10°, while *Nagano and Mambo* [1989] expected that such averaging would reduce errors close to zero.

Both *Strangeways and Rycroft* [1980] and *Nagano and Mambo* [1989] found the NPE method to be unreliable except for distances less than about 150 km from the duct exit region. *Nagano and Mambo* [1989] suggested that, after frequency averaging, the goniometer and Poynting methods give accurate and comparable results at distances as close as 50 km to the exit region.

An error source not considered in the recent literature is the effect of local terrain. *Horner* [1954] found that topography on the scale of tens to hundreds of meters could alter VLF arrival azimuths by as much as 8°, and recommended siting VLF antennas on the flat or on the tops of hills rather than on sloping ground.

Tkalcevic [1983] showed that horizontally polarized signals, such as one would expect to propagate subionospherically from cloud-to-cloud lightning flashes or from horizontally polarized transmitters such as Siple Station, are prone to azimuth errors as large as 90° when analyzed using upright crossed loop antennas. While this result suggests caution when applying DF techniques to horizontally polarized signals, *Tkalcevic*'s [1983] experimental observations indicated that the polarization of signals emerging from ducts, including whistlers, is more vertical than horizontal. Since the subionospheric transmitter signals monitored for this research (Table 3.1) are also vertically polarized, it is unlikely that azimuth results presented in this dissertation are significantly affected by horizontal polarization errors.

The Fourier goniometer

The arrival azimuth technique used in this research relies on Fast Fourier Transform (FFT) comparisons of whistler amplitudes and phases from two orthogonal antennas, an approach inspired by *Cousins* [1972] and similar to a method used by the British Antarctic Survey [*Smith and Yearby*, 1987]. The technique finds the major axis of polarization ellipses observed on the antennas just as a goniometer would, but with far better time and frequency resolution.

An ideal polarization ellipse observed on two orthogonal antennas can be represented as the sum of two counter-rotating complex phasors $A_0 e^{j\phi_0}$ and $A_1 e^{j\phi_1}$ (Figure 3.6). Given "real" digital data from the north-south loop antenna and "imaginary" digital data from the east-west loop antenna, a complex FFT will yield the real and imaginary components of the constituent counter-rotating phasors. The major axis angle θ of the polarization ellipse can then be easily obtained from the average of ϕ_0 and ϕ_1:

$$\theta = \frac{\phi_0 + \phi_1}{2}. \tag{3.24}$$

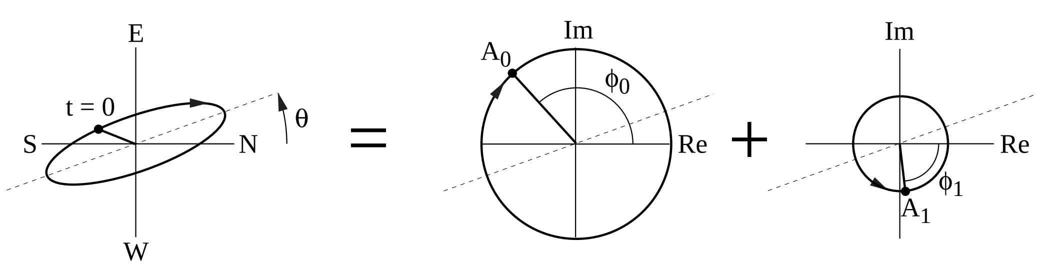

Fig. 3.6. Obtaining arrival azimuth with the complex FFT.

The theory of this technique bears similarity to that of the goniometer. If the east-west axis is treated as imaginary, the goniometer expression (3.22) can be written as

$$V_g = \Re\{(V_{NS} + jV_{EW})e^{-j\omega t}\}, \tag{3.25}$$

while the Fourier transform of the complex signal $V_{NS}+jV_{EW}$ is accomplished by integrating (3.25) instead of taking its real part:

$$F(\omega) = \int_{-\infty}^{\infty} (V_{NS} + jV_{EW})e^{-j\omega t}\mathrm{d}t. \tag{3.26}$$

This comparison suggests that the term "Fourier goniometer" would be appropriate for this technique.

Creation of polar arrival azimuth plots

The Fourier goniometer technique can be used dynamically to create two frequency-time "spectrograms" representing absolute magnitude and arrival azimuth. For each of many points along a visually selected whistler trace on the magnitude spectrogram, the angle of the major axis of the polarization ellipse observed on the antennas is determined from the corresponding "bin" on the azimuth diagram. The weight for that azimuth is then increased by the value of the magnitude "bin." The weighted azimuths are then formed into a polar plot for that whistler trace.

To demonstrate and verify this procedure, the Fourier goniometer was applied to VLF signals from the eight "Omega" navigation transmitters [*Swanson*, 1983]. These transmitters, located around the world, broadcast in eight-segment cycles repeated every ten seconds. Each transmitter provides four of the eight segments on common frequencies and the other four on a transmitter-unique frequency (UF) in the following pattern: 10.2 kHz, 13.6 kHz, $11\frac{1}{3}$ kHz, UF, UF, 11.05 kHz, UF, UF. The pattern is staggered among the eight transmitters so that no common frequency is transmitted by more than one station at a time. The Omega format is shown in Figure 3.7.

Figure 3.8 shows a dynamic spectrogram of Omega signals received at Palmer, obtained from magnitudes of the polarization ellipse major axes using the Fourier goniometer technique. The corresponding azimuth results for the top 35 dB of Figure 3.8 are shown in Figure 3.9. Using the weighting method just described, polar plots were generated for each

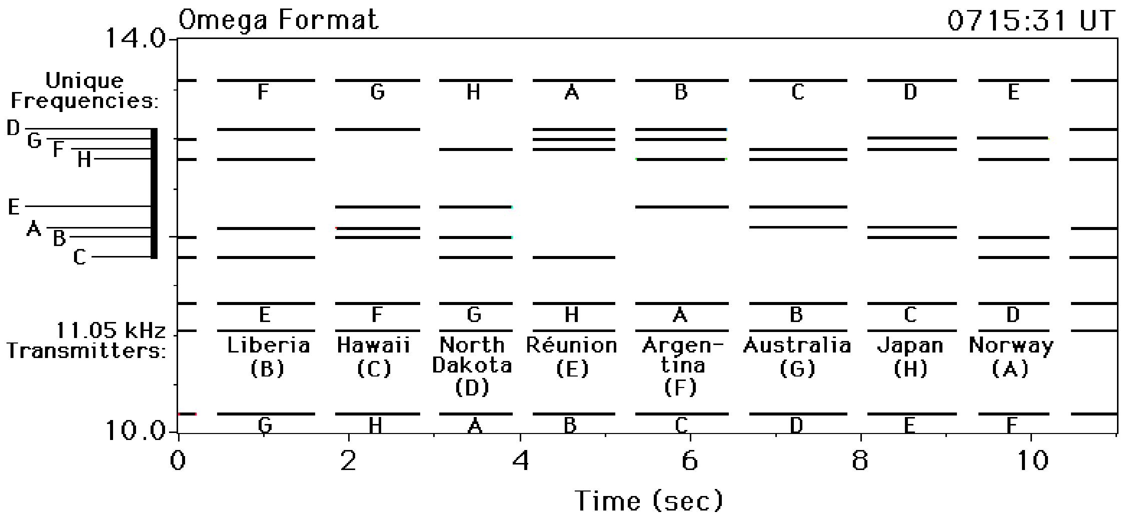

Fig. 3.7. The Omega transmitter format. Each of the eight transmitters broadcasts eight segments every ten seconds. The frequencies of 10.2, 11.05, $11\frac{1}{3}$, and 13.6 kHz are broadcast by each transmitter once per cycle, in addition to four pulses at a frequency unique to the transmitter.

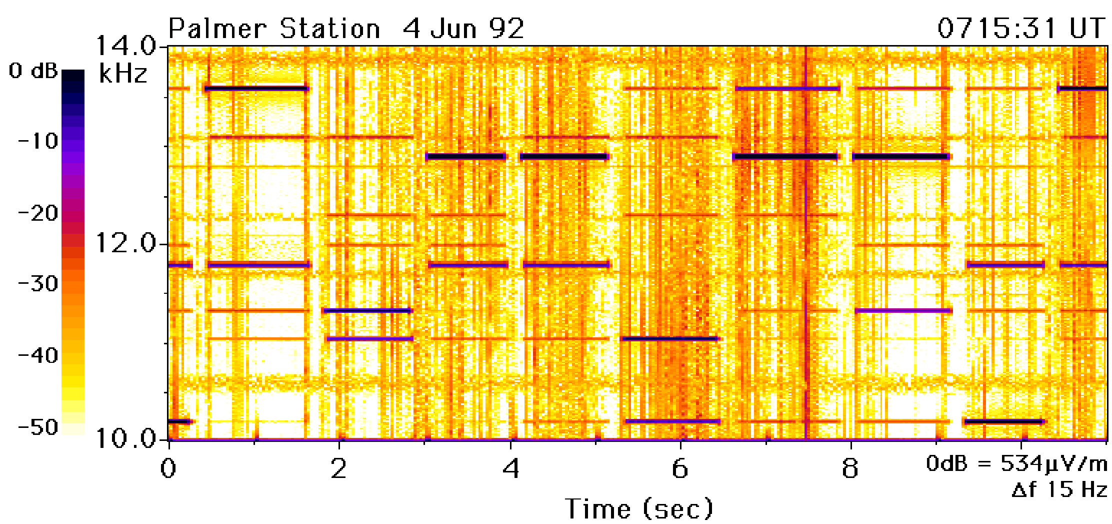

Fig. 3.8. Magnitudes of Omega pulses observed at Palmer Station. All eight transmitters can be seen at 11.05 kHz, at received signal strengths ranging from about 2 μV/m (Norway) to over 500 μV/m (Argentina).

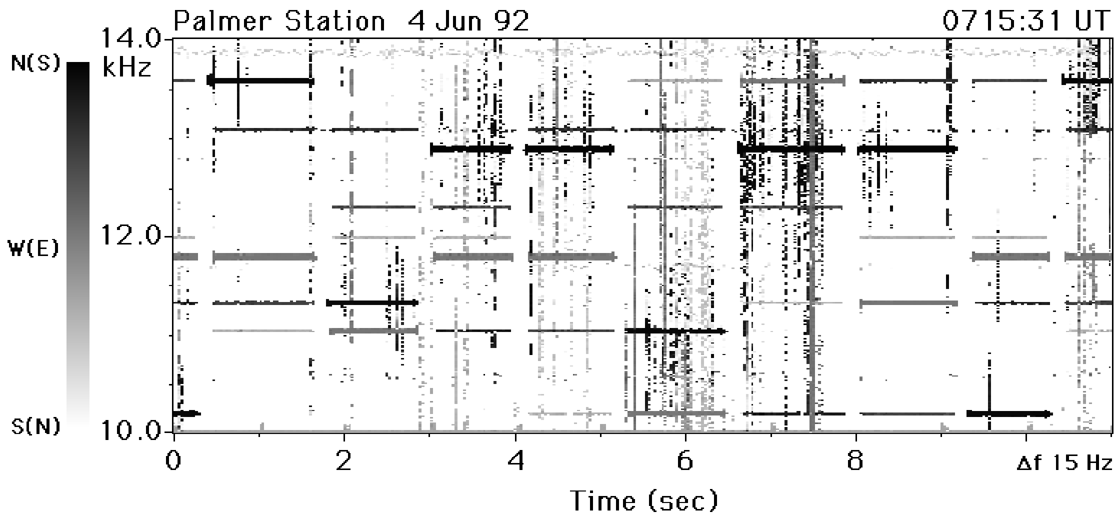

Fig. 3.9. Arrival azimuths of Omega pulses observed at Palmer Station. Azimuths corresponding to the top 35 dB of Figure 3.8 are shown, with different shades representing azimuths as shown in the bar (left). Each shade identifies two possible azimuths because of the 180° ambiguity inherent in the Fourier goniometer technique used here.

of the five Omega signals visible in Figure 3.9, and are compared against great circle arrival paths in Figure 3.10.

Errors

As shown in Figure 3.10, the signal azimuths observed tend to validate the Fourier goniometer technique. With the exception of Omega La Réunion, all signals were measured to arrive within 5° of their great circle azimuths. The apparent arrival of La Réunion from 10° to the south of its great circle azimuth is difficult to explain. The La Réunion signal was the weakest of the five transmissions analyzed, and its arrival azimuth may have been affected by propagation parallel to the Antarctic coast for several hundred km (Figure 3.11). Local, path-dependent terrain effects may also have played a role; the VLF loops at Palmer Station are situated about 600 m up the slope of a glacier, and *Horner* [1954] determined that summits or flat ground give more accurate results. On the other hand, *Tkalcevic* [1983] used the tracking DF receiver of *Leavitt* [1975] to measure several Omega arrival azimuths

Fig. 3.10. Polar arrival azimuth plots of signals from five Omega transmitters received at Palmer Station. All observed azimuths are within 5° of great circle paths, except that of La Réunion, which appeared to arrive from 10° S of its great circle path.

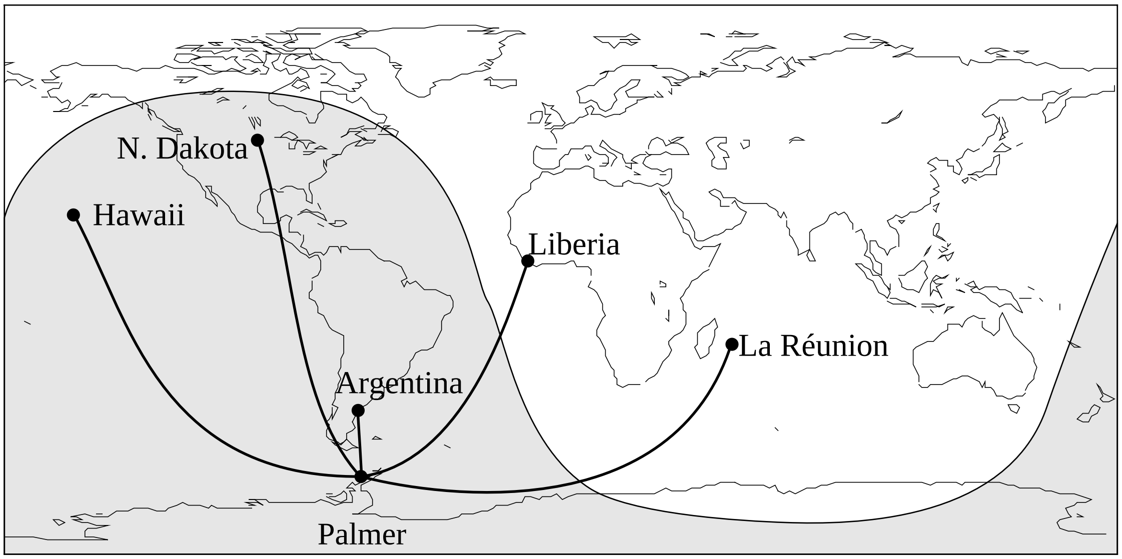

Fig. 3.11. Propagation of five Omega transmissions to Palmer Station at 0715 UT on June 4, 1992. The great circle propagation path of Omega La Réunion lies parallel to the Antarctic coast for several hundred kilometers. The day-night terminator is shown at 100 km altitude for reference.

at Palmer, including that of La Réunion, and found agreement with great circle paths of $\pm 4°$ in all cases.

The use of only two antennas gives rise to a 180° ambiguity in results; for all whistlers analyzed in this research, however, the determination of L-shells was sufficient to resolve the ambiguity. Alignment of the antennas is precise to within $\pm 5°$. Adding the worst-case goniometer azimuth error of $\pm 10°$ [*Strangeways and Rycroft*, 1980] and neglecting site-dependent effects, the estimated absolute azimuth error is less than $\pm 15°$.

By convention, arrival azimuths in all cases are given as degrees clockwise from geographic north.

3.3 IDENTIFICATION OF ASSOCIATIONS BETWEEN WHISTLERS AND SIGNAL PERTURBATIONS

We associate a whistler with a VLF signal perturbation in two ways. The preferred method, illustrated in Figure 3.12, requires the identification of a perturbation-associated “causative” atmospheric in the narrowband data [*Inan et al.*, 1988*b*] which coincides, allowing for propagation delay, with a whistler causative atmospheric observed in the Southern Hemisphere broadband data [*Carpenter and Smith*, 1964]. When narrowband signatures of causative atmospherics are not available, a whistler is considered to be “associated” with a signal perturbation if its descending frequency crosses 4 kHz within $\pm$0.5 s of the steepest part of the perturbation onset, a criteria adopted for convenience and for consistency with previous predictions [*Chang and Inan*, 1985] and observations [*Inan and Carpenter*, 1986]. The geophysical context of whistler-associated signal perturbations, including the definition and interpretation of causative sferics, onset delays and onset durations, is discussed in Chapter 1.

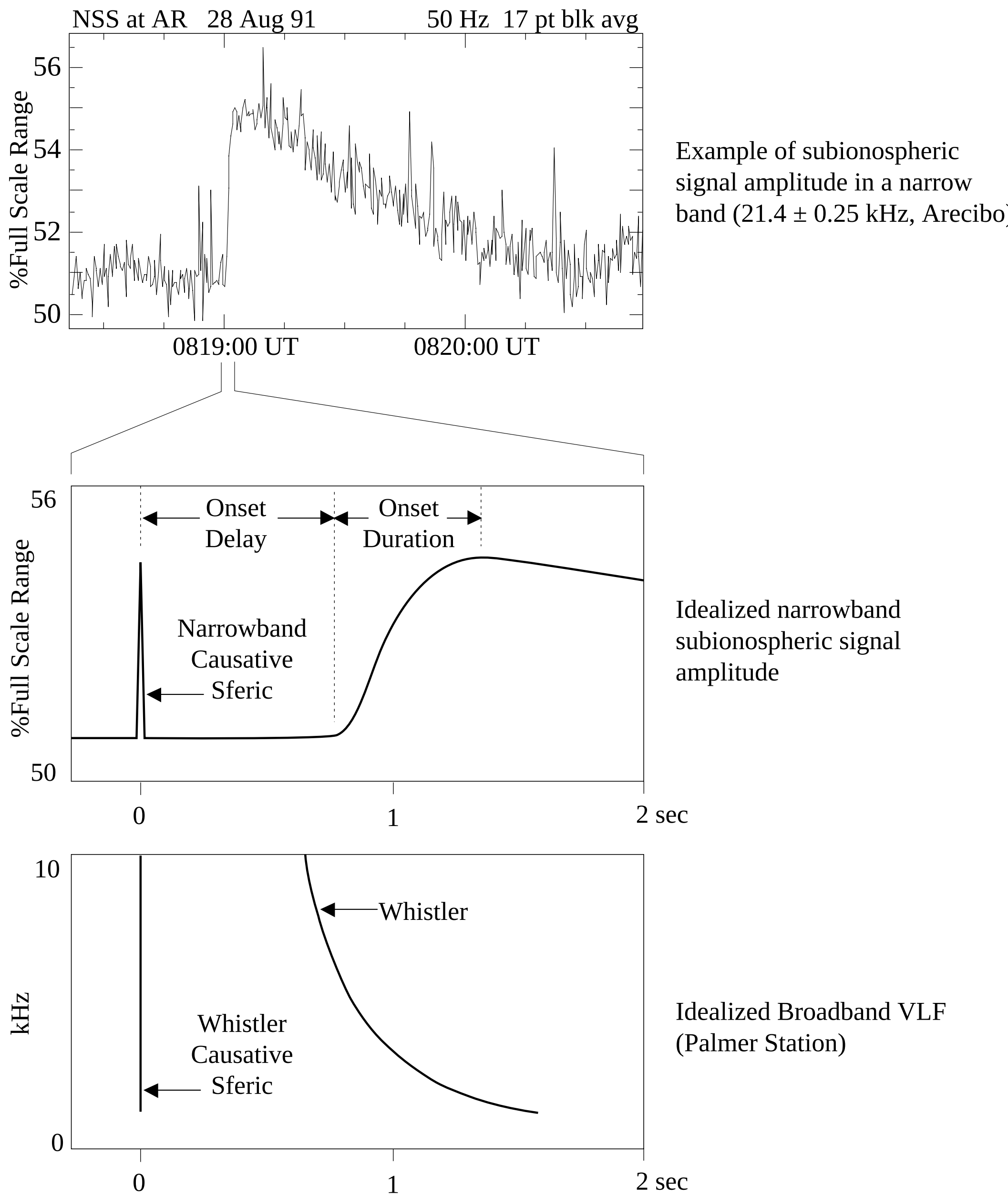

Fig. 3.12. Associating a signal perturbation with a whistler based on coincident reception of causative sferics. Close examination of whistler-associated subionospheric signal perturbations, for example this one observed on NSS at Arecibo, often reveals the impulsive radio signature of the causative lightning flash [*Inan et al.*, 1988*b*]. To verify that the signal perturbation is associated with a given whistler, this "narrowband causative atmospheric" can be compared in time with the "whistler causative atmospheric" observed by the broadband receiver at Palmer Station (see Section 3.2.2). "Full scale range" is the maximum signal level that the narrowband data acquisition system can record without saturation.

4

The Geomagnetic Conjugacy of Ionospheric Disturbances

Since *Dungey* [1963] and *Cornwall* [1964] showed theoretically that cyclotron resonance with whistlers could scatter radiation belt electrons into the bounce loss cone (Section 2.3.6), an unstated but common assumption has been that most electrons thus scattered would precipitate on their first encounter with the atmosphere. *Inan et al.* [1985*b*] showed that this assumption was inconsistent with satellite measurements of electrons scattered by man-made signals, and instead suggested that many loss cone electrons backscatter on contact with the atmosphere, bouncing between conjugate regions several more times before finally precipitating. *In situ* observations of whistler-associated loss-cone electron bursts by *Voss et al.* [1984] supported this hypothesis. These results implied that bouncing whistler-induced precipitation could create near-simultaneous ionospheric disturbance pairs in conjugate regions, but until now such disturbances have not been detected (the conjugate disturbances identified by *Dingle and Carpenter* [1981] occurred in association with magnetospheric VLF noise bursts, which are less frequent and much stronger than whistlers, and may have involved direct electron scattering into both northern and southern loss cones).

This chapter presents the first evidence, gathered from Arecibo, Puerto Rico (AR) and Palmer Station, Antarctica (PA), that ionospheric regions in both Northern and Southern

Hemispheres can be near-simultaneously and detectably disturbed in association with ordinary whistlers.* During a one hour period on March 21, 1989, the onsets of 129 out of 147 whistler-associated subionospheric signal perturbations measured at AR occurred within 1 s of signal perturbation onsets measured at PA. Similar activity occurred before and after this period, and on the preceding and following days. The observations are consistent with the disturbance of geomagnetically conjugate ionospheric regions by multiple bounces between hemispheres of bursts of radiation belt electrons, scattered in pitch angle by whistlers in the magnetosphere. Analysis of patterns of perturbations with corresponding whistler and lightning information from this period suggests that there were at least four distinct ionospheric disturbances, two in each hemisphere.

4.1 PERTURBATIONS ON CONJUGATE SUBIONOSPHERIC VLF/LF SIGNAL PATHS

During the morning of March 21, 1989, Arecibo and Palmer Station recorded several hundred perturbations on signals from five VLF and LF communication transmitters in the United States (Table 3.1). These perturbations were characteristic of "Trimpi" events (Chapter 1), having sudden (0.2 to 2 s) positive or negative onsets of up to 9 dB in amplitude followed by slow (10 to 100 s) recoveries to prior levels. Between 0900 and 1000 UT the perturbations were particularly large and frequent on the NSS and 48.5 kHz signals at Arecibo and on the NPM signal at Palmer Station. The latter signal path was perturbed at least twice as often as any other path recorded at either site, averaging four perturbations per minute. Partial maps of the ten signal paths monitored are shown in Figure 4.1.

For the purposes of this chapter, the signal perturbations observed at Palmer and Arecibo are henceforth referred to as "events," where an event is defined as a characteristic signal amplitude perturbation with a magnitude not less than 0.2 dB. Perturbations seen on different

---

* Much of this chapter was originally published as a journal article by W. C. Burgess and U. S. Inan in *Geophysical Research Letters*, volume 17, pp. 259-262, 1990, copyright by the American Geophysical Union [*Burgess and Inan*, 1990].

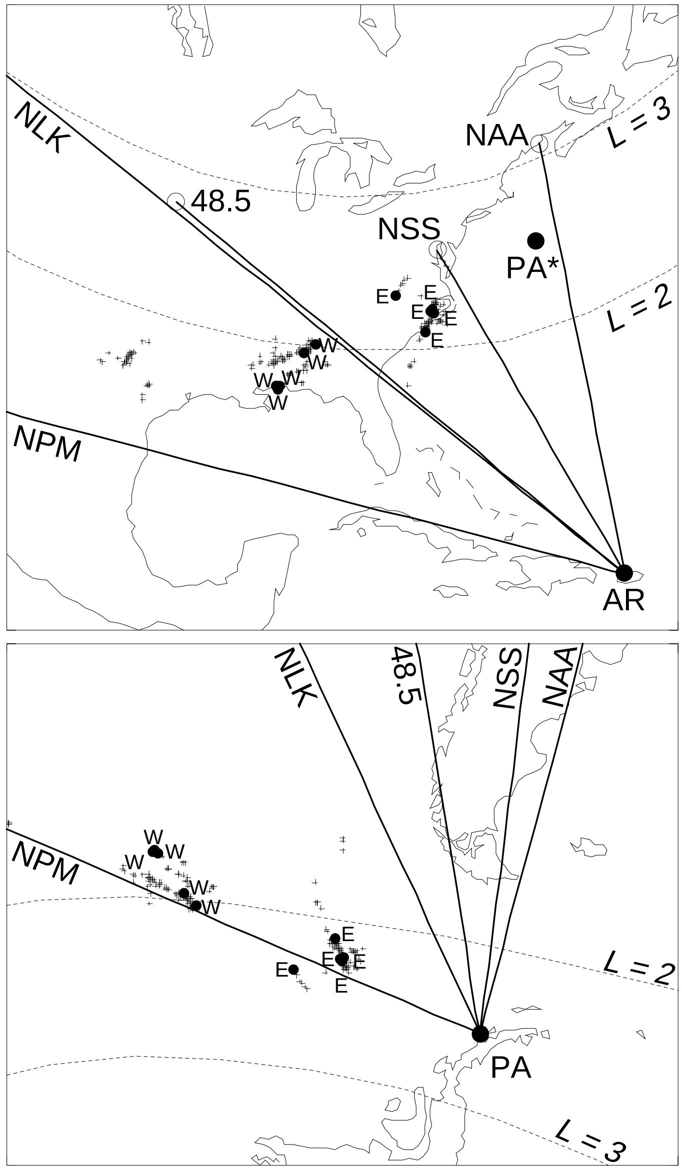

Fig. 4.1. Great-circle paths of subionospheric signals from five of the VLF/LF transmitters listed in Table 3.1 to Arecibo, Puerto Rico (AR) and Palmer Station, Antarctica (PA). Each cloud-to-ground lightning flash recorded by the SUNY-Albany detection network between 0940 and 0950 UT on March 21, 1989 is shown by a + in the upper panel to indicate general thunderstorm activity. Each of ten additional flashes time-associated with signal perturbations discussed in the text and occurring between 0900 and 1000 UT is marked with a •. The geomagnetic conjugates of all upper panel flashes are similarly marked in the lower panel. Of the ten specially marked flashes, the five labeled 'E' were associated with perturbations of NSS but not 48.5 kHz at Arecibo, while the five labeled 'W' were associated with perturbations of 48.5 kHz but not NSS at Arecibo; all ten flashes were associated with perturbations of NPM at Palmer. The footprints at 100 km altitude of L = 2 and L = 3 are shown for reference. PA* indicates the geomagnetic conjugate of Palmer Station.

signals at the same or different sites will constitute a single, simultaneously observed event when the perturbation onsets occur within one second of each other. The one-second criterion was applied because frequent atmospheric noise prevented systematic use of a finer threshold. Between 0900 and 1000 UT, 129 events were observed simultaneously at both Arecibo and Palmer. Such events accounted for 88% of the 147 events observed at Arecibo but only 51% of the 252 events observed at Palmer during that period, so that disturbances in the north were more likely to have counterparts in the south than vice-versa.

Assuming that a perturbed subionospheric signal indicates an ionospheric disturbance located within 200 km of the signal's great-circle path (Section 1.2), the patterns of perturbation simultaneity among the ten signal paths monitored would contain information on the location and extent of the responsible disturbances. As we shall see, two patterns of simultaneous events are of special interest in this chapter: events including NSS–AR and NPM–PA but not 48.5–AR, hereafter referred to as the "east group," and events including 48.5–AR and NPM–PA but not NSS–AR, hereafter referred to as the "west group." Examples of west group and east group simultaneous events are shown in Figure 4.2.

The disturbance information hidden in these patterns of simultaneity is, however, not easily revealed. The general case of ten signal paths involves 2^{10} possible combinations of perturbed and unperturbed signals, complicating display and analysis. This difficulty is depicted in Figure 4.3*a*, which indicates the signal paths perturbed in eight selected events displayed in chronological order. A simple method to reduce the complexity of Figure 4.3*a* is to re-order the events to maximize the contiguity of perturbation activity on given signal paths. A re-ordering scheme maximizing the contiguity of NPM–PA, NSS-AR, and 48.5–AR perturbations is offered in Figure 4.3*b* to clarify patterns of simultaneity associated with the east and west groups.

Using this re-ordering technique, Figure 4.4 summarizes patterns of simultaneity among the 270 events observed between 0900 and 1000 UT, and shows that west group and east group events constitute a significant portion of all conjugate events observed in that period.

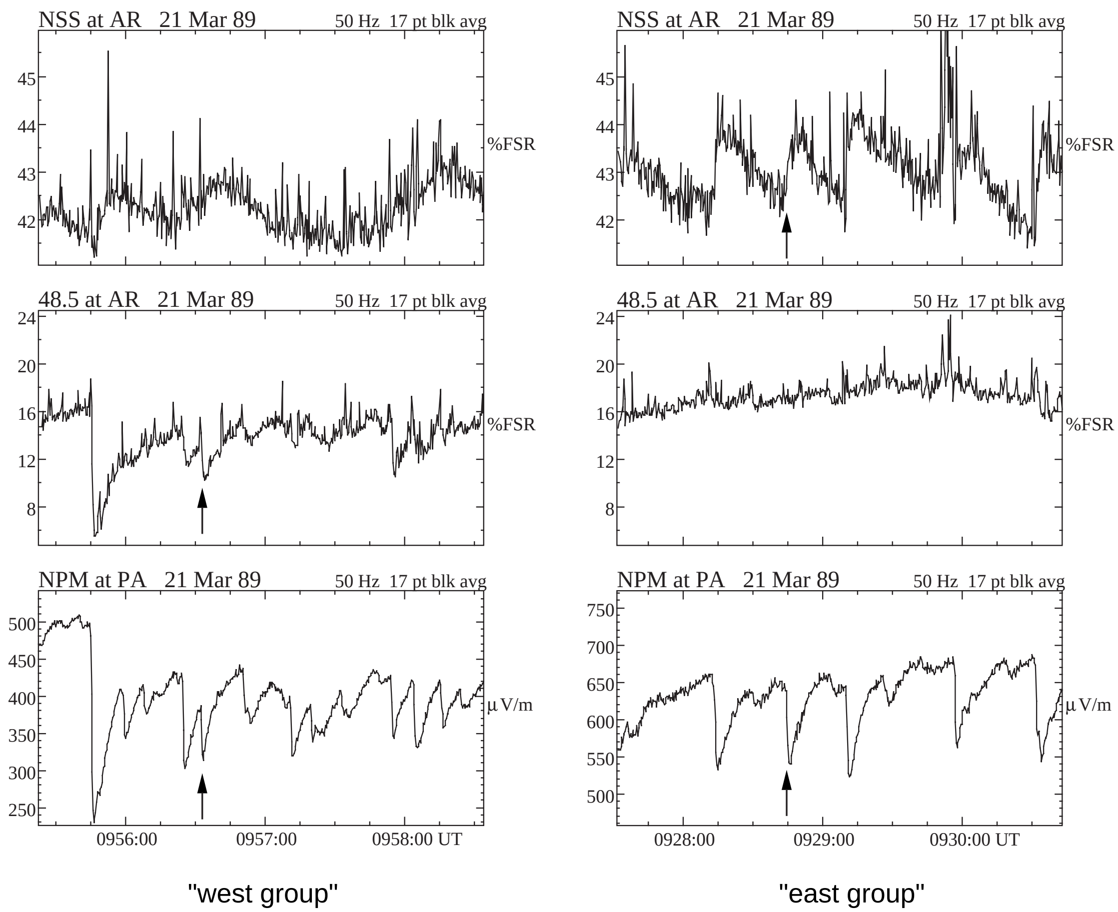

Fig. 4.2. Examples of subionospheric signal perturbations simultaneously observed in conjugate regions. The left panels show perturbations of NPM at Palmer and of 48.5 kHz but not (except for one case) NSS at Arecibo, referred to as "west group" events in this chapter. The right panels show perturbations of NPM at Palmer and of NSS but not 48.5 kHz at Arecibo, referred to as "east group" events in this chapter. In both, the onsets of many of the perturbations of NPM at Palmer occur within 1 s of perturbation onsets observed at Arecibo. The arrows indicate perturbations which are shown in greater detail in Figure 4.5. Where absolute signal amplitude calibration was unavailable, "%FSR" denotes percent of the acquisition system's full scale range.

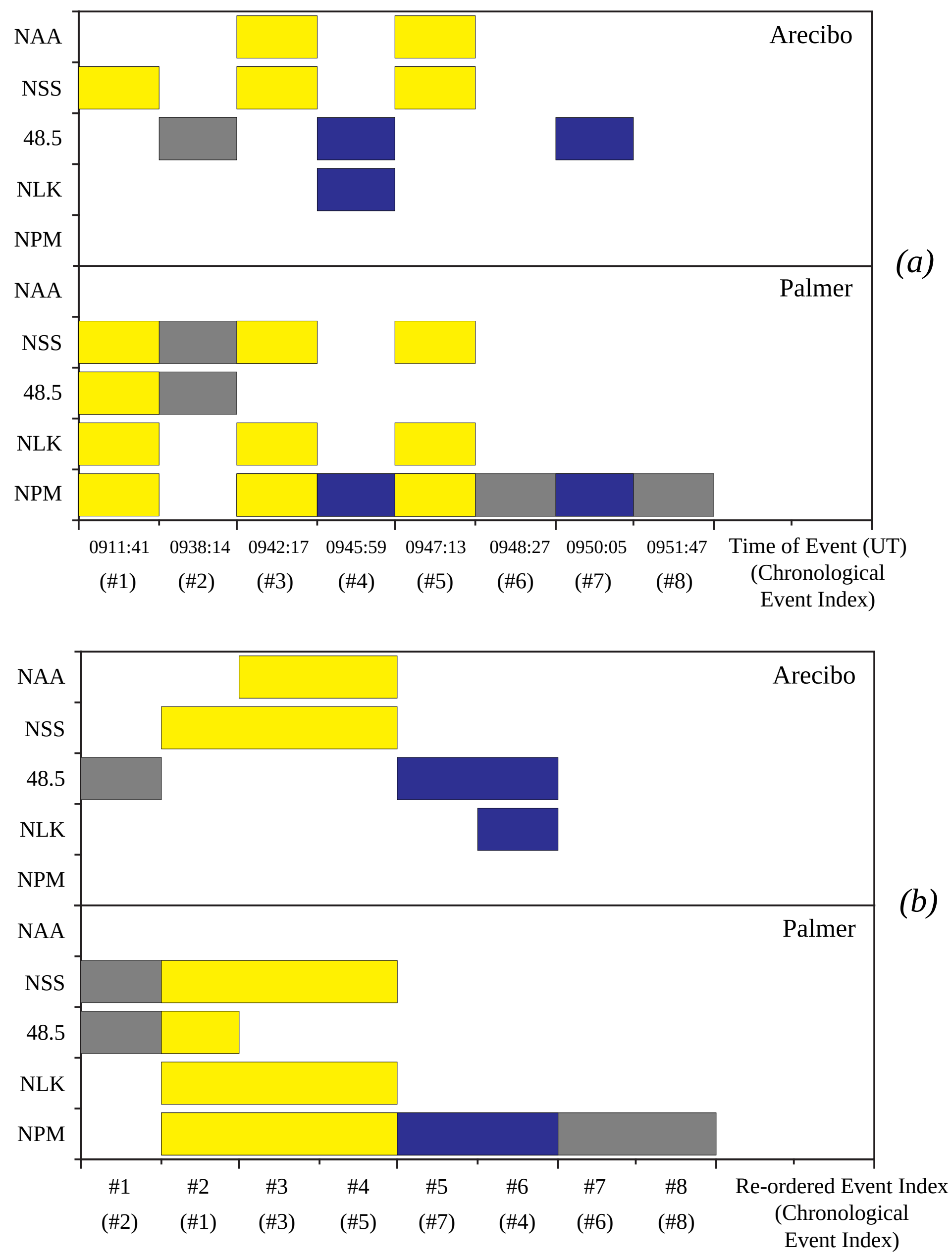

Fig. 4.3. Patterns of simultaneity among perturbations of ten signal paths. Perturbation onsets observed within 1 s of each other at the same or different sites are regarded as a single, simultaneously observed "event." To illustrate the analysis of simultaneity, (*a*) and (*b*) show eight of the 270 such events observed at Arecibo and Palmer Station between 0900 and 1000 UT on March 21, 1989. Each event is represented by a column possessing a shaded box for each signal path perturbed in that event, with light shading indicating "east group" events and dark shading indicating "west group" events, defined in the text (see also Figure 4.1); medium shading represents events in neither group. (*a*) The eight selected events are shown chronologically. (*b*) The eight events have been re-ordered in a sequence which is not chronological, but which more clearly illustrates patterns of simultaneity.

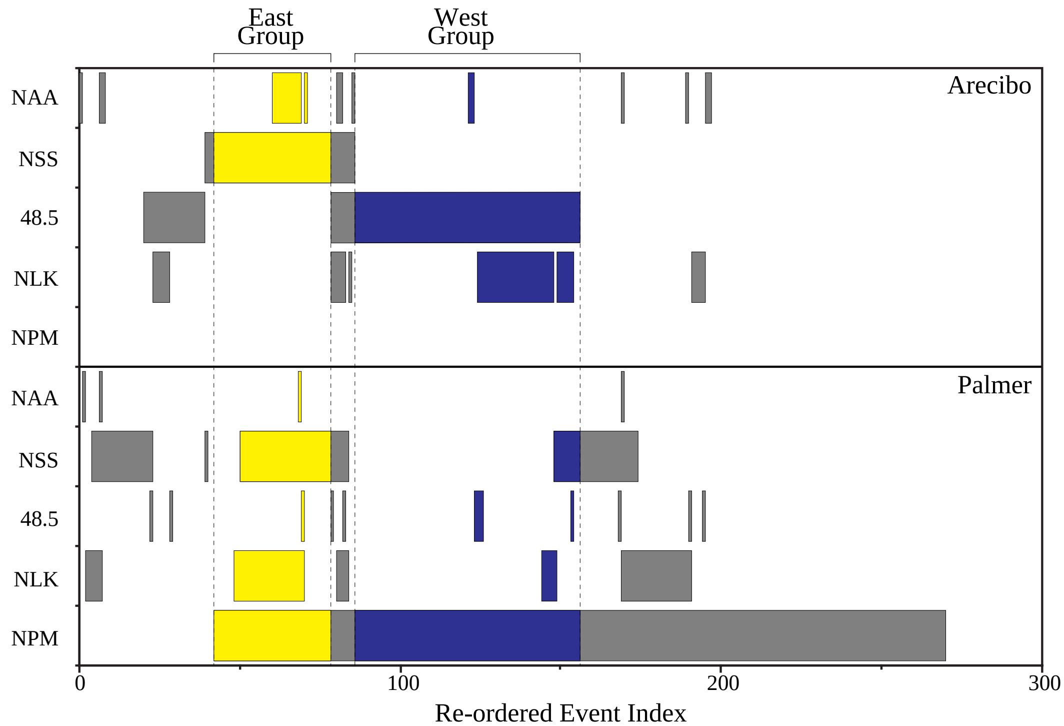

Fig. 4.4. Simultaneity of 270 signal perturbation "events" observed on subionospheric signals from five transmitters received at Arecibo and Palmer Station between 0900 and 1000 UT on March 21, 1989. The format is identical to that in Figure 4.3*b*.

That these two distinct groups of simultaneity exist suggests that at least four separate regions of ionospheric disturbance, two in each hemisphere, perturbed the monitored signal paths. To investigate this possibility, the two groups were compared.

As shown graphically in Figure 4.4, east group events accounted for 36 and west group events accounted for 70 of the 129 events observed at both sites. Eight additional events involved both NSS and 48.5 kHz at Arecibo as well as NPM at Palmer, and are not included in either group. East group and west group events were interspersed during the hour studied, but not evenly. Most east group events occurred around 0930 UT, while most west group events occurred around 0955 UT.

Sixteen well-defined events, nine from the east group and seven from the west group, were selected to represent the two categories. The following sections discuss the whistlers, onset delays, and lightning flashes associated with these sixteen events.

4.2 ASSOCIATED WHISTLERS

The onset of each of the sixteen selected events occurred simultaneously with a whistler recorded at Palmer Station, which is consistent with similar, previously reported comparisons [*Inan and Carpenter*, 1986]. The radio atmospheric associated with each of these whistlers was identified in the Palmer broadband data with an accuracy of ± 0.03 s. The time of each radio atmospheric was then corrected by 0.04 s of approximate propagation delay to Palmer Station from its conjugate point.

Figure 4.5 shows a high-resolution comparison of the perturbation onsets with spectrograms of the associated whistlers for the east group and west group events marked with arrows on Figure 4.2. The west group whistler differs in at least two ways from the east group whistler. First, the whistlers appear to have traversed slightly different L-shells; analysis of whistler traces and corrected radio atmospherics associated with each group indicates propagation at $L = 2.1$ for the west group and at $L = 2.3$ for the east group (Section 3.2.2). Second, the west group whistler is over 10 dB less intense than the east group whistler, and the portion of the west group whistler below the Earth-ionosphere waveguide cutoff at ~ 2 kHz appears to be more severely attenuated than that of the east group whistler.

Both of these differences between east group and west group whistlers were consistent among all sixteen whistlers examined. They imply the association of at least two groups of whistler ducts with the two groups of Trimpi events. The ionospheric exit regions from these two ducts appear to be in one case nearer to Palmer Station, higher in L-shell, and associated with the east group; in the other, they appear to be farther from Palmer, lower in L-shell, and associated with the west group.

Identification of the associated radio atmospheric and approximate correction for propagation delay also makes possible the determination of "onset delay," defined here as the time between the propagation-delay-corrected atmospheric and the onset of an associated signal perturbation (Section 1.2). Onset delays were measured for each perturbation involved in the sixteen events, and are compared in Figure 4.6. Large error ranges in some cases are due

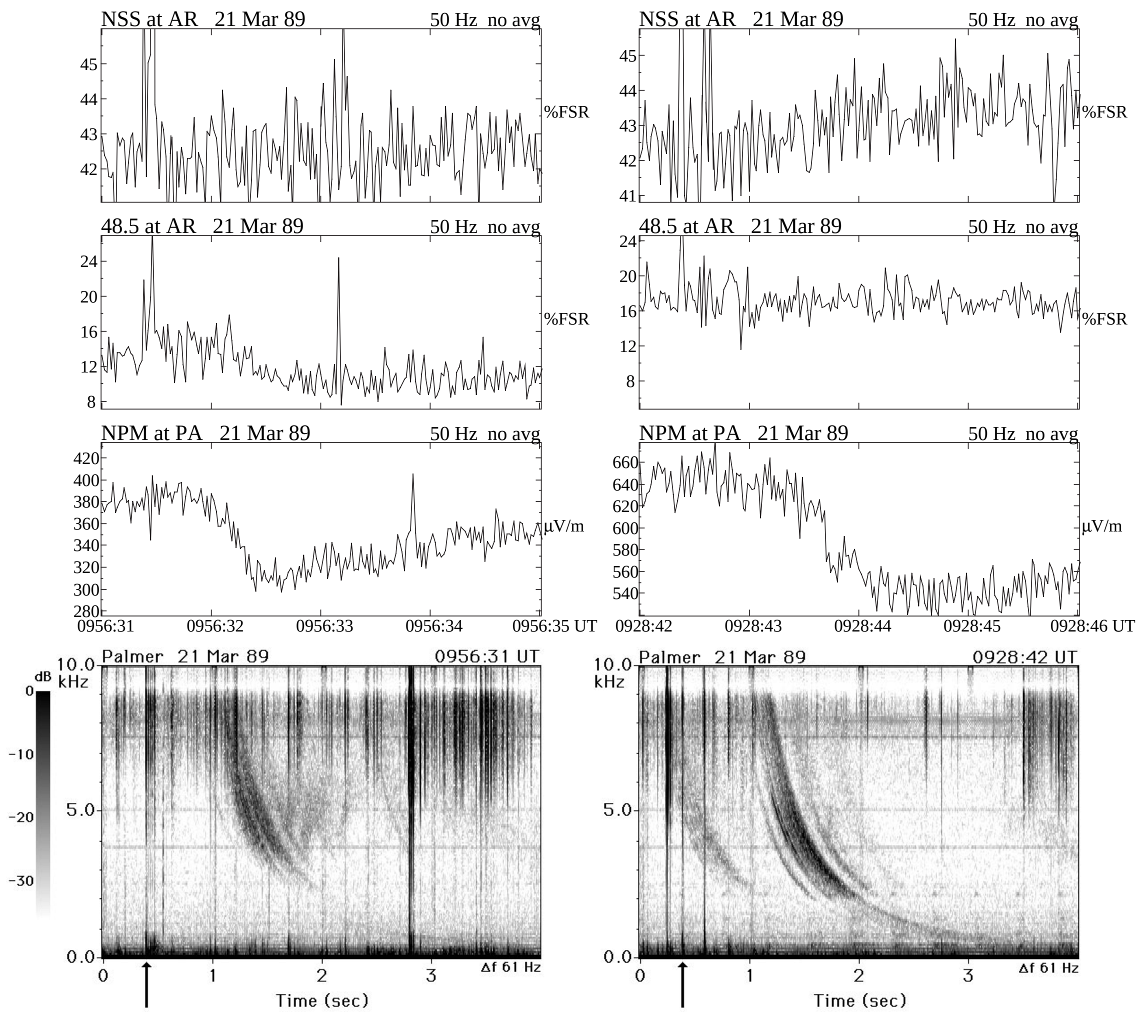

Fig. 4.5. Detailed comparison of whistlers recorded at Palmer with perturbation onsets observed at Arecibo and Palmer. The perturbations illustrated are marked with arrows on Figure 4.2. On the left is a multipath whistler typical of those associated with "west group" events, on the right a multipath whistler typical of those associated with "east group" events. The radio atmospherics associated with both are identified by arrows.

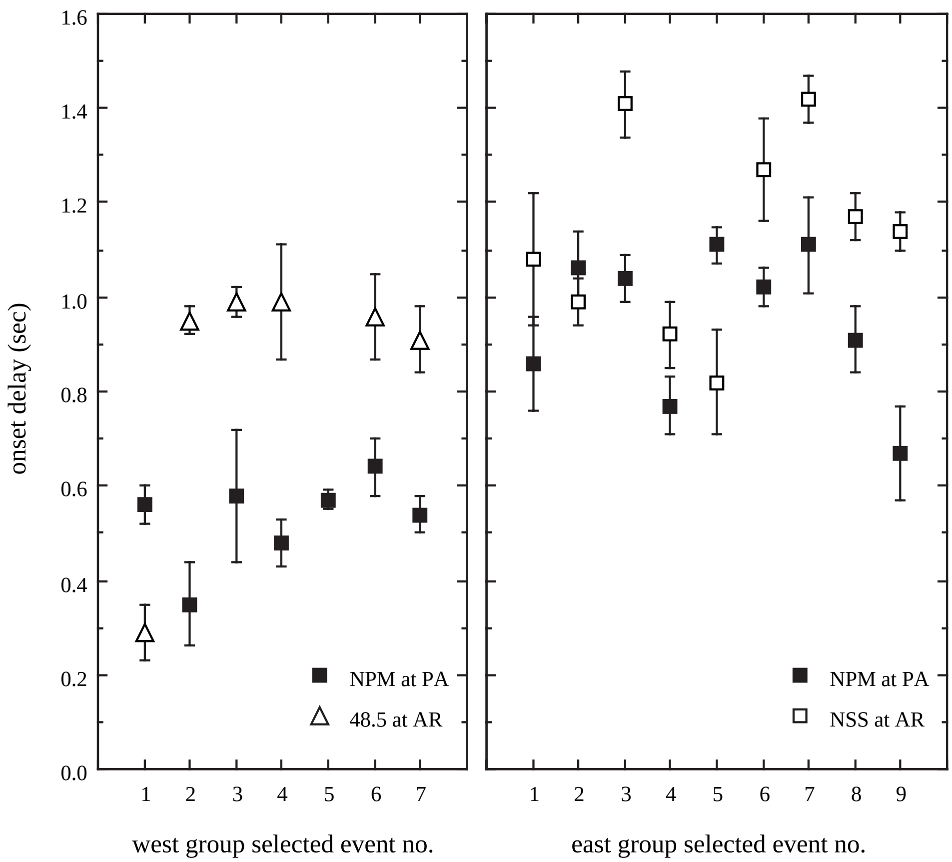

Fig. 4.6. Comparison of selected onset delays on March 21, 1989. Onset delays were measured for some of the simultaneous perturbations involved in sixteen selected events, seven from the west group and nine from the east group. The onset delay for the perturbation of 48.5 kHz in event number 5 of the west group could not be determined due to noise.

to uncertainties introduced by atmospheric and other noise. Nevertheless, it is apparent that the perturbations observed in the Southern Hemisphere frequently began 0.3 to 0.6 s before the corresponding perturbations observed in the Northern Hemisphere. It also appears that east group onset delays were in general 0.2 to 0.4 s longer than their counterparts in the west group. The greater east group delays are consistent with whistler-associated electron precipitation from a higher L-shell, where whistler propagation and electron bounce times would be longer [*Chang and Inan*, 1985]. A detailed interpretation of onset delays observed in the Northern and Southern Hemispheres in terms of whistler-induced electron precipitation theory is given in Section 5.4.

4.3 THUNDERSTORM ACTIVITY AND ASSOCIATED LIGHTNING

Lightning time and location data from the State University of New York (SUNY) lightning detection network [*Orville et al.*, 1983], provided courtesy of Dr. R. Orville, were examined first to locate the North American regions affected by thunderstorms during the period in question, and subsequently to determine whether particular cloud-to-ground lightning flashes responsible for the sixteen analyzed whistlers could be identified in the SUNY data.

Figure 4.1 maps the locations and conjugates of all flashes detected by the network between 0940 and 0950 UT as a general indication of thunderstorm activity. Also mapped are ten flashes whose first strokes occurred within 0.03 s of the times, corrected for propagation delay, of radio atmospherics associated with the sixteen representative whistlers (the six atmospherics for which no corresponding flashes were recorded may have been radiated by cloud-to-cloud flashes, which are neglected by the detection network, or by cloud-to-ground flashes which were missed by the network [*Inan et al.*, 1988*b*; *Carpenter and Orville*, 1989]). Of the ten associated flashes, five correspond to the east group and five to the west group, and are labeled 'E' and 'W', respectively. Six of the ten flashes were separated in time by more than one second from other flashes recorded by the network, further decreasing the likelihood that the close time correspondence between the time-corrected radio atmospherics and the SUNY flashes is coincidental.

Of the ten flashes time-associated with the representative whistlers, the five associated with the east group all occurred in East Coast thunderstorms, and the five associated with the west group all occurred in Gulf Coast thunderstorms. The consistency with which these flash locations correspond to the two groups of events studied suggests a correlation between the location of a flash and the location of an associated ionospheric disturbance, and supports the distinction between west and east group events; the significance of the correspondence in this particular case is not clear, however, since in another study *Yip et al.* [1991] examined recent data involving the midwestern United States and found no such correlation.

4.4 DISCUSSION

As mentioned in the beginning of this chapter, the possibility of conjugate precipitation associated with individual lightning flashes has been implied by recent analyses of satellite data. *Inan et al.* [1985*b*] showed that radiation belt electrons scattered by waves into the bounce loss cone do not necessarily precipitate in the first encounter with the atmosphere, but can backscatter and remain trapped for one or more hops before precipitating. Atmospheric backscatter can reflect up to 90% of electrons that would otherwise precipitate, as a result of the grazing angles at which wave-scattered electrons reach the atmosphere [*Berger et al.*, 1974]. Evidence presented by *Voss et al.* [1984] supported this hypothesis, showing that the lifetime of bursts of electrons scattered into or near the bounce loss cone by whistlers may be as long as four bounce periods. Such bursts would have the opportunity to disturb the ionosphere in both Northern and Southern Hemispheres.

The measured onset delays show a tendency for the Southern Hemisphere to be disturbed before the Northern Hemisphere in simultaneously observed events. At first thought, this result is contrary to what would be expected from a southbound whistler wave inducing "direct" precipitation into the north, followed by "mirrored" precipitation into the south [*Chang and Inan*, 1985].

A difference in northern and southern electron loss cone angles could explain this behavior. At longitudes near Palmer Station, the Southern Hemisphere loss cone is wider than the Northern Hemisphere loss cone as a result of the South Atlantic Magnetic Anomaly (Figure 2.4). As a result, typical trapped electron flux at the edge of the southern loss cone can be 10 to 100 times larger than that at the edge of the northern loss cone [*Inan et al.*, 1988*c*], and the first significant precipitation induced by Northern Hemisphere lightning may well strike the Southern Hemisphere after mirroring in the north. Later disturbance of the Northern Hemisphere could then result from precipitation of electrons which backscattered from the atmosphere in the south. Such twice-reflected precipitation is also consistent with our finding that the disturbances observed in the north were more likely to have counterparts in the south than vice-versa. The effect of the Anomaly on precipitation is further discussed in Section 5.4 and illustrated in Figure 5.16.

At least two groups of events were identified during the period investigated. These two groups differ in the combinations of signal paths which were perturbed, the perturbation onset delays, the characteristics of the associated whistlers, and the location of the associated lightning, implying that at least four separate ionospheric regions were disturbed, two in each hemisphere. This result suggests that analysis of patterns of simultaneous perturbations observed in conjugate regions may shed additional light on the size, shape, and location of ionospheric disturbances in either hemisphere.

In the Southern Hemisphere, both disturbed regions appear to have been near the NPM to Palmer great circle path. The relatively high rate of perturbations occurring on NPM at Palmer on this day as well as on others could therefore be a result of multiple and distinct regions of ionospheric disturbance in the Southern Hemisphere. *Wolf* [1990] showed that the NPM signal appears to be more commonly perturbed than any other monitored at Palmer. In light of the results presented here, it is perhaps no coincidence that this signal path lies conjugate along much of its length to the southeastern United States, a region known for frequent and widespread thunderstorm activity.

The events of March 21, 1989 followed one week after one of the biggest geomagnetic storms since quantitative records began in 1868 [*Allen et al.*, 1989]. This storm may have influenced the location, size, and occurrence rate of the ionospheric disturbances which were observed; still, similar conjugate disturbances were measured on April 8, three weeks after the storm peaked, and have since been found to occur regularly (Chapter 5).

The disturbance of ionospheric regions in both hemispheres in association with individual lightning flashes suggests a broader role for lightning-induced electron precipitation (LEP) events in the coupling of lower and upper atmospheres: thunderstorms in one hemisphere can disturb the ionosphere in both hemispheres. Observation of conjugate ionospheric regions can increase the amount of ground-based information available on individual LEP events, as we shall see in the next chapter.

5

Subionospheric Signal Perturbation and Whistler Associations

The existence of a temporal association between ducted whistlers and the characteristic perturbation of subionospheric VLF, LF and MF signals recorded at Palmer Station, Antarctica is well documented (e.g., *Inan and Carpenter* [1986]). Whistler and signal perturbation data from a number of single-hemisphere experiments have been quantitatively interpreted as evidence of ducted-whistler-induced pitch angle scattering of radiation belt electrons, whose subsequent precipitation disturbs the lower ionosphere [*Lohrey and Kaiser*, 1979; *Carpenter et al.*, 1984; *Inan et al.*, 1985*a*; *Inan and Carpenter*, 1987].

Despite these results, the "smoking gun" directly linking ducted whistlers with precipitation and ionospheric disturbances has eluded us. In an effort to clarify the significance of ducted whistlers in the precipitation of electrons, this chapter presents the first detailed temporal, spatial, and theoretical comparison of conjugate signal perturbations with associated ducted whistlers.

5.1 WEAK WHISTLERS AND NORTHERN HEMISPHERE SIGNAL PERTURBATIONS

Past studies of the association between signal perturbations and ducted whistlers have relied solely on observations conducted at Palmer Station. We now find that, even when Palmer observes no signal perturbations, Palmer whistlers can be associated with perturbations detected in the Northern Hemisphere. Figure 5.1 shows a ten-minute period of Northern Hemisphere signal perturbations occurring between 0650 and 0700 UT on 26 April 1990. During this period narrowband data were available from AR, HU, and PA. Except for 48.5–AR, 48.5–HU, NLK–AR, NLK–HU, and NPM–HU, which were perturbed simultaneously, no other signal path observed was clearly perturbed, including NAU–HU. This configuration is consistent with an ionospheric disturbance located 100–200 km northwest of HU, as suggested in Figure 5.1*b*. Of the fourteen 0.1 dB or greater signal perturbations measured on 48.5–HU, all were associated with one-hop whistlers recorded at Palmer.

As narrowband causative sferics existed in some of the Northern Hemisphere signal data, most clearly on NAA–HU, associated whistlers were identified by comparing the time of narrowband and whistler causative sferics as described in Section 3.3. Narrowband causative sferics were identifiable for twelve of the fourteen perturbations of 48.5–HU. Assuming the lightning occurred over the continental United States, a reasonable assumption given the strength of the narrowband sferics at HU, the sferic propagation delay to Palmer would be 39 ± 5 ms. Allowing for this delay, all twelve narrowband sferics corresponded to whistler causative sferics: in five cases the sferics matched within 20 ms (the resolution limit of the narrowband sampled data), and even in the worst two cases the match was within 140 ms. The lack of a better match in the latter cases may represent misidentification of the causative sferics because of their tendency on this day to occur in clusters. Nevertheless, assuming that the occurrence interval between the 250 whistlers measured above $\sim$2 μV/m in this ten minute period followed a Poisson distribution [*Inan and Carpenter*, 1986], the probability of chance association of the twelve narrowband causative sferics within even 140 ms of whistler causative sferics would be less than 10^{-15}. As shown in Figure 5.2, the magnitude

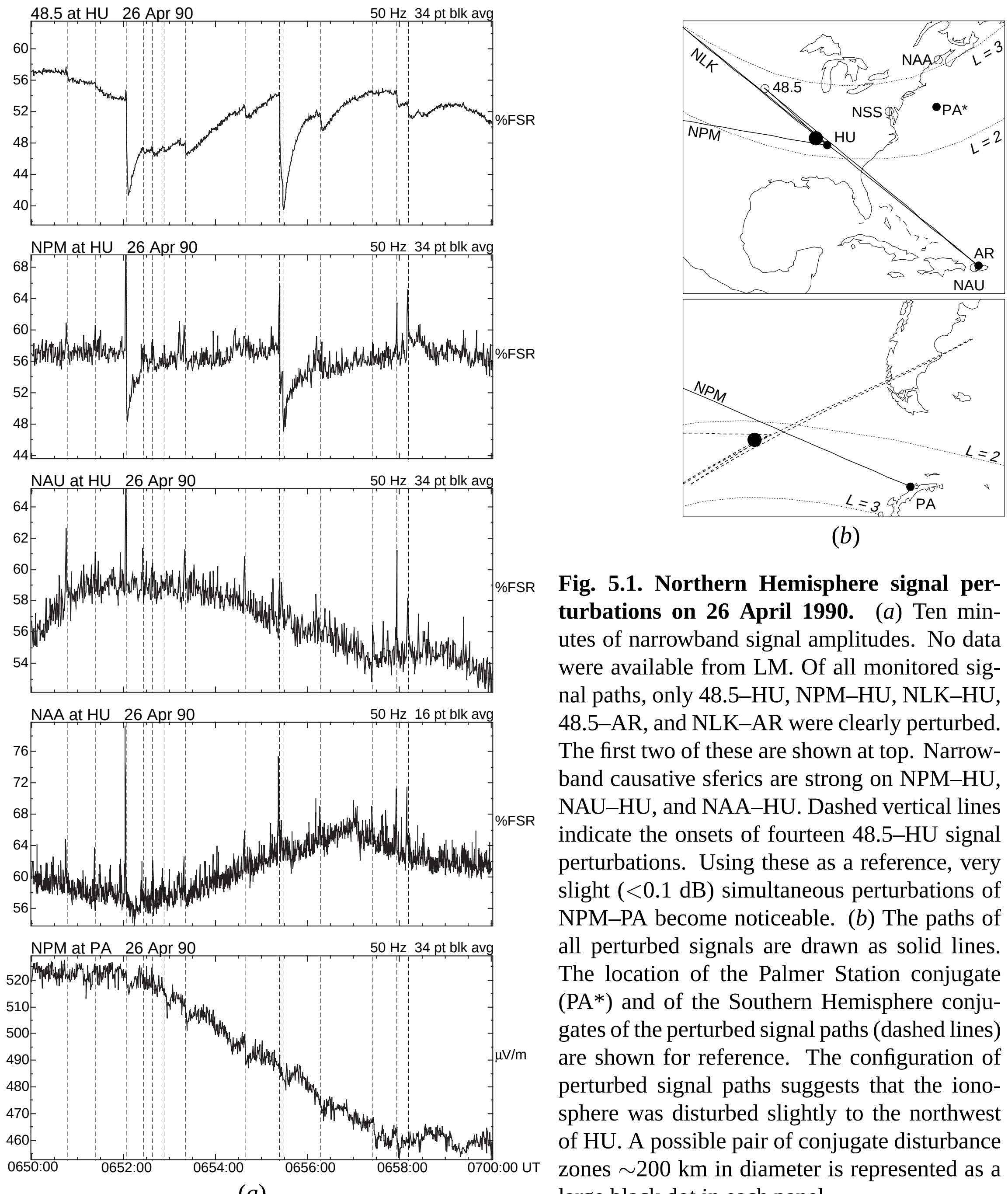

Fig. 5.1. Northern Hemisphere signal perturbations on 26 April 1990. (*a*) Ten minutes of narrowband signal amplitudes. No data were available from LM. Of all monitored signal paths, only 48.5–HU, NPM–HU, NLK–HU, 48.5–AR, and NLK–AR were clearly perturbed. The first two of these are shown at top. Narrowband causative sferics are strong on NPM–HU, NAU–HU, and NAA–HU. Dashed vertical lines indicate the onsets of fourteen 48.5–HU signal perturbations. Using these as a reference, very slight (<0.1 dB) simultaneous perturbations of NPM–PA become noticeable. (*b*) The paths of all perturbed signals are drawn as solid lines. The location of the Palmer Station conjugate (PA*) and of the Southern Hemisphere conjugates of the perturbed signal paths (dashed lines) are shown for reference. The configuration of perturbed signal paths suggests that the ionosphere was disturbed slightly to the northwest of HU. A possible pair of conjugate disturbance zones ∼200 km in diameter is represented as a large black dot in each panel.

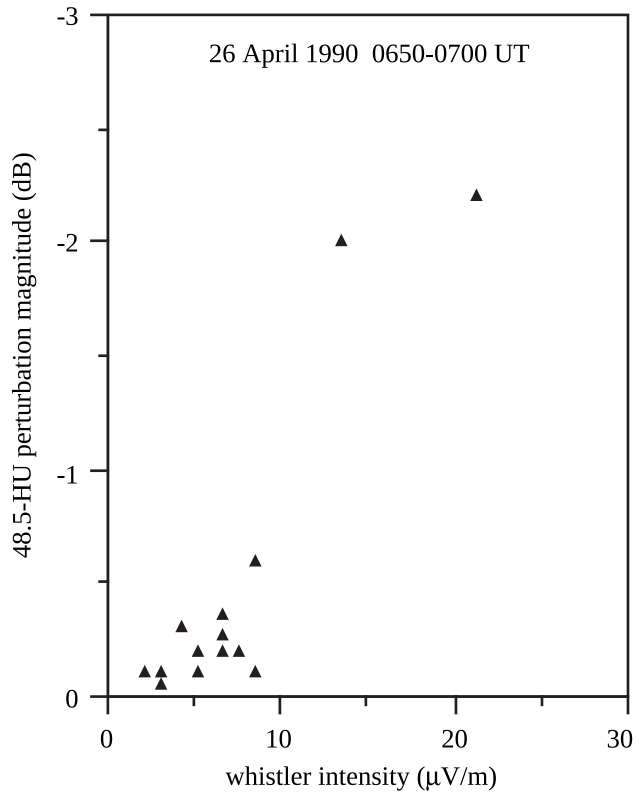

Fig. 5.2. The intensities of the whistlers observed at Palmer on 26 April 1990 compared with the magnitudes of associated perturbations of the 48.5–HU signal. Fourteen perturbations were recorded between 0650 and 0700 UT. A positive correlation is consistent with the scattering and precipitation of electrons by the observed whistlers during ducted propagation. Perturbation magnitude measurements have an error of ± 0.1 dB, and whistler intensity measurements an error of $\pm 25\%$. Whistler intensities are given in μV/m instead of dB for consistency with the literature [*Carpenter and LaBelle*, 1982; *Inan and Carpenter*, 1986].

of the fourteen Northern Hemisphere signal perturbations correlated with the intensity of associated whistlers, a characteristic of Southern Hemisphere perturbation-whistler associations reported by *Carpenter and LaBelle* [1982] and *Inan and Carpenter* [1986].

The whistlers in this case include the weakest yet documented in association with signal perturbations. The fourteen associated whistlers measured between 2 and 21 μV/m, ranging below the association thresholds of 13 μV/m [*Carpenter and LaBelle*, 1982] and 50 μV/m [*Inan and Carpenter*, 1986] discussed in two previous case studies. At the same time, 42 of the total 250 whistlers observed were stronger than 50 μV/m but were not associated with detected signal perturbations in either hemisphere. The dispersion and multipath characteristics of these unassociated whistlers differed from those of the associated whistlers. Arrival azimuths could not be obtained for associated whistlers due to their weak intensities, but the unassociated whistlers appeared to arrive from azimuths of 210° to 240°, well south of the region conjugate to the 48.5–HU path. Attempts to determine precise *L*-shell and N_{eq} of both associated and unassociated whistlers were inconclusive for lack of sufficient dispersion, due apparently to fast propagation outside the plasmapause and at low *L*-shell ($2 \lesssim L \lesssim 2.5$). This interpretation is consistent with the strong geomagnetic activity (K_p = 5+) observed during this period (D. L. Carpenter, private communication, 1992), as well as with the relatively short onset delays of 0.2 to 0.8 s which characterized the Northern Hemisphere signal perturbations (cf. Figure 4.6; see also *Chang and Inan* [1985]).

The association of extremely weak whistlers with signal perturbations in this case could be due to precipitation by ducted whistlers which entered the Earth-ionosphere waveguide at a relatively large distance from Palmer. The southern conjugate of the inferred precipitation region, where we assume precipitation-inducing ducted whistlers would exit the magnetosphere (Section 3.2.2), lies some 2300 km from Palmer (Figure 5.1*b*). Using an estimate for subionospheric VLF attenuation discussed later in Chapter 6, propagation to Palmer over this distance would have attenuated the whistlers by $\sim$36 dB.

Upon closer examination, very slight NPM–PA perturbations ($<$0.1 dB) can be seen in Figure 5.1 which coincided with many of the events on 48.5–HU. These perturbations may have resulted from nearly simultaneous ionospheric disturbances conjugate to those inferred in the north. Such disturbances would have been located some 200–250 km off the NPM–PA path, as suggested in Figure 5.1*b*. If this was the case, the extremely small NPM–PA perturbations compare well with the theoretical analysis by *Poulsen et al.* [1990] of diminishing perturbation magnitudes with increasing path-disturbance separation (Figure 1.7). By the same token, the frequent occurrence of NPM–PA perturbation magnitudes ranging from 0.1 to 1 dB and above on other days [*Wolf and Inan*, 1990] might be due to disturbances closer to the NPM–PA path.

The above results suggest that very weak observed whistler intensities are not in themselves adequate to discount the possibility of associated precipitation in either hemisphere. Whistlers at the lower limits of reception, which would include weak components of multipath whistlers, can indicate the precipitation of radiation belt electrons at locations relatively distant from the receiver.

5.2 PERTURBATION SIGNATURES AND WHISTLER MULTIPATH CHARACTERISTICS

If every ducted whistler induces a precipitation burst, we would expect multipath whistlers to induce multiple precipitation bursts, causing multiple ionospheric disturbances. The disturbance of multiple regions was an interpretation offered by *Carpenter et al.* [1984] to explain the simultaneous perturbation of signals arriving at Palmer from widely separated azimuths. Since then, however, the possibility of multiple, simultaneous whistler-associated disturbances has not been addressed in detail.

New support for a "shotgun" model of whistler-induced precipitation, where energy from a single lightning flash scatters and precipitates electrons in multiple, distributed whistler ducts, arises from an analysis of unusual signal perturbation signatures observed on 16 April 1990. Figure 5.3 shows eight of the nine signal paths affected during an eleven minute period of simultaneous perturbations observed on this day at AR, LM, and PA. Data from HU were unavailable. Each of the thirteen events marked *a* through *m* on NPM–PA was associated with a multipath whistler recorded at Palmer. The marked perturbation signatures fall into three categories:

- upgoing with anomalously long onset duration ($\sim$10 s), displayed by events *a* and *i*;
- momentarily downgoing but then upgoing (similar to the "overshoot" effect discussed by *Dingle and Carpenter* [1981]), displayed by events *b, c, e, g,* and *k*;
- downgoing with fast ($\sim$10 s) recovery, displayed by events *d, f, h, j, l,* and *m*.

We compare the onsets of representative events *a*, *k*, and *f* with spectrograms of their associated whistlers in Figure 5.4. These and all multipath whistlers detected during the

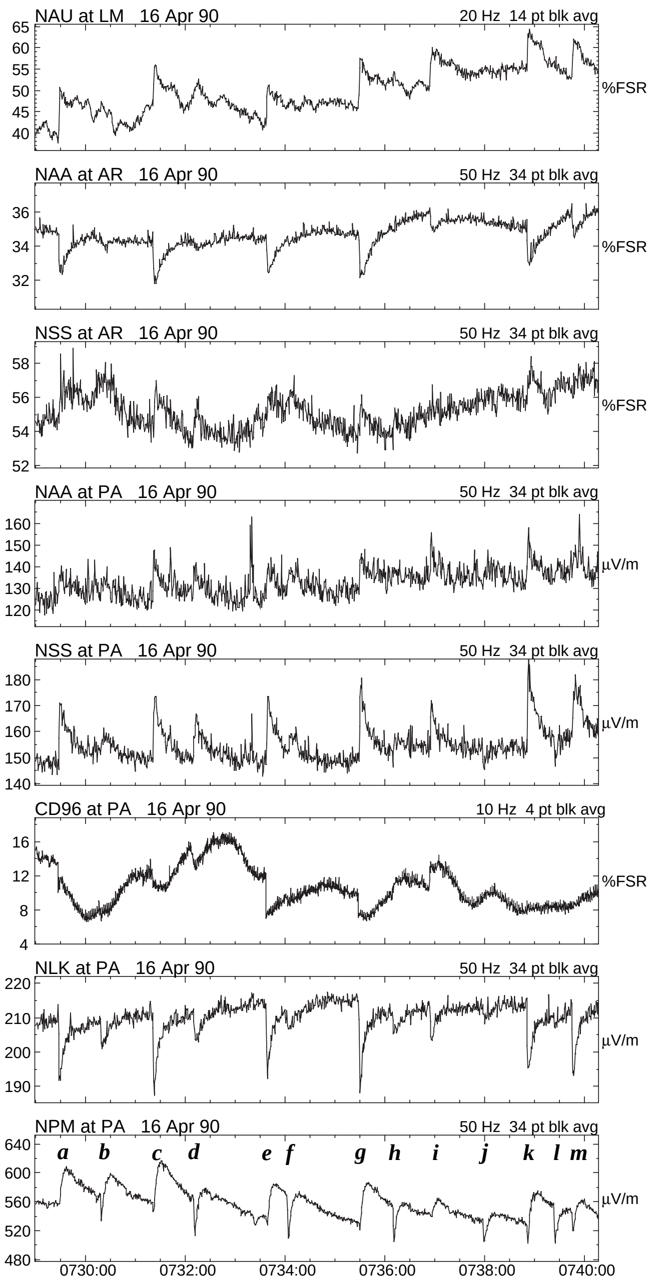

(*a*)

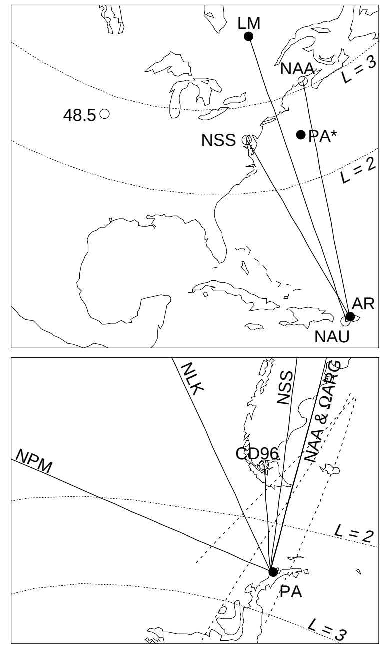

(*b*)

Fig. 5.3. Slow-onset and "overshoot" signal perturbations on 16 April 1990. (*a*) An eleven-minute period of simultaneous signal perturbations on eight signal paths (Omega Argentina at PA was also perturbed but is not shown). The thirteen events detected on NPM–PA during the period are marked *a* through *m* for identification. The unusually slow onset behavior and occasional initial downward excursions ("overshoots") of the upgoing events on NPM–PA are interpreted in the text as resulting from multiple ionospheric disturbances near the NPM–PA signal. (*b*) The format of the map is identical to that in Figure 5.1*b*. HU is not shown because no data were available from that site.

period included the same components, schematically identified in Figure 5.5. Although the relative intensity of the components differed from whistler to whistler, the dispersion characteristics remained the same. The observed variations in relative component intensity from one whistler to the next could reflect changes in the relative coupling efficiency of the causative sferic into the various whistler ducts. Such changes may in turn depend on the location and orientation of the source lightning discharge, since those characteristics would affect the sferic propagation and mode structure in the duct coupling regions.

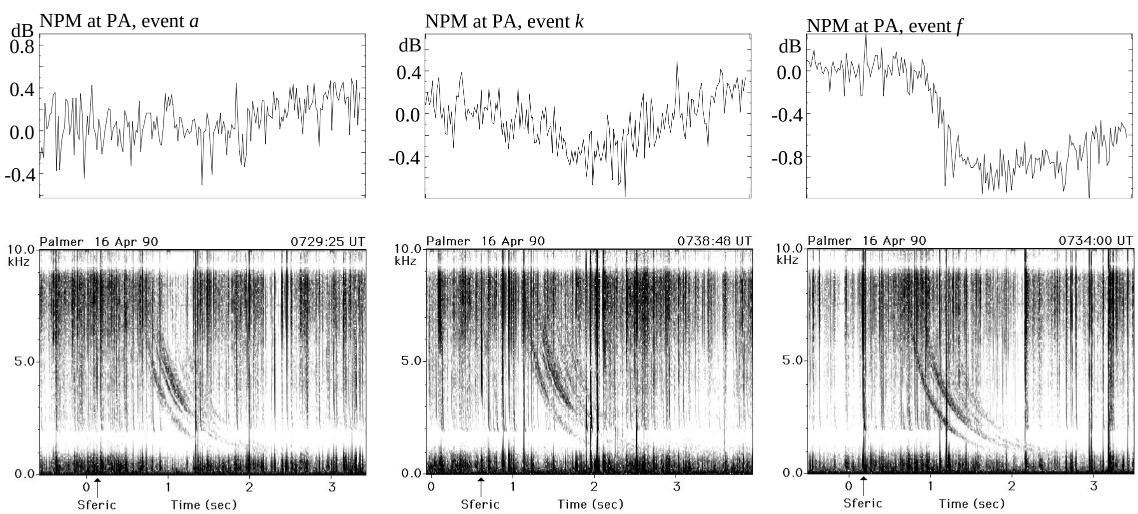

Fig. 5.4. Examples of the time association between whistlers and NPM–PA signal perturbations for three of the thirteen events marked in Figure 5.3. The examples represent the three characteristic perturbation signatures observed: slow-onset upgoing (event *a*), overshoot upgoing (event *k*) and normal downgoing (event *f*). Analysis of these and the other events in Figure 5.3*a* indicates a link between perturbation signature and the relative strength of associated whistler components. The 0 dB reference corresponds to the ambient pre-perturbation signal level in each case. The spectrograms display a 30 dB dynamic range, with maximum intensity (black) representing signals $\geq 95\mu$V/m, and with a frequency resolution (Δf) of 61 Hz.

The apparent dependence of perturbation signature on the relative component intensities of associated multipath whistlers, suggested by Figure 5.4, may be due to the scattering by those whistlers of multiple, separately located precipitation bursts. Such bursts would

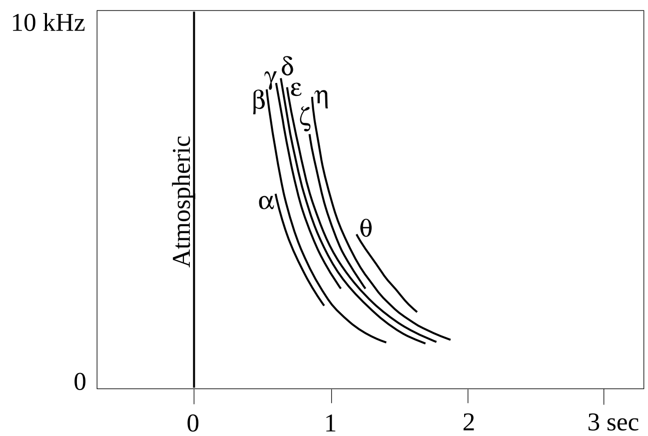

Fig. 5.5. A schematic identification of whistler components in Figure 5.4. The intensity of the γ component in particular appears to correspond to the upgoing magnitude of the associated NPM–PA signal perturbations shown in Figure 5.4.

result in multiple ionospheric disturbances, two of which might perturb the amplitude of a subionospheric signal with opposite polarity. The peculiar slow-onset and "overshoot" signatures of 16 April 1990 could thus result from the superposition of two competing signal perturbations caused by simultaneous but spatially separate ionospheric disturbances, while the downgoing signatures, with more typical onset behavior, result from a single ionospheric disturbance.

We test this hypothesis by closely comparing the upgoing and downgoing signatures. If the slow-onset upgoing signature represents competing "up" and "down" signal perturbations, and the downgoing signature represents only the "down" perturbation component, we can reconstruct an approximate "up" perturbation component by subtraction. As shown in Figure 5.6, the subtraction of event *f* from event *a* suggests an "up" perturbation component for event *a* which compares well with more characteristic signatures such as those observed on NSS–PA.

By the same token, the "overshoot" signatures could be decomposed into "up" and "down" perturbation components of unequal magnitudes, with the "down" component stronger at first but soon overwhelmed by the longer recovery time of the "up" component. In the

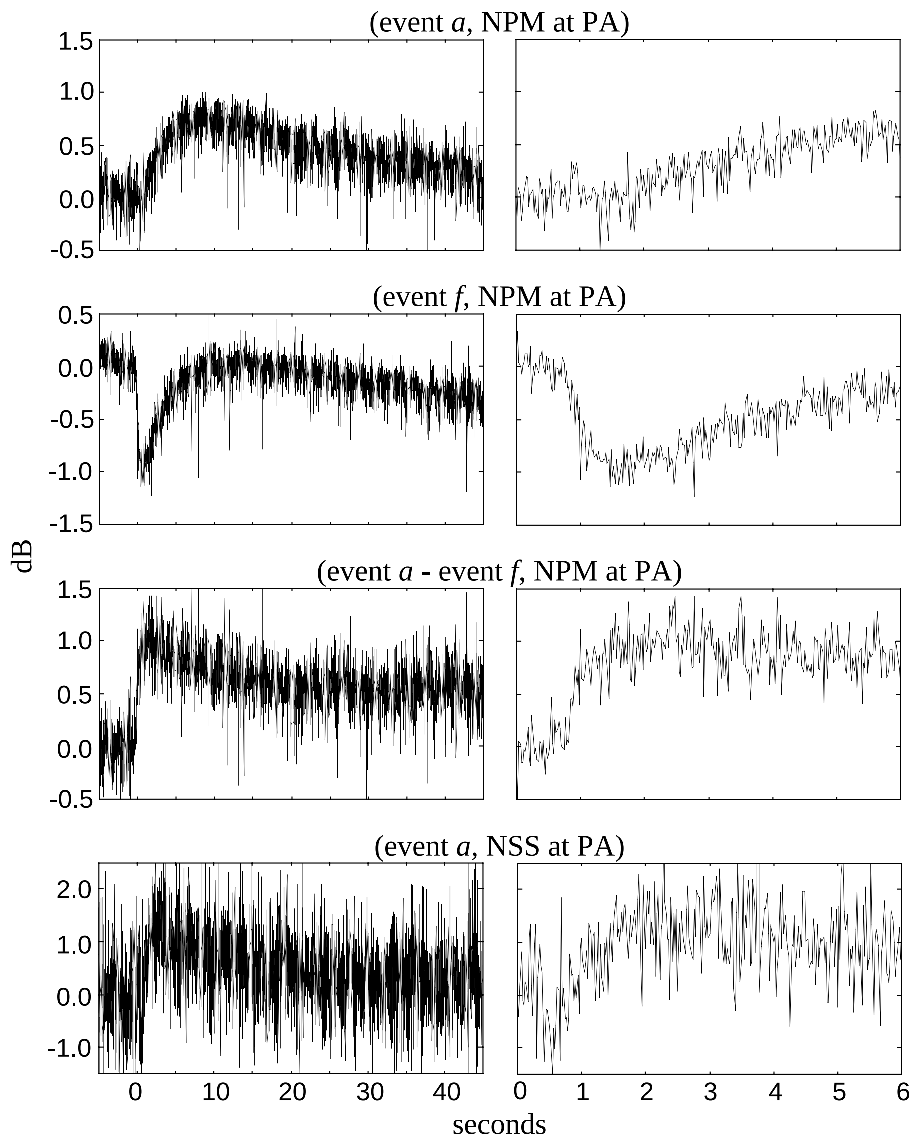

Fig. 5.6. Reconstructing an approximate "up" perturbation component. The slow-onset upgoing signal perturbation signatures shown in Figure 5.3 appear to have resulted from the superposition of a slow-recovery upgoing perturbation and a fast-recovery downgoing perturbation. To investigate this possibility, we estimate an upgoing "component" perturbation for event *a* by subtracting event *f*, a typical downgoing event, from event *a*. The result suggests an upgoing component which compares well with more normal onset behavior, such as that exhibited by NSS–PA. In all panels t = 0 corresponds to the time of the causative sferic. The 0 dB reference corresponds to the ambient pre-perturbation signal level in each case.

general case one would expect to see a continuum of signatures, ranging from upgoing to overshoot to downgoing, depending on the relative strength of the "up" and "down" perturbation components. If a duct-disturbance association holds, the relative strength of the perturbation components would in turn depend on the relative strength of the associated whistler components.

To evaluate the dependence of signal perturbation signature on relative whistler component strengths, we must first identify the associated whistler components. This task is complicated by the presence of at least eight clear components in each multipath whistler (Figure 5.5) which are partly obscured by several additional and less distinct components. A study of the timing, arrival azimuth, and intensity of the identified whistler components leads us to associate the γ whistler component with the "up" perturbation component, and, with less certainty, the ϵ whistler component with the "down" perturbation component. While the intensity of the γ whistler component corresponds well to the observed magnitude of the upgoing signal perturbations, we associate the ϵ component with the downgoing perturbations only on the basis of timing and uncertain evidence that its arrival azimuth at Palmer matches that of the NPM signal within $\pm 30°$.

Figure 5.7 shows a progression of the thirteen perturbation signatures ordered by the relative magnitude of the γ and ϵ whistler components. Despite the uncertainty in the identification of the associated whistler components, the signatures show a distinct trend from upgoing to overshoot to downgoing (the ordering was also performed using the magnitudes of the β and δ components in place of the ϵ component, but in both those cases the progression was marginally less clear than when using the ϵ component). This result is consistent with a one-to-one relationship between multiple ionospheric disturbances and the components of multipath ducted whistlers.

The multiple disturbance hypothesis is also supported by the multiplicity of signal paths, nine in all, perturbed simultaneously in both hemispheres. If we assume that individual disturbances are centered within 200 km of perturbed signal paths [*Inan et al.*, 1990; *Poulsen*

Associated whistler component magnitudes	Ratio of γ to ε (dB)	NPM-PA amplitude signature (dB)
γ: 53 μV/m ε: 22 μV/m	8	(a)
γ: 42 μV/m ε: 47 μV/m	−1	(c)
γ: 42 μV/m ε: 48 μV/m	−1	(e)
γ: 42 μV/m ε: 53 μV/m	−2	(k)
γ: 30 μV/m ε: 38 μV/m	−2	(i)
γ: 27 μV/m ε: 34 μV/m	−2	(m)
γ: 17 μV/m ε: 42 μV/m	−8	(f)
γ: 13 μV/m ε: 34 μV/m	−8	(j)
γ: 34 μV/m ε: 95 μV/m	−9	(g)
γ: 15 μV/m ε: 67 μV/m	−13	(h)
γ: 13 μV/m ε: 60 μV/m	−13	(d)
γ: 13 μV/m ε: 67 μV/m	−14	(b)
γ: 12 μV/m ε: 60 μV/m	−14	(l)

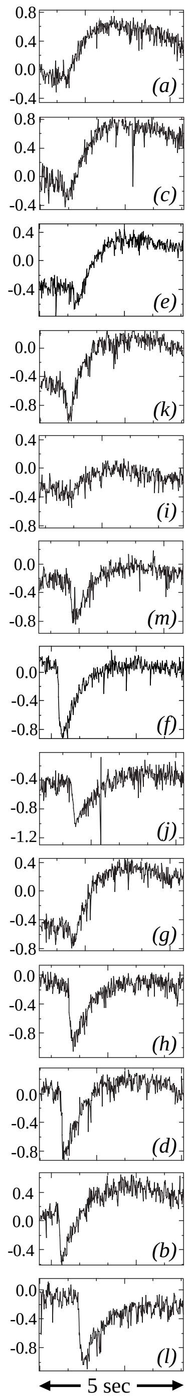

Fig. 5.7. The NPM–PA signatures identified in Figure 5.3 are ordered by the relative magnitude of the γ and ϵ components of the associated whistlers. The signature progression, from upgoing to overshoot to downgoing, is consistent with a cause-effect association between the intensity of individual ducted whistler components and the magnitude of individual ionospheric disturbances. The aberrant placement of signature *g*, whose associated whistler possessed an unusually intense ϵ component, suggests that the relationship between component intensity and disturbance magnitude is not linear for strong events, possibly indicating a "saturation" effect for LEP-induced ionospheric disturbances. Whistler component magnitude measurements have an error of $\pm$25%. In all cases 0 dB represents 560 μV/m narrowband signal strength of NPM–PA.

et al., 1990] and are located at $1.8 \leq L \leq 2.2$ (the range corresponding to the strongest whistler components observed), at least three disturbances in the south and two in the north are necessary to explain the perturbed signal path configuration (Figure 5.3*b*). If instead the signal perturbations were all caused by a single, centrally located ionospheric disturbance and its conjugate, such a disturbance would have had to perturb signals whose paths lay 600 km from its center. While such effects have been proposed by *Dowden and Adams* [1990] as a result of deeply penetrating, almost discontinuous disturbances ("stalactites"), the onset and recovery behavior in this case appears to be more consistent with multiple smaller disturbances.* Also, given the link between individual disturbances and whistler components just discussed, the presence of several conjugate disturbance pairs would be consistent with the large number of whistler components observed.

The inferred "up" and "down" perturbation components exhibit markedly different recovery times of $\sim$100 s and $\sim$10 s, respectively; of course, without some disparity in recovery, the signatures would either appear normal or be invisible altogether. The fast-recovering "down" signatures appear to be associated with whistler component ϵ, which propagated at $L \simeq 2.2$, while the slow-recovering "up" signatures appear to be associated with component γ, propagating at $L \simeq 1.9$. The disparity in recovery times at the different *L*-shells is in the opposite sense to predictions for the variation of recovery rate with *L* based on the energy spectrum and depth of ionospheric penetration of whistler-induced precipitation bursts [*Inan et al.*, 1988*a*]; however, those predictions assumed a constant and uniform whistler spectral density. The ϵ component is stronger than the γ component below 1.5 kHz, a frequency which corresponds at these *L* values to equatorial resonant loss-cone electron energies of about 500 keV; therefore, the ϵ component may be associated with more precipitation of $>$500 keV electrons than the γ component. The faster recovery signatures associated with

---

* It is interesting to note that Figure 1 of *Dowden and Adams* [1990] shows signal amplitude perturbations which apparently exhibit "overshoot" signatures, implying that their data may have been influenced by multiple precipitation zones. Their paper recognized the possibility of multiple disturbances, but attributed this possibility to evidence of signal amplitude changes too large to be explained by scattering off a single "stalactite" disturbance.

the ϵ component may thus be related to the faster effective recombination rates expected at the mesospheric altitudes ionized by such high-energy particles [*Inan et al.*, 1988*a*]. Additional factors, such as the duct shape or anomalies in radiation belt electron populations, may also play a role in precipitation burst energy spectra and resulting recovery signatures.

During the eleven minute period shown in Figure 5.3*a*, a total of twenty multipath whistlers were observed whose strongest components exceeded a threshold of $\sim$2 μV/m; however, even though all twenty whistlers exhibited similar multipath and dispersion characteristics, only thirteen were associated with signal perturbations. The seven unassociated whistlers were consistently weak – none exceeded 19 μV/m, 6 dB weaker than the weakest of the associated whistlers (event *i*) – but even so, they were stronger than those of the 26 April 1990 case discussed earlier for which associated signal perturbations were observed. The lack of signal perturbations for the weaker whistlers on 16 April may indicate that the precipitation regions were located far enough from the monitored signal paths that only the stronger whistlers could induce enough precipitation to detectably perturb a signal. This interpretation is consistent with the presence of upgoing perturbations on a majority of the nine perturbed signals, since upgoing perturbations of a signal were attributed by *Poulsen et al.* [1990] to disturbances located 100–200 km off the signal path (Figure 1.7). Some of the observed perturbations may also have been associated with whistler components other than the strongest; the intensities of these weaker components would more closely compare with those of the weak whistlers observed on 26 April. Finally, the 16 April whistlers could have exited their ducts closer to Palmer than those on 26 April, which would be consistent with the higher range of whistler intensities observed.

We have interpreted the "overshoot" effect as a result of multiple ionospheric disturbances, but the converse would not be strictly true: multiple disturbances would not necessarily always result in overshoot signal perturbations. To cause an overshoot effect, there must be at least two disturbances close enough to a signal path to perturb it; the disturbances must be located so that one will perturb the signal amplitude upwards and the other will perturb it downwards [*Poulsen et al.*, 1990]; and the recovery rates of the "component" perturbations must be different. Even if multiple disturbances are the rule rather than the exception, as the evidence in this chapter suggests, these conditions for "overshoot" signatures would still be only rarely fulfilled. This evaluation is consistent with the paucity of overshoot signatures in our data at large, comprising less than 1% of all perturbations observed.

5.3 SPATIAL ASSOCIATION OF WHISTLERS AND INFERRED IONOSPHERIC DISTURBANCES

The temporal associations between ducted whistlers and signal perturbations we have discussed so far not only support a cause-effect relationship between the two, but imply that the phenomenon is global and widespread. Precipitation zones may exist at the northern and southern feet of every excited whistler duct. To explore this possibility more deeply, we now turn to the spatial correspondence between ducted whistlers and signal perturbations, which we investigate by looking for an association between duct exit locations and the locations of ionospheric disturbances. Such a comparison was first performed in a preliminary survey by *Carpenter and LaBelle* [1982], who found a statistical correlation between the arrival azimuths of ducted whistlers at Palmer and the arrival azimuths of subionospheric signals which were perturbed during the same period; however, the scope of this work was limited at the time by the direction finding method available and by the lack of Northern Hemisphere signal perturbation data.

5.3.1 Electron Precipitation near Huntsville

Signal perturbations recorded on 19 April 1990, illustrated in Figure 5.8, indicate the presence of an ionospheric disturbance in the vicinity of HU. During the ten minute period shown, HU observed simultaneous perturbations on all signals except NAU, while at Palmer NPM–PA was the only perturbed path. Data from AR and LM were unavailable. The simultaneous perturbation of NPM–PA is consistent with a precipitation-induced ionospheric disturbance conjugate to HU, although the lack of perturbations on NAU–HU may indicate that the Northern Hemisphere disturbance was slightly to the north of HU.

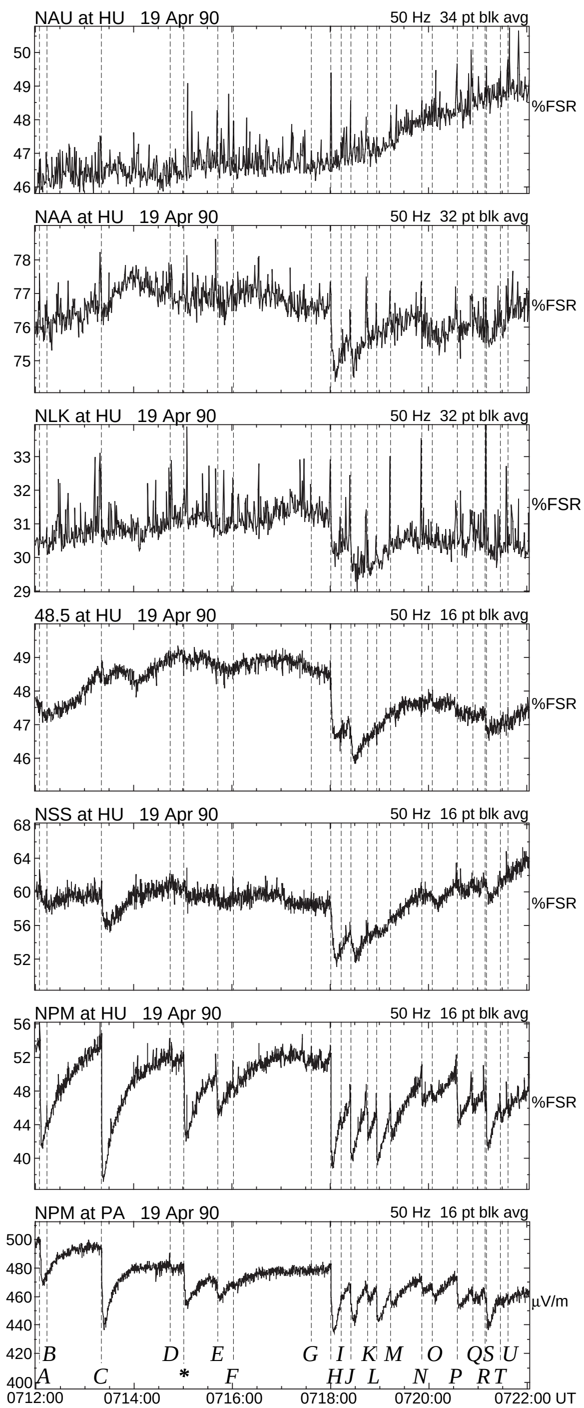

(*a*)

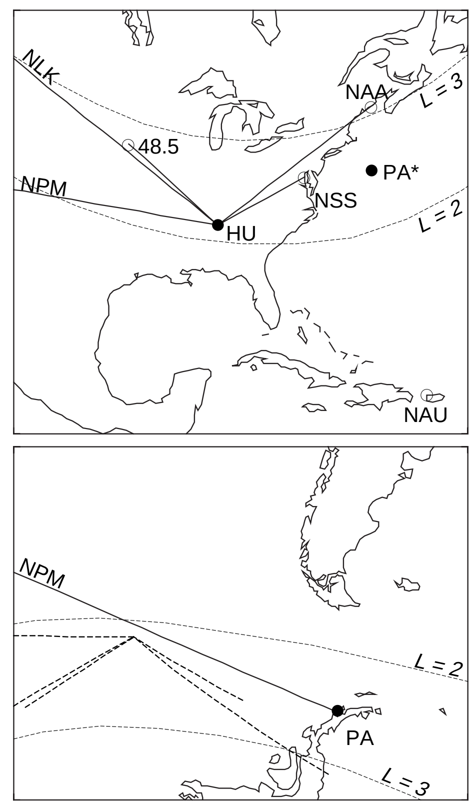

(*b*)

Fig. 5.8. Signal perturbations observed on 19 April 1990 suggesting precipitation near Huntsville. (*a*) A ten-minute period of simultaneous signal perturbations on six signal paths. NAU–HU was not perturbed but is shown at top for reference. Dashed vertical lines indicate the onset times for 22 perturbations observed on NPM–HU, 16 of which were nearly simultaneous (± 1 s) with perturbations of NPM–PA. These events are marked *A* through *U* (no broadband data were available for the event marked with an asterisk). (*b*) The format of the map is identical to that in Figure 5.1*b*. AR and LM are not shown because no data were available from those sites. The configuration of perturbed signal paths suggests the presence of one or more ionospheric disturbances in the vicinity of HU.

To facilitate the comparison of the signal perturbations with whistlers, perturbations larger than a threshold of 0.2 dB on NPM–HU or 0.1 dB on NPM–PA are marked *A* through *U*. The poorer detectability threshold on NPM–HU was due to atmospheric noise. Twenty-two events were observed on NPM–HU, of which 16 were observed near simultaneously on the more weakly perturbed NPM–PA (the 6 events not detected on NPM–PA corresponded to the weakest 6 events of the 22 measured on NPM–HU, and may simply have been below the Palmer receiver's noise floor). No broadband data were available for the event marked with an asterisk, so this event is excluded from further discussion. Of the 21 remaining marked events, all corresponded to whistlers observed at Palmer. Palmer recorded a total of 23 whistlers stronger than 2 μV/m during this period, which leaves two whistlers unassociated with any detected signal perturbation.

The arrival azimuths at Palmer of all 23 multipath whistlers, calculated including all components in each whistler, are shown in Figure 5.9. The mean arrival azimuth of the 21 perturbation-associated whistlers, determined by averaging the peaks of the azimuth main lobes shown in Figure 5.9, is 278°. This value matches the azimuths of NPM (276°) and of the conjugate of HU (273°) well within the $\pm$15° absolute azimuth error. The *L*-shell of the first component of the associated whistlers was $\sim$2.0, which compares well with that of HU (L = 2.13) and resolves the 180° arrival azimuth ambiguity in favor of the northwest. Of the two whistlers unassociated with any detected signal perturbation, one was the second weakest whistler observed (2 μV/m) and the other, though much stronger (15 μV/m), arrived from an azimuth of 345° (regrettably, LU14–which arrives at Palmer with an azimuth of 346°–was off the air during this period). Figure 5.10 compares the second unassociated whistler with the whistler for event *L*.

The correspondence on 19 April 1990 between the inferred locations of ducts and disturbances is consistent with conjugate precipitation by ducted whistlers. The fact that the only two unassociated whistlers observed were weak or from a region unmonitored by signal paths suggests that, had those whistlers also induced precipitation which caused ionospheric disturbances, such disturbances would not have been detected.

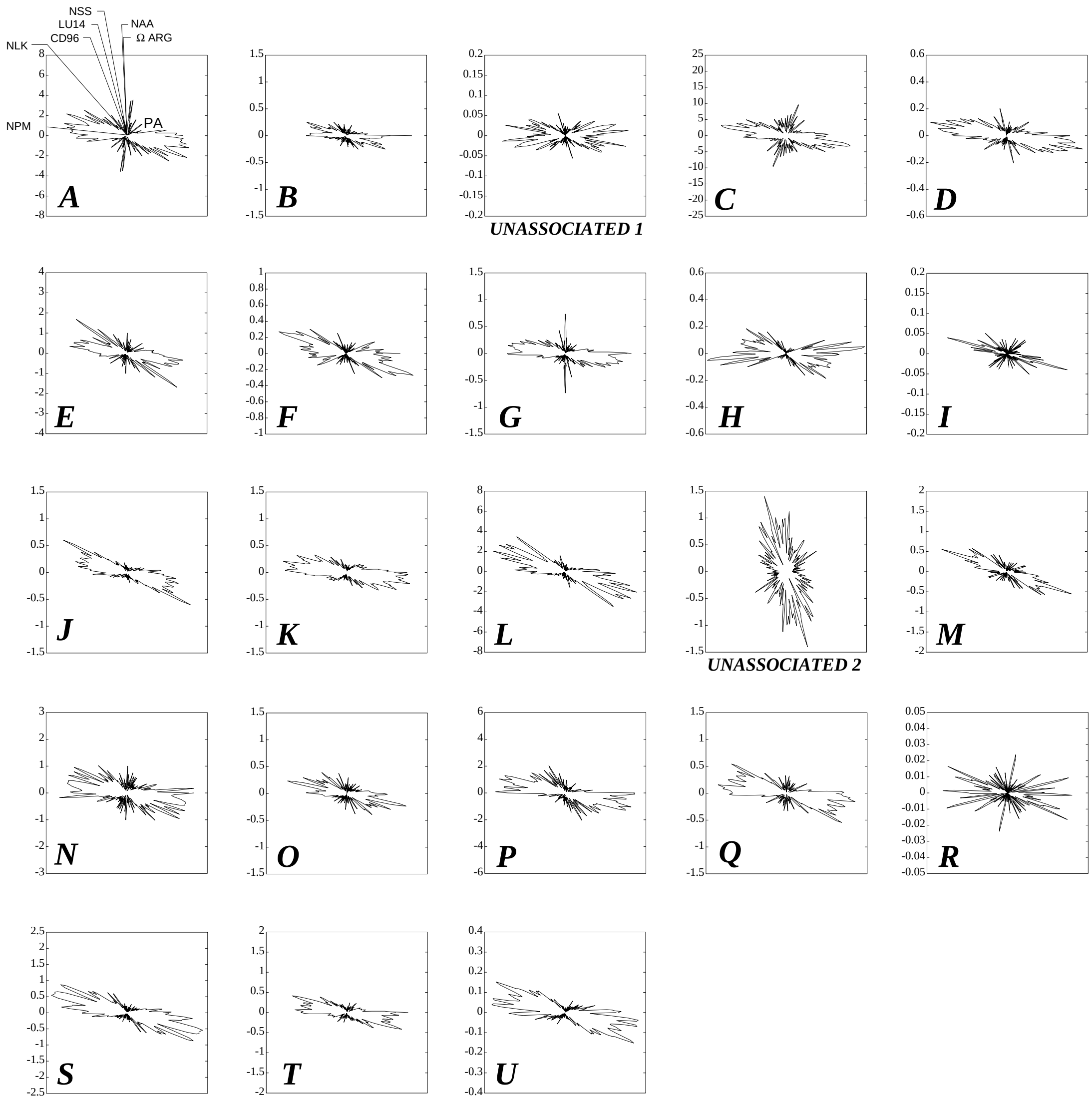

Fig. 5.9. The arrival azimuths of the 23 multipath whistlers observed at PA between 0712 and 0722 UT on 19 April 1990. The 21 lettered plots correspond to whistlers associated with the signal perturbations shown in Figure 5.8. The remaining two whistlers were not associated with detected signal perturbations. All whistlers arrived from lower L-shells than that of PA ($L \simeq 2.4$) which resolves the 180° ambiguity in each plot in favor of the northwestern lobe. The average main lobe peak azimuth for the associated whistlers was 278°, which matches the azimuth of NPM (276°) and of the conjugate of HU (273°) within the $\pm 15°$ absolute azimuth error. Of the unassociated whistlers, one was the second weakest observed and the other, though relatively strong, arrived from a different direction. The plots were generated by sampling the arrival azimuth of each whistler along its curve in the frequency-time plane, and weighting each azimuth sample by the corresponding intensity of the whistler. All whistler components were included in each analysis. The plots are oriented with the top of the page representing geographic north. The relative amplitude scales are only approximately uniform due to the weighting method used.

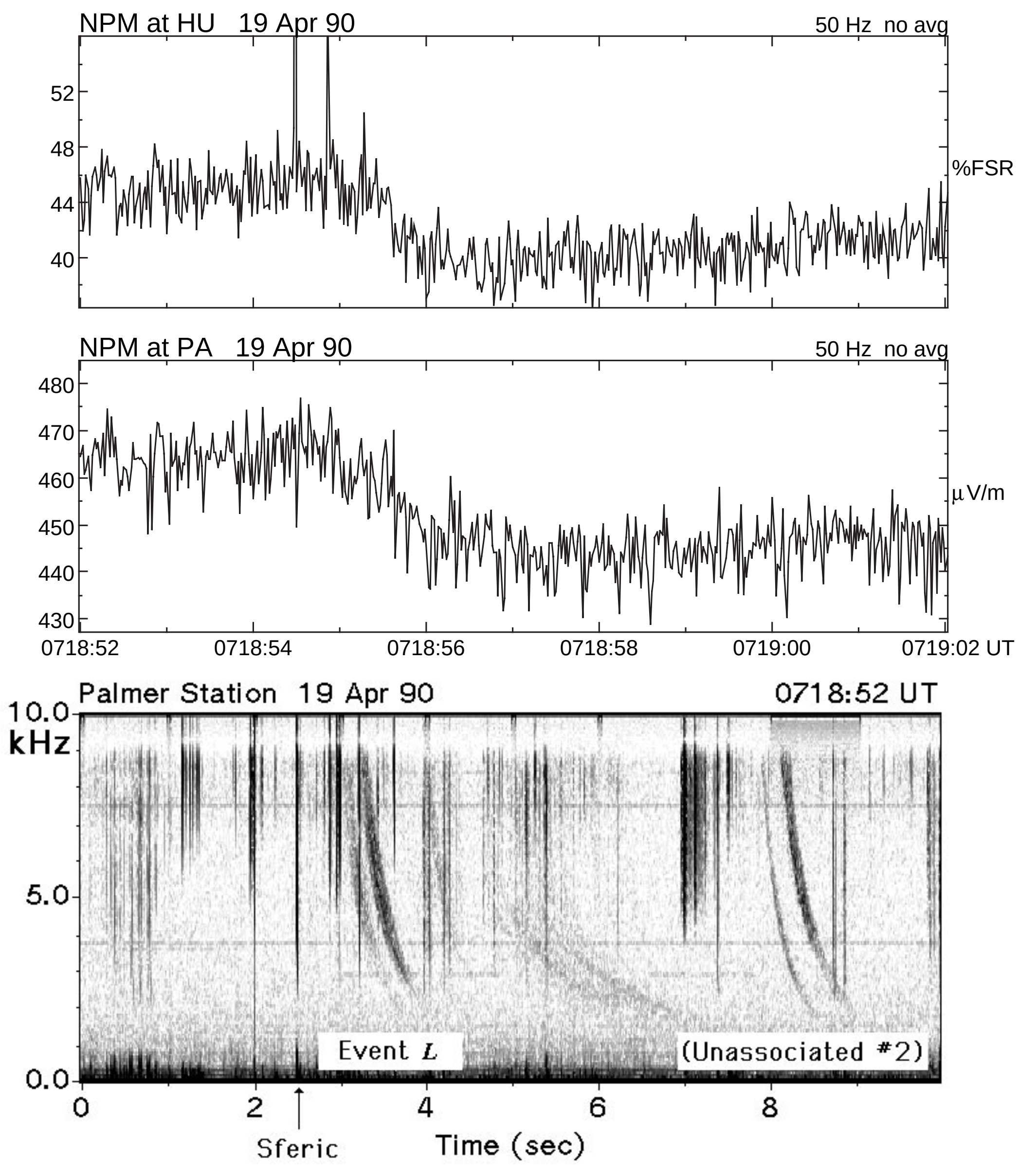

Fig. 5.10. Whistler association and lack of association on 19 April 1990. Two signal perturbations and the whistler associated with event *L* are compared with the lack of perturbations and the second unassociated whistler from the period shown in Figure 5.8. A weak three-hop echo of the event *L* whistler is also visible (see Chapter 2).

The clustering of the multipath whistlers' arrival azimuths in the direction of the HU conjugate suggests the presence of multiple ducts, and therefore multiple disturbances, in the vicinity of HU. The fact that not all paths at HU were perturbed by the same relative magnitudes in each event, as seen especially for events *C*, *H*, and *S* on the 485–HU, NSS–HU, and NPM–HU signals in Figure 5.8, is consistent with the disturbance of multiple ionospheric regions near HU by different relative amounts on each occasion. This interpretation is reinforced by the difficulty in explaining these changing relative signal perturbation magnitudes in terms of a sequence of disturbances occurring in a single location. In this case, the varying relative signal perturbation magnitudes from one event to the next would mean that changes in the structure of each individual ionospheric disturbance were affecting the waveguide response of each perturbed signal differently. It seems unlikely, however, that precipitation bursts associated with the same duct, and therefore presumably with similar energy distributions, would induce profiles of secondary ionization which varied sufficiently from event to event to affect waveguide responses differently. Note that the 16 perturbations observed simultaneously on NPM–HU and NPM–PA exhibited uncannily constant relative magnitude (Figure 5.11) despite their resulting from disturbances inferred to be in opposite hemispheres.

The onset behavior of conjugate signal perturbations on 19 April 1990 is compared with LEP theory in Section 5.4.

5.3.2 Arrival Azimuths of Multipath Whistler Components

Arrival azimuth measurements on individual components of multipath whistlers can shed light on the relationship between multipath whistlers and multiple ionospheric disturbances. If multiple, simultaneous disturbances correspond one-to-one with the ducts excited by a multipath whistler, and those disturbances perturb subionospheric signals, then there should be at least one duct exit near every perturbed signal path, probably within 200 km (Figure 1.7).

Figure 5.12 shows the simultaneous perturbation of four signal paths observed at PA

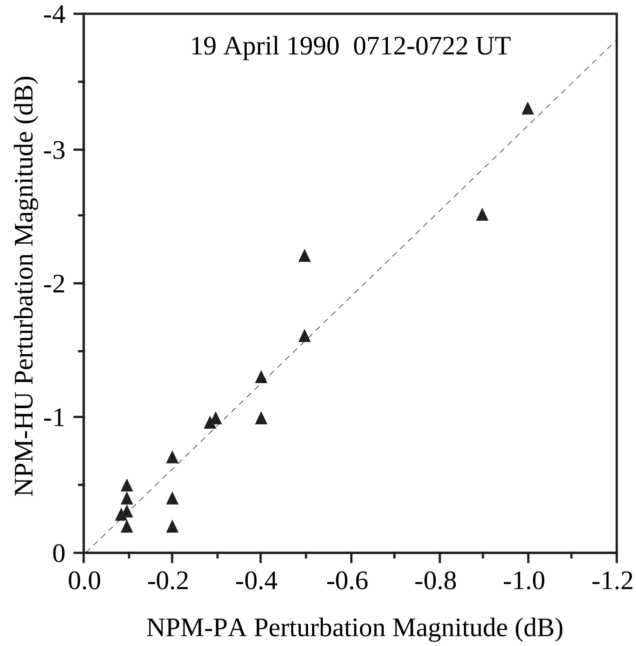

Fig. 5.11. The relative magnitude of 16 nearly simultaneous perturbations observed on NPM–HU and NPM–PA on 19 April 1990 was almost constant, consistent with twin ionospheric disturbances, one in each hemisphere, caused by conjugate precipitation bursts with similar energy spectra. The disturbances are unlikely to have been in the vicinity of the NPM transmitter because simultaneous perturbations were observed on other signals arriving at HU (see Figure 5.8). The least squares fit shown has a slope of 3.2 to one, a y-intercept of -0.02 dB, and represents a correlation coefficient of 0.96. Perturbation measurements have an error of $\pm$0.1 dB.

and one at AR. Other signals monitored at the two sites were not detectably perturbed, and no data were available from HU or LM. Twenty-six perturbations greater than 0.1 dB were observed on NPM–PA during the half-hour shown. All 26 events were associated with multipath whistlers with maximum intensities ranging from 5 to 53 μV/m. It is difficult to postulate a single conjugate pair of spatially extensive disturbances to explain the observations, because several other signals propagating within both conjugate regions were not detectably perturbed. The observations thus appear to be more consistent with multiple smaller disturbances.

Arrival azimuths measured for the components of the associated whistlers are consistent with a duct-disturbance association. Figure 5.13 shows an example of an associated whistler, in which three major components are identified as α, β, and γ. These three components

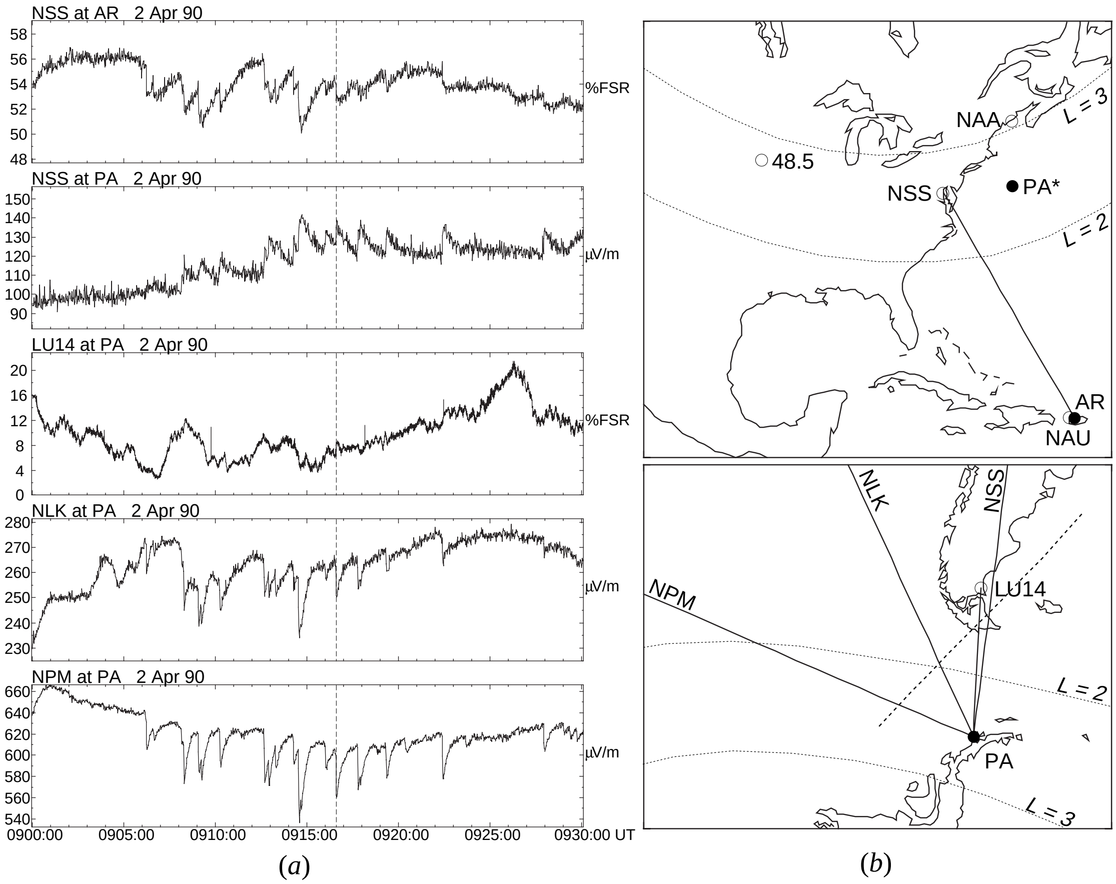

Fig. 5.12. Signal perturbations on 2 April 1990 suggesting multiple precipitation zones. (*a*) Thirty minutes of narrowband signal amplitudes. The dashed vertical line indicates the onset of a perturbation event to be examined in greater detail. No other observed signal paths at AR or PA were perturbed, and no data were available from HU or LM. (*b*) The format of the map is identical to that in Figure 5.1*b*.

were strong and isolated enough for their azimuths to be analyzed individually, with the results shown in Figure 5.14. The α component arrived at Palmer from the same direction as NSS and LU14, two of the perturbed signals. The β component arrived from the same direction as NLK, which was also perturbed.

When L-shells of α, β, and γ are also considered, the resulting position "fixes" do not indicate ducts on or near NPM–PA or NSS–AR, both of which were strongly perturbed. As we have already seen, however, NPM–PA perturbations can be associated with extremely weak whistlers. Such whistlers could easily have been overwhelmed in the azimuth analysis

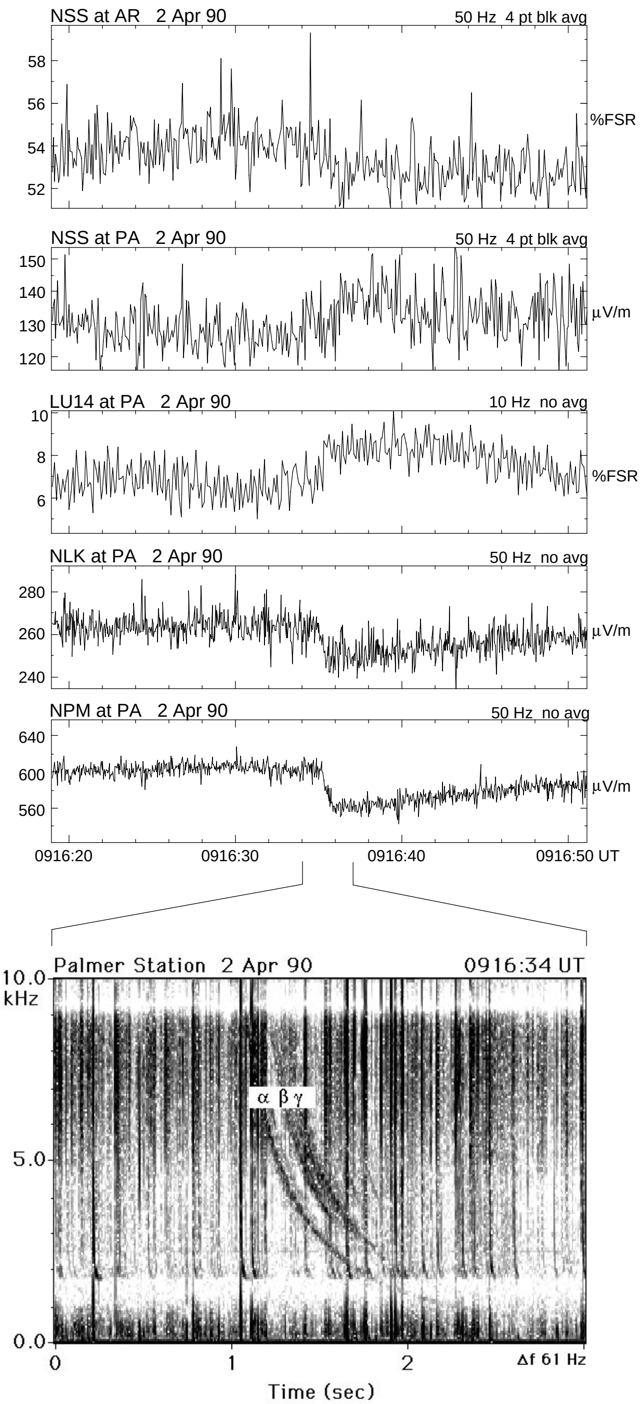

Fig. 5.13. The simultaneous signal perturbation event marked in Figure 5.12 is shown in greater detail, and compared with the associated whistler. Although the whistler involved at least seven components, three components were strong and isolated enough to attempt an estimate of their individual arrival azimuths.

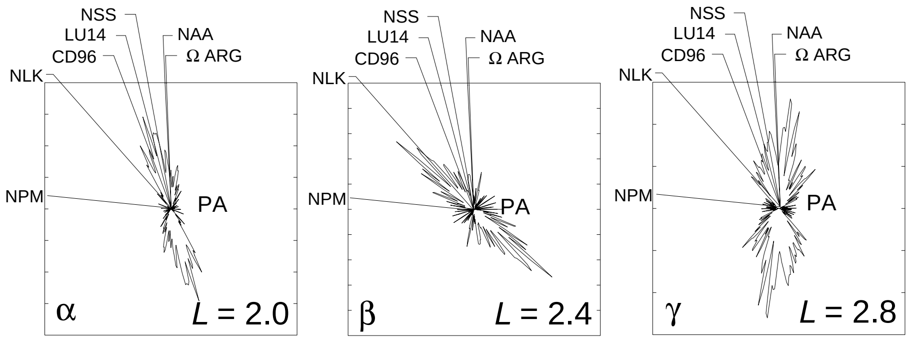

Fig. 5.14. Arrival azimuths of the three whistler components identified in Figure 5.13. Component γ arrived from the south of Palmer, so the upper lobe of its azimuth plot should be disregarded.

by noise or by stronger whistler components from other directions. The lack of an identifiable duct associated with NSS–AR may be due to a similar cause.

The duct associated with the β component appears to have been within ± 0.1 *L*-shell of Palmer. The lack of detectable perturbations on three of the seven signals monitored at Palmer, despite the apparent proximity of the β duct and its inferred associated disturbance, is not inconsistent with *Poulsen et al.*'s [1993] subionospheric VLF wave scattering model. This model suggests that wave scattering from whistler-induced ionospheric disturbances is mostly into a near-forward direction. Thus, if the disturbance was located on the NLK–PA path as implied by the arrival azimuth of the associated whistler, considerable sideways scattering by the disturbance of any other monitored signals, such as NAA for example, would be required to result in detectable perturbations of those signals at Palmer.

5.4 SIGNAL PERTURBATION ONSETS AND PRECIPITATION THEORY

The possibility that every ducted whistler component can induce precipitation is consistent with the theory of gyroresonant interaction between ducted whistlers and radiation belt electrons developed by *Chang and Inan* [1985]. No theoretical evidence was found which suggests any abrupt thresholds in the ability of ducted whistlers to scatter electrons. But while the theory has been successfully applied to precipitation bursts observed *in situ* [*Inan et al.*, 1989], lack of high-time-resolution narrowband recordings has prevented all but limited comparison with ground-based signal perturbation data [*Carpenter et al.*, 1984; *Inan et al.*, 1985*a*].

To determine if signal perturbations are consistent with the *Chang and Inan* [1985] model of electron scattering and precipitation by ducted whistlers, we compare the timing of predicted conjugate precipitation bursts with observed perturbation onsets in the Northern and Southern Hemispheres. Examples of conjugate perturbation onsets during a half-hour period on 19 April 1990 and a four-minute period on 21 March 1989 (also studied in Chapter 4) are shown in Figure 5.15. Six events from 19 April and two events from 21 March were selected for analysis using clarity of onset and lack of interfering atmospheric noise as criteria. The events were then superposed to further improve onset definition.

For a superposition time reference, we used the estimated time that the causative sferic first entered a magnetospheric duct. To find this time, we assumed that the source lightning occurred over the eastern United States, an assumption supported by strong narrowband causative sferics at HU on 19 April 1990 and by lightning detection data on 21 March 1989 (Figure 4.1). We assumed further that the propagation delay between the location of the lightning flash and the region where the resulting sferic coupled into the magnetosphere is negligible. These assumptions allow us to estimate initial magnetospheric entry time as the time of the associated whistler causative sferic recorded at Palmer minus 39 $\pm$ 5 ms of propagation delay from the flash location to Palmer.

The initial electron precipitation pulse in the Northern Hemisphere (pulse I) was scaled in time from a prediction for L = 2 and N_{eq} = 1300 el cm^{-3}, made using a comprehensive treatment of scattering by ducted whistlers, presented in Figure 11*b* of *Chang and Inan* [1985]. Time scaling of the original pulse was necessary to correct for observed values of associated whistler L and N_{eq}, and was performed based on the difference in peak flux arrival time (t_p) as predicted by a simple model of equatorial electron gyroresonance with a reference wave

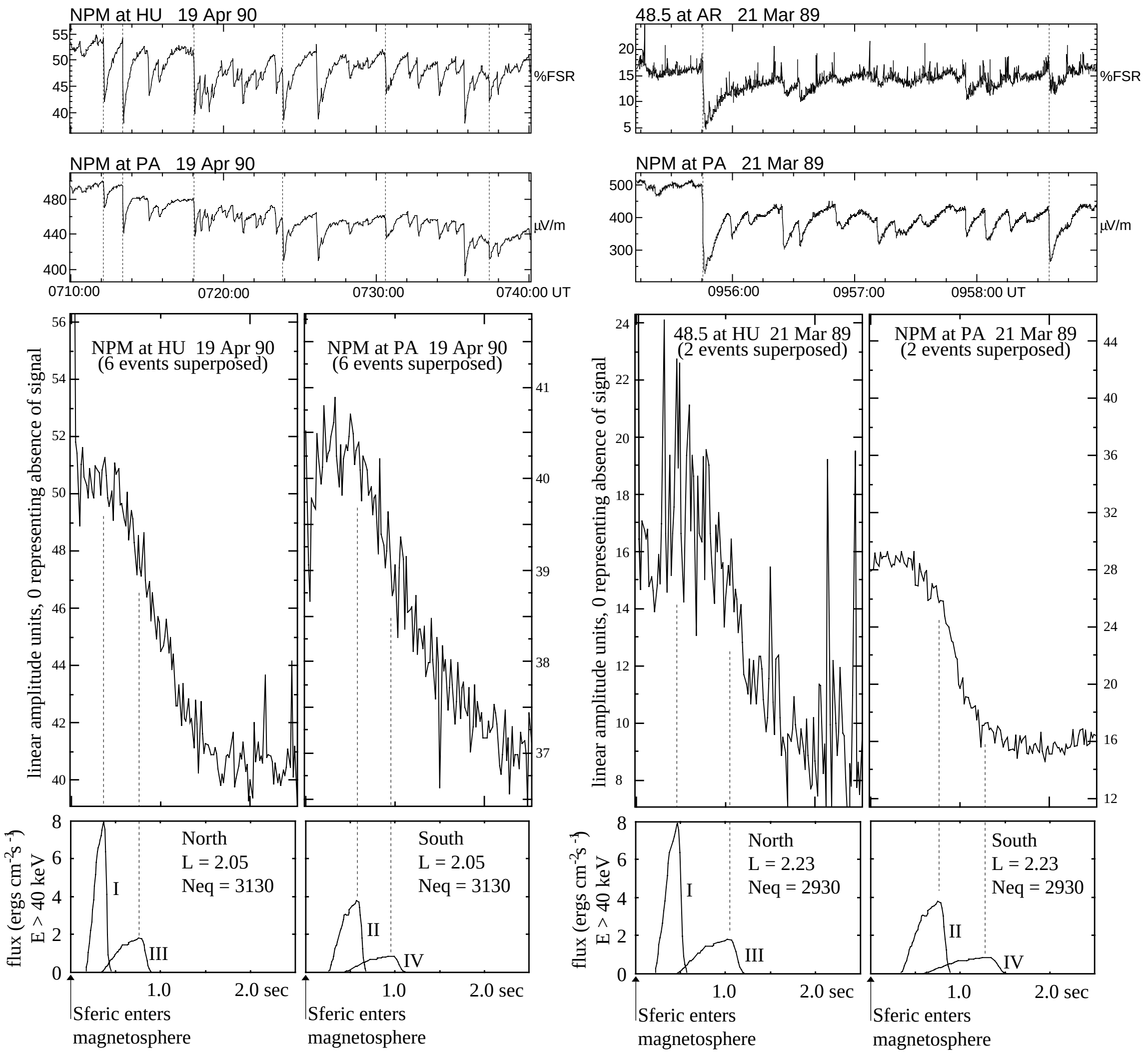

Fig. 5.15. A comparison of observed signal perturbation onset behavior with the timing of theoretical electron precipitation pulses, which were modeled based on scattering of radiation belt electrons by ducted whistlers. The left panels show the superposition of six signal perturbations selected from a half-hour period on 19 April 1990, and the precipitation pulses predicted using the L-shell and N_{eq} corresponding to the associated whistlers. The right panels show a similar analysis of two superposed events from a four-minute period on 21 March 1989. Superposition was carried out using as a $t = 0$ reference the Northern Hemisphere causative sferic, which is noticeable at the beginning of the Northern Hemisphere superposition panels. The bouncing pulses are labeled in the order in which they strike the Earth, with I and III striking the Northern Hemisphere and II and IV the Southern Hemisphere. The perturbation onsets compare well with the timing of the predicted precipitation, except for pulse I on 21 March. The lack of a detectable perturbation in association with this pulse is consistent with the relatively small flux on the edge of the northern loss cone in the vicinity of the South Atlantic Magnetic Anomaly (see Figure 5.16).

at a given frequency f_{ref}. Whistler-mode propagation delay at $f = f_{ref}$ was modeled as a function of L and N_{eq} using the dispersion predicted by (3.12), assuming a ratio of whistler nose frequency to equatorial gyrofrequency (Λ_n) given for a diffusive equilibrium electron distribution by *Bernard* [1973]. We found that choosing f_{ref} = 6.3 kHz was all that was necessary to calibrate the model to within $\pm$30 ms of the t_p curve for 1.8 $\leq L \leq$ 2.4 and N_{eq} = 8128 $\times$ $10^{-0.359L}$ el cm^{-3} given in Figure 8 of *Chang and Inan* [1985]. We then used the model with measured values of whistler L and N_{eq} to estimate t_p and time-scale the original precipitation pulse for the observed cases.

The first precipitation pulse to strike the Southern Hemisphere, which is the second pulse to approach the Earth (pulse II), was time-scaled from Figure 11*d* of *Chang and Inan* [1985] using the same simple model for t_p except with the addition of a one-hop bounce time for loss-cone electrons that would resonate at the equator with 6.3 kHz. This choice of bounce time is only a ballpark estimate for the range of electron energies that would be involved in the precipitation burst, but it is adequate at relativistic energies where velocity no longer varies as the square root of energy (Figure 2.10); for example, bounce periods for electron energies of 50 and 500 keV at a given L-shell and pitch angle differ by only about a factor of two. Bounce periods of 6.3 kHz-resonant loss-cone electrons are 0.33 s (128 keV, L = 2.05) and 0.47 s (64 keV, L = 2.23) for the 19 April and 21 March cases, respectively, shown in Figure 5.15.

The later precipitation pulses (pulse III in the Northern Hemisphere and pulse IV in the Southern Hemisphere) were predicted from pulses I and II by keeping the time delay between pulse beginnings constant, and likewise for pulse endings. No modification was made to the original amplitudes of pulses I and II, which *Chang and Inan* [1985] calculated assuming 100% mirroring or backscatter and ignoring any loss cone asymmetry. The amplitudes for pulses III and IV were generated from pulses I and II by keeping the peak amplitude ratio of a given pulse to the previous pulse constant.

In the 19 April case, experiment agrees well with theory. The Northern Hemisphere is perturbed earlier than the Southern Hemisphere, as expected. The predicted onset delay does appear perhaps 0.2 seconds too short, but this may be due to selection of the leading whistler component to provide *L* and N_{eq}. As discussed earlier, several whistler components were observed and a later one may have been responsible for the disturbances which perturbed NPM–HU and NPM–PA. If so, the delays associated with a later component would reduce the discrepancy in the prediction.

The 21 March data also appear to agree well with predictions, with one exception: one detects no signal perturbation in association with pulse I. The Southern Hemisphere is perturbed first. As pointed out in Chapter 4, this effect can be expected at longitudes of the South Atlantic Magnetic Anomaly, since the population near the northern loss cone is far less than that near the southern loss cone. As demonstrated in Figure 5.16, it is possible for pulse I to be far weaker than pulse II – in contrast to what is shown in Figure 5.15 – because fewer electrons are available for precipitation into the Northern Hemisphere [*Inan et al.*, 1988*c*]. That the Southern Hemisphere was perturbed first on 21 March 1989 but not on 19 April 1990 suggests that the near-loss-cone electron distribution may have been different on the two days.

The onset durations exhibited in both cases extend well beyond the end of the first causative precipitation pulse (pulse I in the Northern Hemisphere, pulse II in the Southern Hemisphere). This observation is consistent with the continuing disturbance of the conjugate ionospheric regions by pulses III and IV, and possibly by later pulses as well. Such successive precipitation pulses of diminishing flux have been observed *in situ* in association with ducted whistlers [*Voss et al.*, 1984].

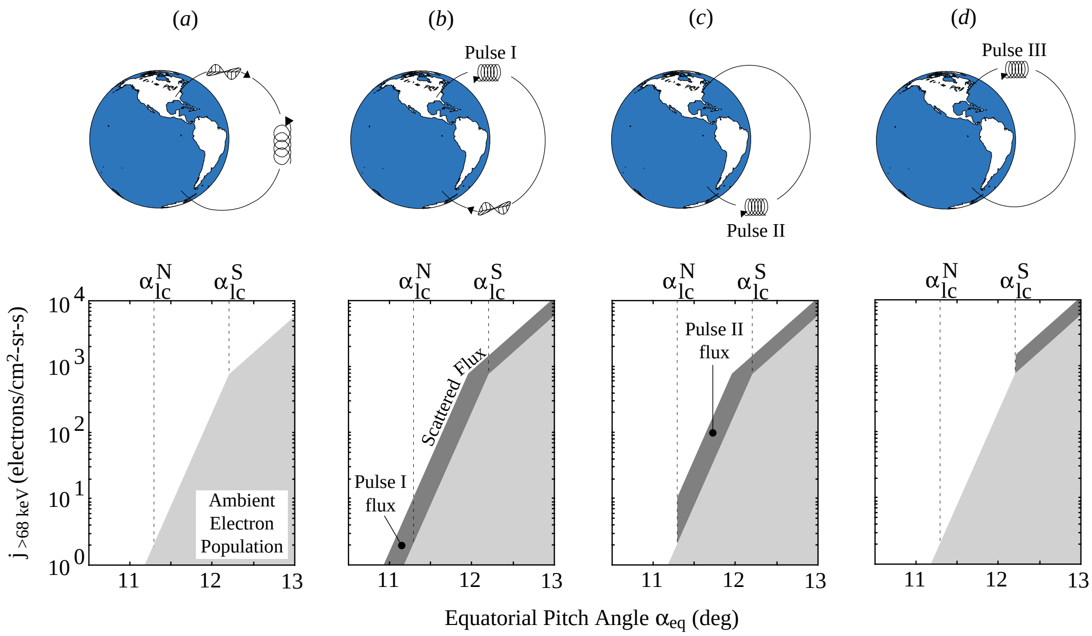

Fig. 5.16. The effect of the South Atlantic Magnetic Anomaly on electron precipitation from the Radiation Belts. (*a*) The Anomaly results in two loss cones: electrons with equatorial pitch angles inside the northern loss cone ($\alpha_{eq} < \alpha_{lc}^{N}$) precipitate in the Northern Hemisphere, while those with pitch angles inside the southern loss cone ($\alpha_{eq} < \alpha_{lc}^{S}$) precipitate in the Southern Hemisphere. (*b*) When loss-cone electrons are pitch-angle scattered by a whistler, the total additional electron flux inside the northern loss cone is orders of magnitude less than that inside the southern loss cone, so that pulse I may be far smaller than (*c*) pulse II. (*d*) Pulses III and beyond would consist primarily of backscattered electrons. The ambient population profile is adapted from Figure 3 of *Inan et al.* [1988*c*]; see also Figure 2.14.

6

The Contribution of Ducted Whistlers to Radiation Belt Losses and Equilibrium

The evidence presented in Chapter 5 suggests that every ducted whistler component precipitates radiation belt electrons. Assuming this is so, this chapter estimates a first-order lower bound on the resulting radiation belt losses by comparing ground-observed whistler intensities and occurrence rates with whistler-associated precipitation flux measured *in situ*. We constrain this analysis to $2 < L < 3$, identified in previous work as the region where most whistler-associated precipitation of >50 keV electrons is expected [*Chang and Inan*, 1985] and appears to occur [*Carpenter and Inan*, 1987].

6.1 EQUATORIAL WHISTLER INTENSITY

We begin by estimating a representative equatorial wave magnetic field (B_{dw}) for the "average" precipitation-inducing ducted whistler. Since *in situ* data on ducted whistler intensities are not available, we infer wave intensity in the duct from ground measurements. First, analysis of whistler arrival azimuth and *L* is used to locate the duct exit point and estimate attenuation resulting from the relative orientation of the receiving antenna. Given the distance between the duct exit point and Palmer, we apply an Earth-ionosphere waveguide spreading loss of 14 dB in the first 200 km [*Tsuruda et al.*, 1982], followed by waveguide attenuation of 1.6 dB per 100 km up to 1000 km and 0.8 dB per 100 km thereafter, as adapted from Figure 3.9 of *Crary* [1961]. After accounting for subionospheric attenuation, we are left with an estimate for the field strength just below the ionosphere in the vicinity of the duct exit point. From this we find the equatorial wave field in the duct using the approach of *Inan et al.* [1984], including lower nighttime ionospheric absorption loss for a 2 kHz signal as given in Figure 3-35 of *Helliwell* [1965], changes in the refractive index, and the expansion of duct cross-section with decreasing geomagnetic field intensity.

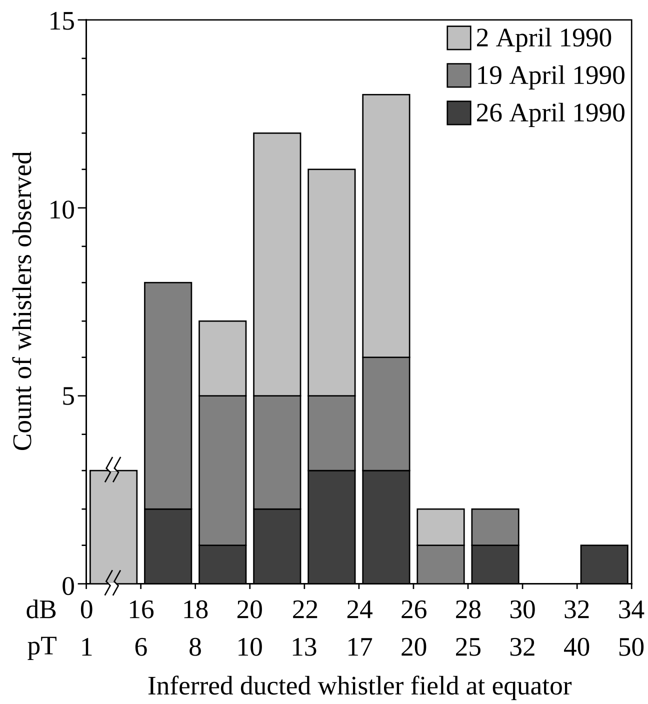

Fig. 6.1. Equatorial ducted whistler wave magnetic fields inferred from ground measurements of 59 whistlers on three different days. The average equatorial ducted field (B_{dw}) is 12 pT. A feature of the data from all three days is a noticeable drop in the number of whistlers observed over 20 pT, possibly indicating a threshold in the efficiency with which lightning generates radio atmospherics and/or ducted whistlers.

Applying this method to 59 perturbation-associated whistlers recorded on three different days yielded an average duct equatorial field of B_{dw} = 12 pT (Figure 6.1). Equatorial resonant energies for loss-cone electrons scattered by these whistlers would have ranged from 70 to 700 keV, based on the observed bandwidths of the whistler traces and their associated L and N_{eq} values. For the purpose of discussion we will henceforth take 70 keV as the lower limit of the energy of electrons scattered by ducted whistlers.

6.2 SIZE OF THE REGION MONITORED FOR WHISTLERS

The next task is to estimate the size of the region for which long-term whistler rate data from a single site might indicate the quantity of associated electron precipitation. Let us say we wish to count at least 95% of precipitation bursts within this region. Of the 59 whistlers just mentioned, 95% (56) corresponded to equatorial fields stronger than 6 pT; we therefore define our range as the greatest distance between a duct exit point and Palmer for which we can identify a whistler which would have had an equatorial field $\geq$6 pT. A conservative threshold for the weakest routinely detectable whistlers at Palmer might be 5 μV/m. Applying the method used earlier, we find that a whistler with an equatorial duct field of 6 pT would reach Palmer at this detection threshold if the duct exit point were 2500 km from Palmer. Palmer should thus be able to detect 95% of whistlers exiting ducts within 2500 km. This assumes that the downcoming whistlers illuminate the Earth-ionosphere waveguide equally in all directions, which may not be a good assumption: *Helliwell* [1965] showed that VLF waves would tend to propagate towards the geomagnetic pole when leaving a duct. On the other hand, since we are concerned with $2 < L < 3$, and since Palmer lies at L = 2.4, this effect would only lead to a conservative undercount of $2.4 < L < 3$ whistlers.

Assuming that a ducted whistler induces radiation belt losses only from within its duct, we will average precipitation flux from the area of a single duct (A_{duct}) over the area of the entire monitored region (A_{region}). Using our range estimate above, the region over which Palmer could detect precipitation-associated whistlers would be 5000 km wide between L = 2 and L = 3, or about 6,600,000 km^2 at 100 km altitude (Figure 6.2). Scaling *Angerami*'s [1970] estimate of the cross-sectional area of a duct to 100 km altitude gives 370 km^2. Thus the fraction of the monitored area covered by a single duct is $A_{\text{duct}}/A_{\text{region}} \simeq 6 \times 10^{-5}$.

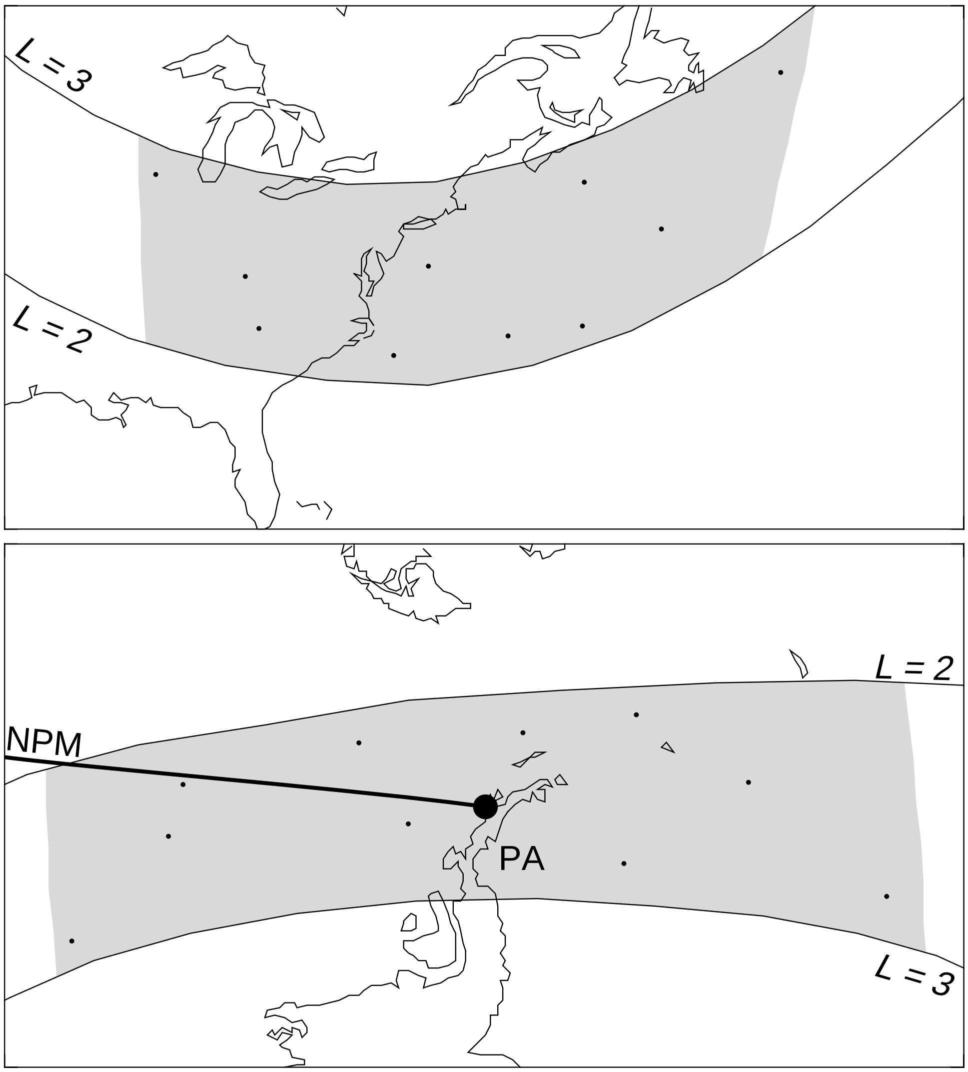

Fig. 6.2. The region monitored for whistler-induced precipitation by Palmer Station, Antarctica. The shaded region in the lower panel indicates the 5000 km wide area between $L = 2$ and $L = 3$, discussed in the text, within which 95% of whistlers exiting ducts would be detected at Palmer. The geomagnetic conjugate of this area is shaded in the upper panel. For the purpose of illustration, the endpoints of ducts guiding a hypothetical ten-path whistler are shown as dots about 30 km in diameter scattered arbitrarily throughout the region. One duct endpoint is pictured close to the NPM–PA path, where precipitation spatially associated with that duct might cause a signal-perturbing ionospheric disturbance. The evidence in Chapter 5 suggests that every multipath whistler results in multiple small precipitation zones, located at the conjugate endpoints of excited ducts and spread over thousands of kilometers.

6.3 BELT LOSSES FOR A REPRESENTATIVE WHISTLER COMPONENT

We now estimate the percentage of flux lost from a duct due to precipitation by an average whistler component, which we will write as $\Phi_{\text{loss}}/\Phi_{\text{duct}}$. The best starting point appears to be S81-1 satellite observations reported by *Voss et al.* [1984], who found a precipitation loss of omnidirectional flux density of $\sim$0.001% in association with a whistler measured at Palmer to be 15 μV/m at 1.5 kHz [*Inan et al.*, 1989]. The whistler and precipitation pulse were marked as event "D" by *Voss et al.* [1984]. We use this reported flux loss percentage with caution; it represents only a single case, and is uncertain by a factor of $\sim$2 because S81-1 was unable to directly observe southern loss cone electrons mirroring above it and because much of the precipitating flux it did observe was at the edge of the detectors' field of view (M. Walt, private communication, 1992). Furthermore, to use this finding as a reference, we must assume that the satellite was measuring scattered electrons from within a duct and that the whistler observed at Palmer had propagated in that duct and caused that scattering. We consider the validity of these assumptions one at a time.

During the 40 s period discussed by *Voss et al.* [1984] the S81-1 satellite observed four precipitation bursts over a distance of $\sim$290 km. *Angerami* [1970] estimated the horizontal extent of ducts to be 15–27 km at 300 km altitude, and at the 230 km altitude of the S81-1 satellite, such ducts would be only a couple of kilometers smaller. It is not unreasonable that four ducts of this size may have been coincidentally clustered in the region traversed by the satellite, especially when one considers that back-to-back examples of precipitation are rare in the S81-1 data (H. D. Voss, private communication, 1992). Such clustering of ducts appears to be possible: the 19 April 1990 data discussed in Chapter 5 were consistent with multiple ducts in the vicinity of Huntsville (which, interestingly, is located only $\sim$350 km from the ground trajectory of the S81-1 satellite during the *Voss et al.* [1984] measurements).

If the observed precipitation was indeed confined to ducts, however, those ducts may have been larger than suggested above. The 8 km/s speed of the S81-1 satellite would bring it from one edge of a 24 km duct to the other in 3 s, yet in the four events reported by *Voss* *et al.* [1984] the precipitation bursts were observed to last 3–5 s. We could infer somewhat larger ducts to account for the 5 s observations, say $\sim$40 km, but even then it is unlikely that the satellite's time in a duct and the duration of precipitation would so closely coincide four times in a row. These considerations may indicate that *Angerami* [1970] underestimated the horizontal extent of ducts, and that a closer estimate might be 60–70 km at 230 km altitude. If ducts and ionospheric disturbances are linked, as suggested in Chapter 5, this estimate is consistent with the $<$100 km extent of whistler-associated disturbances reported by *Carpenter and LaBelle* [1982] and *Inan et al.* [1990]. Such duct sizes would increase the $A_{\text{duct}}/A_{\text{region}}$ ratio nearly tenfold.

Even if we take the ducts for granted, it is not obvious that the whistler component whose intensity was recorded at Palmer was responsible for the precipitation in event D. If there were several ducts, the measured intensity might correspond to a whistler propagating in any one of them.

Laying this reservation aside for the moment, we can estimate the equatorial intensity of the ducted whistler using the method developed earlier. Given that the foot of the satellite's L = 2.24 field line (and therefore presumably the foot of the duct) was about 1800 km from Palmer, the equatorial duct field corresponding to 15 μV/m on the ground would have been about 34 pT. When compared with the other duct fields obtained earlier with the same method (Figure 6.1), 34 pT is almost three times the average field and is in the top 3% of observed field strengths. Since precipitation event D discussed by *Voss et al.* [1984] was also unusually strong–in the top 10%–compared with others observed on S81-1 (H. D. Voss, private communication, 1992), it is at least not inconsistent with the available data to associate the observed whistler intensity with event D.

With this reference associating a duct field (34 pT) with belt losses in the duct (0.001%) at L = 2.24, we can estimate losses associated with more typical whistlers. Because scattering is thought to be linearly related to wave field under these circumstances [*Inan et al.*, 1982;

Chang and Inan, 1985], the "average" precipitation-inducing whistler, at 12 pT, might cause a loss of $\Phi_{\text{loss}}/\Phi_{\text{duct}} \simeq 0.0004\%$ in omnidirectional flux density in a duct at $L = 2.24$.

The absolute equatorial wave fields just discussed may not be accurate: in a case study of event D, *Inan et al.* [1989] found that the best agreement between scattering theory and the *Voss et al.* [1984] precipitation observations was obtained with equatorial fields of 200 pT. The order-of-magnitude discrepancy may reflect deficiencies in the scattering model or uncertainty in our assumptions concerning ionospheric and subionospheric wave propagation losses. Nevertheless, since both our reference (34 pT) and test (12 pT) equatorial fields were calculated in the same way, their relative strength should still be useful.

6.4 WHISTLER OCCURRENCE STATISTICS

Table 6.1 lists average values for whistler rate (W) observed during a five-year survey by *Laaspere et al.* [1963] at Port Lockroy, a site about 30 km from Palmer. Since the survey counted whistlers by ear, it seems certain that multipath whistlers were interpreted as single events; therefore, because each whistler component might cause precipitation, we must multiply the whistler counts by a representative value for ducted components per whistler (N_d). Familiarity with Palmer data leads us to suggest an average of $N_d = 10$ components per whistler, leading to the corresponding whistler component rates which are also given in Table 6.1. If only a single loop antenna was used at Port Lockroy, weak whistlers arriving from unpropitious directions relative to the plane of the antenna may have been missed. Whistler rates presented in Table 6.1 may therefore underestimate the total occurring in the monitored region.

TABLE 6.1. Whistler Rates and Inferred Electron Lifetimes.

Local Conditions	Whistler Rate W (min^{-1})	Component Rate (min^{-1})	Electron τ (days)[e]
extreme day[a]	195	1560	2×10^3
average winter night[b]	22	220[d]	1×10^4
average winter day[b]	4	40[d]	7×10^4
average summer night[b]	2.4	24[d]	1×10^5
average summer day[b]	0.3	3[d]	1×10^6
year-round average[c]	6	60[d]	5×10^4

[a] Palmer Station, Antarctica, 2 April 1990, about 2200 UT
[b] Port Lockroy, Antarctica, from *Laaspere et al.* [1963]
[c] Port Lockroy, Antarctica, averaged from *Laaspere et al.* [1963]
[d] assuming an average of N_d = 10 components per whistler
[e] calculated for L = 2.24

6.5 ELECTRON LIFETIME ESTIMATES

We can now estimate a representative percentage of radiation belt flux lost per minute. In calculating this value, we assume that over the long term the N_d excited ducts are distributed uniformly with respect to L in the monitored region. This allows us to treat the quantity $N_d \times (A_{\text{duct}}/A_{\text{region}})$ as an effective "duct density" which is applicable for any chosen L and corresponding value of $\Phi_{\text{loss}}/\Phi_{\text{duct}}$. Choosing an annual average of 6 whistlers per minute for W from Table 6.1 and using N_d = 10, we have

$$\left(\frac{\Phi_{\text{loss}}}{\Phi_{\text{duct}}}\right)\left(\frac{A_{\text{duct}}}{A_{\text{region}}}\right)(W)(N_d) \simeq 1 \times 10^{-6}\ \%\ \text{min}^{-1} \tag{6.1}$$

loss of omnidirectional flux density at L = 2.24, where

$\frac{\Phi_{\text{loss}}}{\Phi_{\text{duct}}}$ is the percent loss of omnidirectional flux density in a duct per whistler,

$\frac{A_{\text{duct}}}{A_{\text{region}}}$ is the fraction of the monitored area covered by a single duct,

W is the whistler occurrence rate (per minute), and

N_d is the number of components per whistler, i.e., the number of excited ducts.

To compare this result with loss rates predicted for other radiation belt processes, we express it as an energetic electron lifetime τ. We define τ as the time in which the belt electron population at a given L in the monitored region would drop to $1/e$ of its original density, assuming that pitch-angle diffusion near the loss cone is adequate to maintain the percentage loss of omnidirectional flux per minute, but ignoring other source or loss processes. Based on the flux loss percentage just estimated, we calculate the annual average electron lifetime τ to be $\sim 5 \times 10^4$ days, or about 140 years, at L = 2.24. Lifetimes for other whistler rates are given in Table 6.1. Note that if the horizontal extent of ducts is three times *Angerami*'s [1970] estimate, as discussed earlier, these lifetime estimates would drop almost an order of magnitude.

We can compare this result to a theoretical lifetime prediction based on a "coherent diffusion coefficient" $D^c_{\alpha\alpha}$ introduced by *Inan* [1987] to describe pitch-angle diffusion of belt electrons as a result of interactions with ducted whistler-mode signals. Accounting for the localized and episodic nature of scattering by ducted whistlers, the analysis gives $\tau \simeq 2.7 \times 10^4$ days at L = 2.24, encouragingly similar to the empirical result. The details of this analysis are given in Appendix A. Note that both the empirical and theoretical lifetime inferences depend on $A_{\text{duct}}/A_{\text{region}}$, W, N_d, and the equatorial ducted whistler wave field B_{dw}.

The predicted electron lifetimes can also be compared with theoretical lifetime estimates based on scattering by nonducted plasmaspheric hiss, which were suggested by *Lyons and Thorne* [1973] to explain the equilibrium of the radiation belts. The τ for such losses at L = 2.24, presented in Figure 1 of *Lyons and Thorne* [1973], ranges from $\sim 10^5$ days for 90 keV electrons to 10^3 days for 600 keV electrons. The resemblance between these lifetimes and those estimated for ducted whistler-induced losses indicates that, at L = 2.24, losses of $\sim$70 to $\sim$200 keV electrons induced by ducted whistlers and by plasmaspheric hiss may be similar. If the suggestion by *Lyons and Thorne* [1973] that plasmaspheric hiss controls radiation belt equilibrium in the plasmasphere is correct, this analysis would indicate that ducted whistlers may share significantly in that control.

The hiss-related lifetimes modeled by *Lyons and Thorne* [1973] decrease with increasing *L*. The model predicts, for example, that the lifetime of a 100 keV belt electron will drop roughly a thousandfold between $L = 2$ and $L = 3$. The increasing efficiency of wave-particle scattering which is responsible for this drop would similarly affect interactions involving ducted whistlers. In their model of precipitation by ducted whistlers, *Chang and Inan* [1985] predicted over an order of magnitude increase in the total energy deposition of precipitation bursts from $L = 2$ to $L = 3$, while at the same time whistler-resonant electron energies fall about an order of magnitude. Together these two effects mean a hundredfold increase in the density of precipitating burst electrons. Considering the order-of-magnitude drop in the belt population density of 120–240 keV electrons from $L = 2$ to $L = 3$ [*Lyons and Williams*, 1975*a*], the total effect is a thousandfold increase in the percentage belt loss induced by whistlers. This in turn means a thousandfold decrease in whistler-associated belt electron lifetimes, similar to that expected for hiss. Losses of $\sim$70 to $\sim$200 keV belt electrons inferred to be caused by ducted whistlers and by hiss would thus appear to be comparable across the entire $2 < L < 3$ range.

6.6 DISCUSSION

Satellite studies of radiation belt recovery after geomagnetic storms and upper atmosphere nuclear weapons tests have yielded evidence of very short electron lifetimes. Following an intense storm in November 1968, for example, *West et al.* [1981] reported Ogo 5 satellite observations of $\tau = 49$ days for 158 keV electrons at $L = 2.4$. Although *West et al.* [1981] pointed out the consistency of their experimental results with theoretical hiss-related lifetimes presented in Figure 7 of *Lyons et al.* [1972], such short lifetimes do not agree with the quiet-time hiss-induced losses suggested by *Lyons and Thorne* [1973] nor with the ducted whistler-induced losses estimated in this chapter.

The wide range of predicted values for hiss-related lifetimes results primarily from differences in total wave intensity (B_w) used in the hiss-induced loss model. While *Lyons and Thorne* [1973] found that B_w = 10 pT led to an accurate prediction of quiet-time radiation belt populations inside the plasmasphere, *Lyons et al.* [1972] used B_w = 35 pT to predict the short lifetimes later corroborated by *West et al.* [1981]. In the context of the model offered by *Lyons and Thorne* [1973], however, B_w = 35 pT is inconsistent with the quiet-time structure of the radiation belts. For example, if B_w = 35 pT had been used instead of B_w = 10 pT to model the ambient quiet-time population for 500 keV electrons at L = 2, the resulting population prediction would have been over five orders of magnitude less [*Lyons and Thorne*, 1973].

Therefore, if hiss- and whistler-induced losses are responsible for the short electron lifetimes observed following injection events, the equilibrium loss rates just discussed would have to rise during injection recovery. *Smith et al.* [1974] have documented elevated post-storm values of B_w suggestive of such an increase in hiss-induced losses, and post-storm increases in ducted whistler rates have also been observed [*Andrews*, 1975]. The tandem intensification of hiss-induced and whistler-induced losses after storms would be consistent with the suggestion by *Lyons and Williams* [1975*b*] that the relative strengths of source and loss processes remain the same before and after injection events. On the other hand it is possible that neither hiss- nor whistler-induced losses dominate the radiation belts, because an interdependence between loss rates and belt population would be inconsistent with the observed exponential character of post-storm belt recoveries [*West et al.*, 1981].

We emphasize that these preliminary results apply only to the region monitored by Palmer Station (Figure 6.2), an area which is not typical of other longitudes. The region is conjugate to frequent thunderstorm activity in the eastern United States, which may partly explain the observation near Palmer of what are possibly the world's highest whistler rates [*Laaspere et al.*, 1963]. The presence of the South Atlantic Magnetic Anomaly in the same area means that our loss rate estimates may have been augmented by drift losses at these particular longitudes. Nevertheless, the shaded regions in Figure 6.2 account for over one fifth of the Earth's surface between L = 2 and L = 3. Even if whistler-induced precipitation were completely absent elsewhere, a factor of five in the lifetimes listed in Table 6.1 would not affect the first-order conclusions offered herein.

Though we do not consider regions below L = 2, above L = 3, or outside the plasmapause in our lifetime estimates, whistler-associated precipitation of $>$50 keV electrons does appear to occur in these regions [*Carpenter and Inan*, 1987]; in general, however, such precipitation is more difficult to detect with our ground-based approach. Below L = 2 whistler-resonant electron energies reach into a few MeV, but the relatively small belt population of such high-energy electrons – several orders of magnitude less than that for electrons of a few hundred keV [*West et al.*, 1981] – substantially reduces the total energy of whistler-induced precipitation bursts [*Chang and Inan*, 1985]. Between L = 3 and the plasmapause, declining whistler-resonant energies and belt populations reduce the precipitation flux of $>$50 keV electrons, although the precipitation flux of lower-energy electrons increases [*Chang and Inan*, 1985]. Whistler-resonant energies in the diminished cold plasma densities beyond the plasmapause are $>$50 keV, and burst precipitation of such electrons in association with whistler-triggered emissions has been reported [*Rosenberg et al.*, 1971; *Dingle and Carpenter*, 1981; *Carpenter et al.*, 1985]; however, the relative significance of ducted whistlers, whistler-triggered emissions and spontaneous emissions such as chorus [*Burtis and Helliwell*, 1976] as belt loss processes in these regions is not known.

The evidence of a strong link between precipitation and whistler ducts supports the suggestion by *Bernhardt and Park* [1977] that ducts, once formed, may be self-reinforcing. The confinement of ionizing precipitation bursts to a small ionospheric region at the foot of the duct may increase the local ionospheric pressure above the nighttime ambient and thus help maintain the duct enhancement. The process by which ducts are initially formed is still unclear, although thunderstorms may be involved. The precipitation of 10 eV–40 keV electrons induced by nonducted whistlers above a thunderstorm [*Inan and Bell*, 1991] and electric fields from the cloud charging which precedes lightning [*Park and Helliwell*, 1971] have both been suggested to cause localized ionization adequate to form duct enhancements.

Indeed, lightning may contribute to all of the magnetospheric processes discussed in this chapter. In addition to its possible role in the formation of ducts and its triggering of belt losses via ducted whistlers, lightning may also induce losses of lower-energy electrons via nonducted whistlers [*Jasna et al.*, 1992] and has been suggested as a source of plasmaspheric hiss [*Draganov et al.*, 1992].

7

Summary and Suggestions for Future Research

7.1 SUMMARY OF EXPERIMENTAL RESULTS AND CONCLUSIONS

Detailed evidence exists of a close association between individual whistler ducts and conjugate ionospheric disturbances sensed by the perturbation of subionospheric VLF, LF, and MF signals. The evidence can be summarized as follows:

1. Even barely detectable whistlers ($\sim$2 μV/m) can be associated with ionospheric disturbances in both hemispheres.
2. A case study showed slow-onset and "overshoot" perturbation signatures to be consistent with multiple ionospheric disturbances associated one-to-one with individual components of multipath ducted whistlers.
3. Two case studies of whistler component arrival azimuths demonstrated a correspondence between duct exit locations and the locations of ionospheric disturbances inferred from configurations of perturbed subionospheric signal paths.
4. The behavior of signal perturbation onsets as a function of time compared well with predictions for conjugate precipitation pulses induced by ducted whistler scattering of radiation belt electrons.

This evidence casts lightning in the role of trigger for a magnetospheric "shotgun": for each of the multiple ducts excited simultaneously by a typical multipath whistler, there may be a series of precipitation bursts which strike the ionosphere in geomagnetically conjugate regions. Since sferics can couple into ducts over 2500 km from the source discharge [*Carpenter and Orville*, 1989], a lightning flash over Huntsville, for example, has the potential to cause localized precipitation bursts and ionospheric disturbances over the entire contiguous United States as well as over the conjugate region in the Southern Hemisphere. The occurrence of such simultaneous precipitation bursts distributed over a wide area is consistent with the satellite observation by *Voss et al.* [1984] of precipitation 2000 km west of Palmer when whistler-associated perturbations of NAA–PA suggested precipitation to the north of Palmer.

Belt losses caused by ducted whistlers can be estimated to first order, based on the hypothesis that every ducted whistler component scatters and precipitates radiation belt electrons. The lifetimes of $\sim$70 to $\sim$200 keV electrons due to this loss process appear to be similar to those estimated by *Lyons and Thorne* [1973] due to precipitation by nonducted ELF/VLF hiss, which those authors suggested was sufficient to explain radiation belt structure. Ducted whistlers may therefore play a significant role in maintaining the equilibrium of energetic radiation belt electron populations.

7.2 SUGGESTIONS FOR FUTURE RESEARCH

7.2.1 Experimental Corroboration and Diagnostic Use of Models for Subionospheric VLF Propagation and Scattering

The three-dimensional modeling of *Poulsen et al.* [1990] has lent theoretical credence to the assumption, used often in this research, that perturbations of a subionospheric signal are caused by ionospheric disturbances within 200–250 km of the signal path. While this part of the *Poulsen et al.* [1990] theory has been consistent so far with experimental data [*Inan et al.*, 1990], other aspects of the theory remain untested. The theory predicts, for example, how the magnitude and polarity of signal amplitude and phase changes will depend on the location of the disturbance relative to the signal path; yet the difficulty in experimentally establishing disturbance locations has all but prevented verification of these predictions.

The application of conjugate signal perturbation methods and identification of associated whistler ducts, as described in Chapters 4 and 5, may provide more dependable indications of disturbance location than were previously available. Combined with statistical studies of signal perturbation characteristics such as those performed by *Wolf and Inan* [1990], knowledge of disturbance locations could provide corroboration of the *Poulsen et al.* [1990] model and make possible quantitative estimates of ionospheric disturbance structure based on the amplitude and phase of observed signal perturbations.

7.2.2 Ground-Based Estimation of Electron Pitch-Angle Distributions in the Radiation Belts

The monitoring of whistlers and conjugate ionospheric disturbances may provide a means to determine the profile of the bounce and drift loss cones. As pointed out in Chapter 5, Northern Hemisphere disturbances detected before disturbances in the south could indicate a relatively large population in the northern bounce loss cone as opposed to days when the Southern Hemisphere is disturbed first. Estimates of the quantity of precipitating electrons, either from satellites or from signal perturbation data, could be compared with observed whistler strengths to evaluate the scattering "effectiveness" of whistlers from day to day, which would in turn suggest the slope of the bounce loss cone. Worldwide measurements of signal perturbation rates could indicate precipitation as a function of longitude and provide an estimate of the drift loss cone.

7.2.3 Measurements of Duct Dimensions

The average cross-sectional area of ducts (A_{duct}) was suggested in Chapter 6 to directly influence long-term electron loss rates caused by ducted-whistler-induced precipitation. Since duct area varies as the square of duct diameter, the cross-sectional dimensions of ducts exert more influence over these loss rates than any other parameter in equation (6.1). Additional measurements of duct cross-section as a function of time, geomagnetic activity and *L*-shell would therefore enable us to predict the effect of ducted whistlers on the radiation belts with greater confidence. The cross-section of ducts might be surveyed by inferring duct exit apertures from ground-observed ducted signals [*Ikeda et al.*, 1988] or by measuring the spatial extent of duct-associated precipitation from satellites [*Voss et al.*, 1984] or from ionospheric disturbances monitored on networks of long-distance subionospheric signal paths [*Inan et al.*, 1990].

A

Electron Lifetimes at L = 2.24 from a Coherent Diffusion Model

Inan [1987] introduced a "coherent diffusion coefficient" $D^c_{\alpha\alpha}$ to represent the electron pitch angle scattering efficiency of steady-state ducted whistler-mode waves, which he defined in his equation (16) as

$$D^c_{\alpha\alpha} \equiv \frac{\langle(\Delta\alpha)^2\rangle}{T_r} \tag{A.1}$$

where $\Delta\alpha$ is the net total pitch angle change for each electron, the angular brackets denoting an average over the initial electron Larmor phase, and T_r is the "resonance time," the period over which most pitch angle scattering takes place during an electron's interaction with a wave.

For scattering induced by real, transient ducted whistlers, however, pitch-angle diffusion is neither continuous nor uniformly distributed in space. We therefore introduce a temporal efficiency coefficient η_t which represents the whistler-electron interaction time occurring per unit real time:

$$\eta_t \equiv \frac{T_r}{t} \tag{A.2}$$

and a spatial efficiency coefficient η_s which represents the fraction of space occupied by a single whistler duct, defined in terms of the estimated duct area and the area of the region monitored for ducts at 100 km altitude:

$$\eta_s \equiv \frac{A_{\text{duct}}}{A_{\text{region}}}. \tag{A.3}$$

Since the lifetime τ of belt electrons diffusing in pitch angle can be approximated as $\tau \simeq 1/D_{\alpha\alpha}$ [*Schulz and Lanzerotti*, 1974], we can estimate that for whistler-induced diffusion

$$\tau \simeq \frac{1}{D^c_{\alpha\alpha}\eta_t\eta_s}. \tag{A.4}$$

To find $D^c_{\alpha\alpha}$ and η_t at L = 2.24, we must first estimate T_r. Using a parallel resonance electron velocity v_R = 1.8 × 10^8 m/s for a 136 keV whistler-resonant loss-cone electron at L = 2.24 [*Inan et al.*, 1989] in equation (15) of *Inan* [1987], we find the length of the interaction zone as 748 km. Dividing this distance by v_R gives $T_r \simeq$ 4.2 ms.

Since $D^c_{\alpha\alpha}$ as described by equation (18) of *Inan* [1987] varies directly as T_r and as the square of equatorial ducted wave field B_{dw}, and depends only weakly on other quantities such as L, we can scale the L = 4 $D^c_{\alpha\alpha}$ estimate from that paper. For B_{dw} = 1 pT and $T_r \simeq$ 52 ms, *Inan* [1987] found $D^c_{\alpha\alpha} \simeq 1.46 \times 10^{-4}$ s^{-1}. Multiplying by the square of 12 pT (the average whistler B_{dw} estimated from Figure 6.1) and by 4.2 ms/52 ms, we obtain $D^c_{\alpha\alpha} \simeq 1.70 \times 10^{-3}$ s^{-1}.

To find η_t, we multiply 4.2 ms by an annual average of 60 whistler components per minute (Table 6.1) giving $\eta_t \simeq 0.0042$. We use the value for $\eta_s \simeq 6 \times 10^{-5}$ determined earlier in this paper. Solving (A.4) gives $\tau \simeq 2.3 \times 10^9$ s or 2.7×10^4 days.

The first-order similarity between this result and the values listed in Table 6.1 is encouraging; however, it must be interpreted cautiously. *Inan* [1987] used $D^c_{\alpha\alpha}$ to represent the scattering of equatorially resonant electrons, while more comprehensive estimates of precipitated flux account for electrons that interact with the wave elsewhere along the field line. In particular, although $D^c_{\alpha\alpha}$ depends on $(B_{dw})^2$, *Inan et al.* [1982] predicted that total precipitation flux would vary linearly with B_{dw} when particle trapping is neglected (which they estimated to be a good assumption for $B_{dw} \lesssim$ 30 pT at $L \simeq$ 2.25).

B

Uncharacteristic Signal Perturbations

Unusual subionospheric signal perturbations without characteristic onset delays or onset durations were rarely found and, with the exception of the "overshoot" signatures discussed in Section 5.2, were excluded from this research. Such perturbations include "early" (onset delay $<$ 50 ms) and "fast" (onset duration $<$ 50 ms) events, which are not consistent with equatorial gyroresonant LEP models, and may be due to more direct coupling mechanisms between lightning discharges and the lower ionosphere [*Inan et al.*, 1991].

Our understanding of fast and early events may be improved by spatial and temporal comparisons with more commonly observed "Trimpi" events like those discussed in the body of the dissertation. Figure B.1 offers an example of such a comparison. The marked event, shown in greater detail by Figure B.2, appears to be a fast/early event (A) followed by a "Trimpi" event (B) on NSS–AR, while other signals, including NPM–PA in the Southern Hemisphere, experienced only a "Trimpi" event. All events appear to have resulted from the same lightning flash, whose time is indicated by the strong sferic recorded at College Park, Maryland (CP). The lack of a fast/early perturbation on NAU–CP, a signal propagating less than 50 km from NSS–AR, suggests that LEP-induced disturbances responsible for "Trimpi" events are larger than the disturbances responsible for fast/early events.

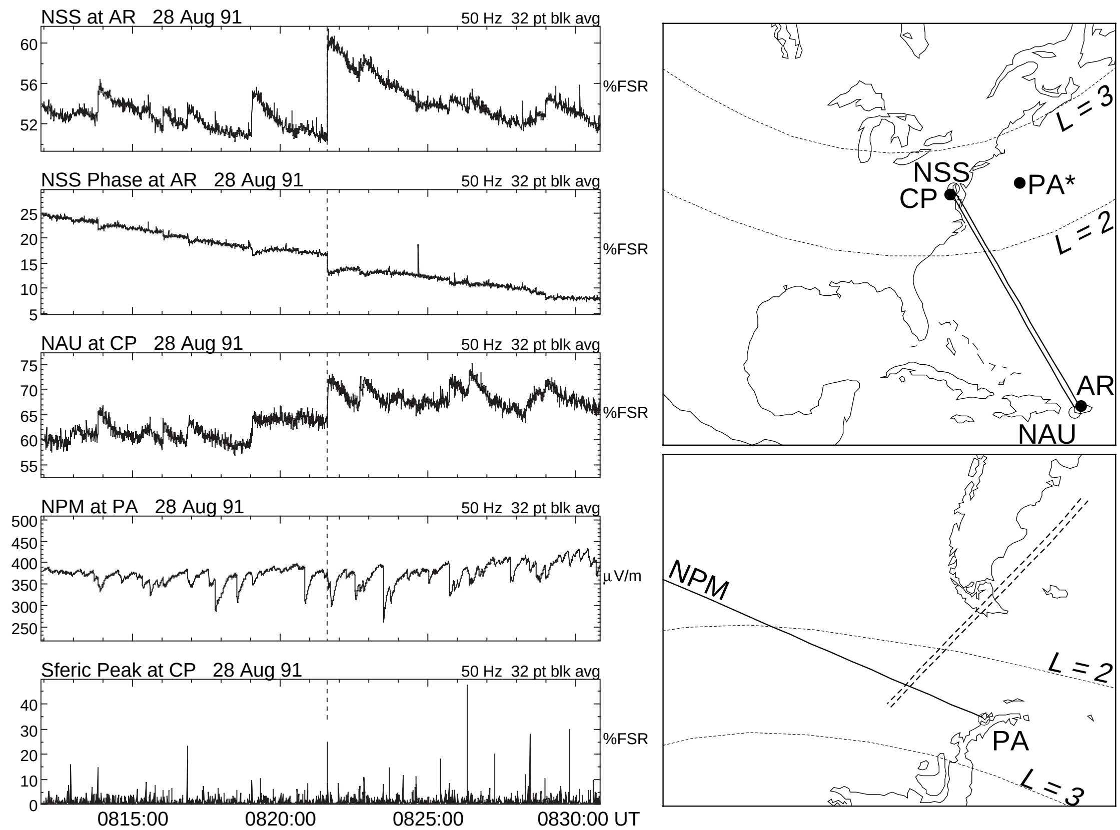

Fig. B.1. Comparing a "fast & early" event with more typical "Trimpi" events. The dashed vertical line in the left panels marks an event which is shown in greater detail by Figure B.2. The map format is the same as in Chapter 5. CP represents a receiving site at College Park, Maryland, PA* indicates the geomagnetic conjugate of Palmer Station, and other symbols are defined in Tables 3.1 and 3.2. The indicated spike in the sferic channel represents a relatively strong atmospheric observed at CP.

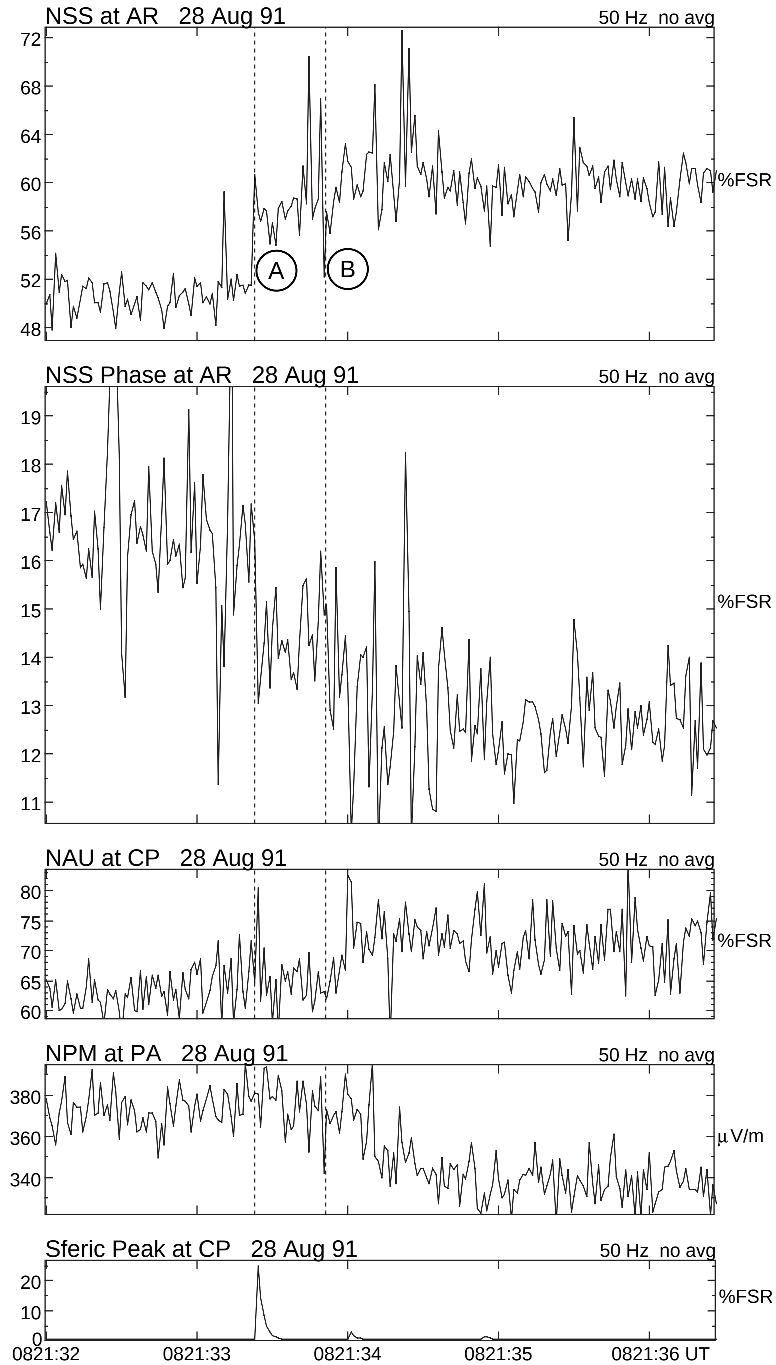

Fig. B.2. A closeup of the event marked in Figure B.1. NSS–AR was perturbed suddenly (A) at the same time as the lightning flash which generated the sferic. NSS–AR was perturbed again a few tenths of a second later (B), this time along with the other signal channels shown, in a “Trimpi” event typical of those discussed in the body of the dissertation.

C

Arrival Azimuth Behavior of Narrowband Signals

The development for this research of a digital broadband VLF direction finding technique invited its application to narrowband signals. The arrival azimuths of signals such as NPM–PA contain potentially significant information on subionospheric VLF propagation, especially in the presence of ionospheric disturbances. This appendix presents a preliminary analysis of perturbed NPM–PA arrival azimuth behavior.

To estimate the maximum likely change in NPM–PA arrival azimuth, a model was constructed based on the assumption that the original and scattered signals arriving at Palmer propagated horizontally as single mode plane waves. For convenience of analysis, one of the two orthogonal antennas ($\hat{\mathbf{x}}$) was assumed to be aligned for maximum reception of NPM, the other ($\hat{\mathbf{y}}$) to null NPM. Under these circumstances the original field picked up by the antennas, in phasor notation, would be simply $\hat{\mathbf{x}}H_{x_0}$. The scattered field, arriving from the scattering region with phase θ_s, appears as $\hat{\mathbf{x}}H_{x_1}e^{j\theta_s} + \hat{\mathbf{y}}H_{y_1}e^{j\theta_s}$ giving a total field of

$$H = \hat{\mathbf{x}}(H_{x_0} + H_{x_1}e^{j\theta_s}) + \hat{\mathbf{y}}(H_{y_1}e^{j\theta_s}). \tag{C.1}$$

This is the expression for a polarization ellipse. Given the location of a scattering center relative to the signal path, H_{x_1} and H_{y_1} can be determined as a function of H_{x_0} using trigonometry and the forward scattering attenuation given for mode 1 in Figure 4.8 of *Poulsen* [1991].

When a scattering center is present, the magnitude and angle of the major axis of the polarization ellipse can change. These changes were calculated for 750 different scattering center locations between 500 and 3000 km away from Palmer along the NPM–PA path and between 10 and 300 km off the NPM–PA path to its northern side. At each location the model used 100 values of scattered signal strength, ranging from 5 to 15 dB less attenuation than that given in Figure 4.8 of *Poulsen* [1991]. The results are summarized in Figure C.1.

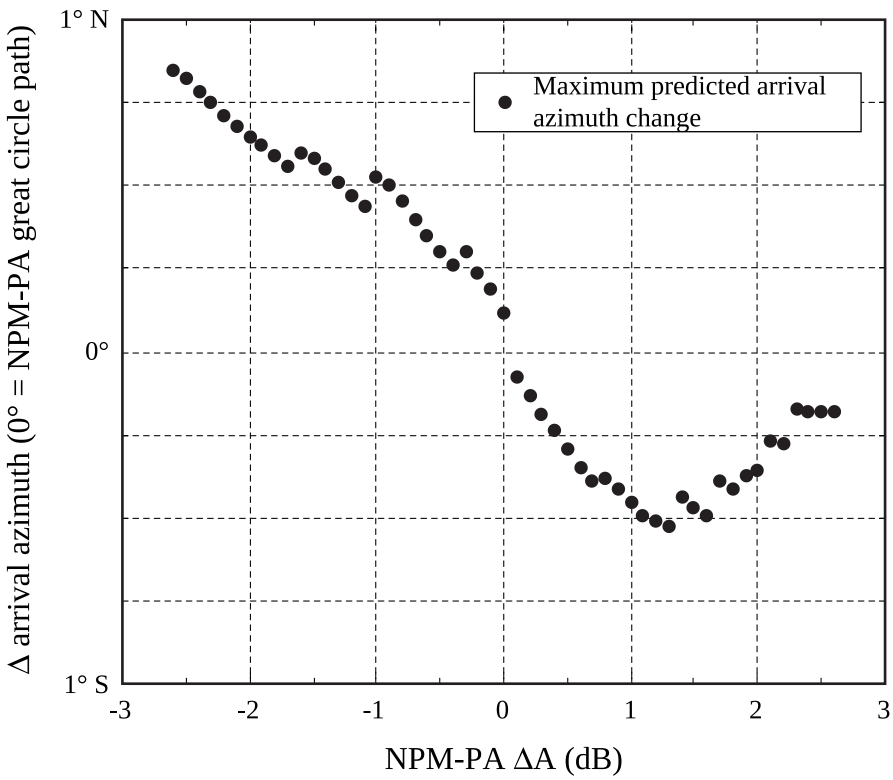

Fig. C.1. Maximum NPM–PA arrival azimuth changes as a function of observed signal perturbation size. The figure shows the maximum changes of signal azimuth predicted by the model discussed in the text for disturbances located to the north of the NPM–PA signal path.

These preliminary results suggest that, even for large amplitude changes, the arrival azimuth of NPM–PA is unlikely to change by more than one degree. It is also interesting

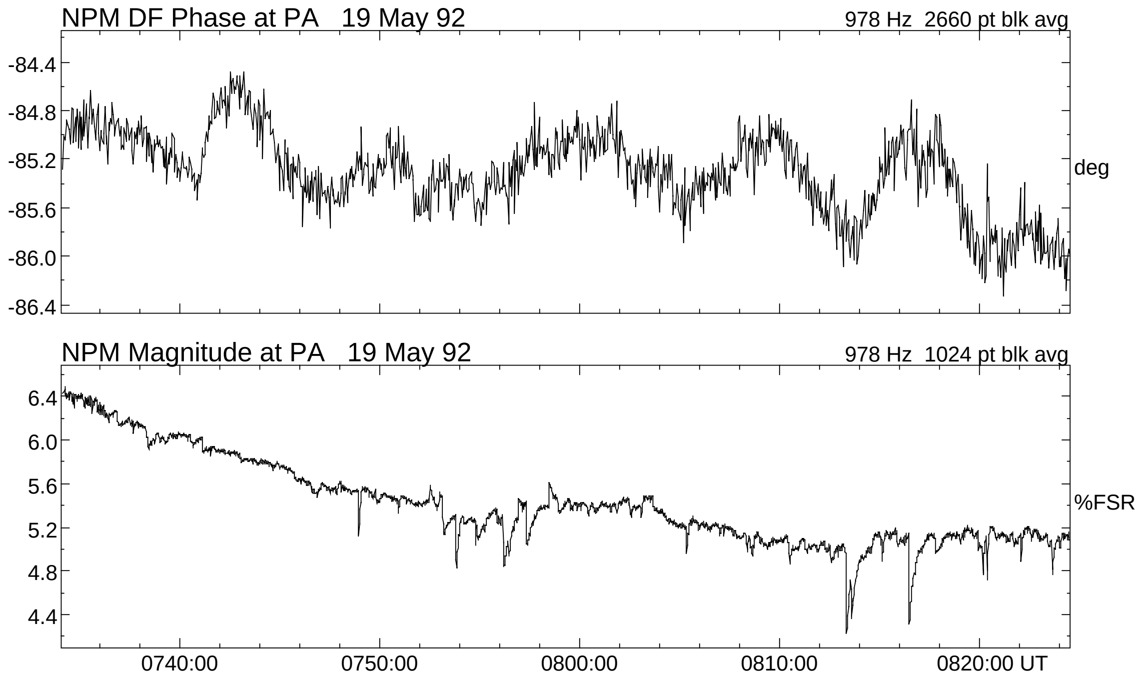

Fig. C.2. Fifty minutes of NPM–PA arrival azimuth and total magnitude observed with crossed loop antennas on May 19, 1992. The largest magnitude changes occurred during the later portion and are expanded in Figure C.3. The great-circle arrival azimuth of NPM at Palmer is -84.1°, and the offset due to antenna orientation is ±5°. "DF Phase" indicates arrival azimuth, measured in degrees; magnitude is expressed in percent of the full scale range of the analyzing equipment.

that scattering centers to the north of the signal path could cause azimuth changes to the south in association with upgoing amplitude changes.

Figure C.2 shows observed variations of NPM–PA arrival azimuth and magnitude. Although no associations between the two characteristics are obvious, the ~8 min fluctuations in arrival azimuth are surprising and may indicate ionospheric effects which do not strongly affect signal strength.

The lack of azimuth perturbations (Figure C.3) is not inconsistent with the simple model used here. Many possible scattering center locations would not result in arrival azimuth changes, most notably those directly on the NPM–PA path. Future work in this area should involve full use of *Poulsen*'s [1991] model and a statistically significant number of observations.

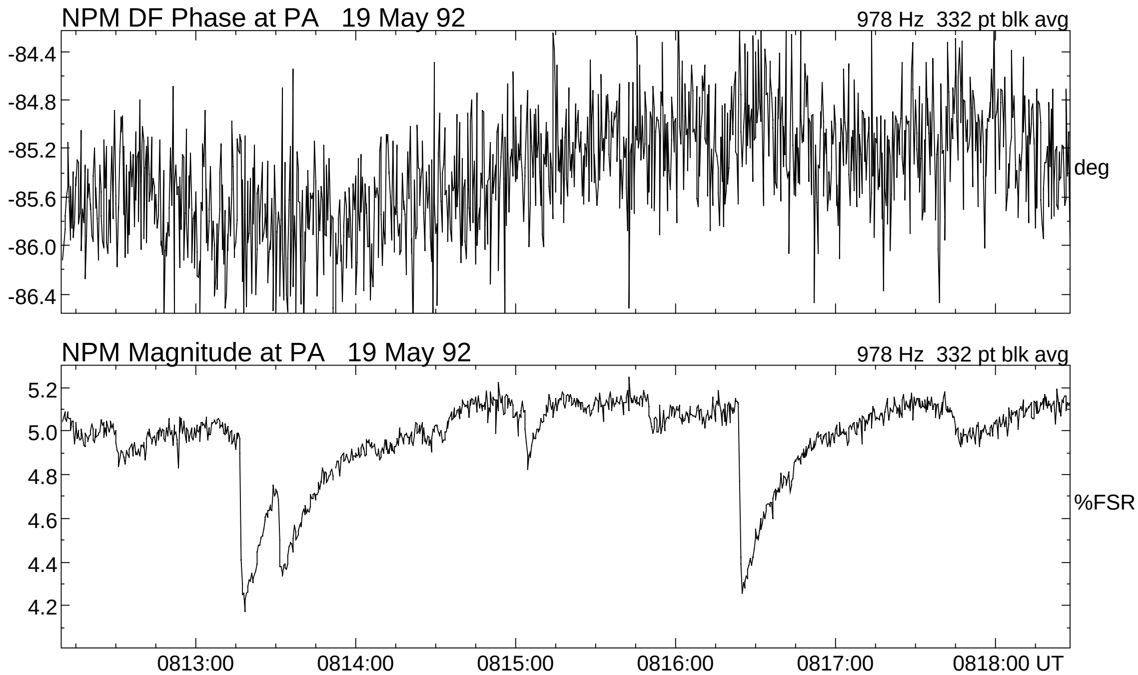

Fig. C.3. Six minutes of NPM–PA arrival azimuth and total magnitude observations expanded from Figure C.2. The two largest magnitude perturbations shown were about -1.5 dB. The maximum arrival azimuth perturbation expected from Figure C.1 would be 0.6°. No corresponding azimuth perturbations are evident; closer examination of the apparent azimuth perturbation at about 0816:20 UT shows it to be unrelated to the magnitude perturbation. "DF Phase" indicates arrival azimuth, measured in degrees; magnitude is expressed in percent of the full scale range of the analyzing equipment.

D

“MacTrimpi” Sampled Data Format

For ease of manipulation by different programs and computer hardware, sampled data used in this research was stored in what has come to be known as the “MacTrimpi” format. Files in this format are composed of a 512-byte header followed by an arbitrarily long sequence of 16-bit signed integers. The header consists entirely of ASCII bytes, so that it may be listed or modified with general-purpose file examination programs, and so that it can be transferred easily between byte-swapped and non-byte-swapped computers. Although 512 bytes are reserved for the header, much of that space is currently unused and available for the addition of future fields. The “MacTrimpi” header is defined by a C language include file (also called a “header” or “.h” file) titled *datafile.h*. This file is reproduced below.

```
/*
* datafile.h -- header format for standard digitized data files.
*/

/*
* If this is being compiled under THINK C, turn off the idiotic
* default that aligns character arrays to 16-bit word boundaries
* under THINK C 5.0.
*/
#ifdef THINK_C
#pragma options (!align_arrays)
#endif

/*
* these define possible values for the typemark field of the
* header.
*/
#define AMPLITUDE  'A'
#define PHASE      'P'
```

```
#define REFERENCE  'R'
#define SPECIAL    'S'  /* special or unknown */
#define PEAKDETECT 'D'  /* from peak detector */
#define DUMMY      ' '  /* invalid data! */
#define NOINFO     '\0' /* no information -- data possibly
                           from some old version of software
                           or from stripped-down software...*/
/*
* swapping types
*/
#define SWAPPED    'S'
#define UNSWAPPED  'U'

/*
* signing types
*/
#define SIGNED     'S'
#define UNSIGNED   'U'

/*
* calibration types
*
* If uncalibrated all other calibration-related fields are to be
* ignored and may contain garbage. If either max or min values
* are calibrated then the corresponding field should be a reasonable
* floating point number.
*/
#define CALIBRATED        'C'
#define UNCALIBRATED      'U'
#define ONLYMINCALIBRATED 'N'
#define ONLYMAXCALIBRATED 'X'

/*
* For portability (and type-ability) the header is made up entirely
* of ascii bytes. For ease of reading with scanf all strings are
* null-terminated. All numbers, including floating point numbers,
* are written as null terminated strings, e.g. "0.401".
*
* If a field is incompletely filled by characters or digits, the rest
* of the field is to be filled with nulls ('\0').
*
* There are some single-character fields. These are not read as
* strings and thus do not have null-termination.
*
* The "DATA\0\0\0\0" identifier in the beginning is for programs
* which read these files to know that this file has a header.
*
* The option for additional headers is application-specific. Standard
* programs should be able to skip over any additional headers without
* breaking. Additional headers might simply contain text to explain
* the following data in greater detail. Some programs might wish
* to allow the user to add explanation headers after looking at the
* data.
*/
```

```
struct datafilehdr {
  char magicstring[8], /* identifier, should be "DATA\0\0\0\0" */
       totalhdrs[3],   /* total number of 512-byte headers
                          incl. this one. (null-terminated ascii) */
       abbrev[8],      /* 7 char abbreviation for title if any */
       stationcode[3], /* 2 char station code (PA, SU, etc.) */
       title[82],      /* where the recording was made/title */
       month[3],       /* numeric WITH ZERO PLACEHOLDER,
                          e.g. 03 = march, 10 = october, etc. */
       day[3],         /* numeric with zero placeholder */
       year[5],        /* full year, eg 1987 */
       hours[3],       /* numeric with zero placeholder */
       minutes[3],     /* numeric with zero placeholder */
       seconds[3],     /* numeric with zero placeholder */
       msec[4],        /* milliseconds later than above time,
                          again with zero placeholders */
       sampling_period[15],/* floating point number in seconds */
       samplebits[3],  /* BITS per data sample (e.g., "12") --
                          this establishes min/max values */
       wordsize[2],    /* bytes reserved per data sample("1","2"...)*/
       typemark,       /* see data type #defines above */
       swapping,       /* see swapping type #defines */
       signing,        /* see signing type #defines */
       caltype,        /* see calibration type #defines */
       calmin[15],     /* floating point min value if calibrated */
       calmax[15],     /* floating point max value if calibrated */
       calunits[40],   /* null-terminated units string (eg "volts")*/
       recordsize[6],  /* bytes to get in single read, usually 512 */
       fill[(512-228)];/* round out header to 512 bytes total.
                          This region should not be filled with
                          anything but nulls, so that later
                          versions of this header will be
                          compatible. Any text comments should
                          be placed in additional headers. */
};
```

Bibliography

Allen, J., L. Frank, H. Sauer, and P. Reiff, Effects of the March 1989 solar activity, *EOS, 70*, 1479, 1989.

Andrews, M. K., Delayed storm-time increases in the whistler rate at mid-latitudes, *J. Atmos. Terr. Phys., 37*, 1423, 1975.

Angerami, J. J., Whistler duct properties deduced from VLF observations made with the Ogo 3 satellite near the magnetic equator, *J. Geophys. Res., 75*, 6115, 1970.

Angerami, J. J., and J. O. Thomas, Studies of planetary atmospheres 1. the distribution of electrons and ions in the Earth's exosphere, *J. Geophys. Res., 69*, 4537, 1964.

Baum, A., Antarctic study tests radio noise, *New York Times*, p. 42, November 26, 1963.

Bell, T. F., W. L. Poulsen, and U. S. Inan, Subionospheric VLF signal variations due to large D-region perturbations caused by precipitating electron bursts, paper presented at the XXIII General Assembly, URSI, Prague, 24 Aug.–5 Sep., 1990.

Berger, M. J., S. M. Seltzer, and K. Maeda, Some new results on electron transport in the atmosphere, *J. Atmos. Terr. Phys., 36*, 591, 1974.

Bernard, L. C., A new nose extension method for whistlers, *J. Atmos. Terr. Phys., 35*, 871, 1973.

Bernhardt, P. A., and C. G. Park, Protonospheric-ionospheric modeling of VLF ducts, *J. Geophys. Res., 82*, 5222, 1977.

Budden, K. G., *The Propagation of Radio Waves*, Cambridge University Press, Cambridge, 1985.

Bullough, K., and J. L. Sagredo, VLF goniometer observations at Halley Bay, Antarctica–I. The equipment and the measurement of signal bearing, *Planet. Space Sci.*, *21*, 899, 1973.

Burgess, W. C., and U. S. Inan, Simultaneous disturbance of conjugate ionospheric regions in association with individual lightning flashes, *Geophys. Res. Lett.*, *17*, 259, 1990.

Burtis, W. J., and R. A. Helliwell, Magnetospheric chorus: occurrence patterns and normalized frequency, *Planet. Space Sci.*, *24*, 1007, 1976.

Carlson, A. B., *Communication Systems*, McGraw-Hill, New York, 1986.

Carpenter, D. L, and R. R. Anderson, An ISEE/whistler model of equatorial electron density in the magnetosphere, *J. Geophys. Res.*, *97*, 1097, 1992.

Carpenter, D. L., and U. S. Inan, Seasonal, latitudinal and diurnal distributions of whistler-induced particle precipitation events, *J. Geophys. Res.*, *92*, 3429, 1987.

Carpenter, D. L., and J. W. LaBelle, A study of whistlers correlated with bursts of electron precipitation near $L = 2$, *J. Geophys. Res.*, *87*, 4427, 1982.

Carpenter, D. L., and R. E. Orville, The excitation of active whistler mode signal paths in the magnetosphere by lightning: two case studies, *J. Geophys. Res.*, *94*, 8886, 1989.

Carpenter, D. L., and R. L. Smith, Whistler measurements of electron density in the magnetosphere, *Rev. Geophys.*, *2*, 415, 1964.

Carpenter, D. L., U. S. Inan, M. L. Trimpi, R. A. Helliwell, and J. P. Katsufrakis, Perturbations of subionospheric LF and MF signals due to whistler-induced electron precipitation bursts, *J. Geophys. Res.*, *89*, 9857, 1984.

Carpenter, D. L., U. S. Inan, E. W. Paschal, and A. J. Smith, A new VLF method for studying burst precipitation near the plasmapause, *J. Geophys. Res.*, *90*, 4383, 1985.

Chang, H. C., and U. S. Inan, A theoretical model study of observed correlations between whistler mode waves and energetic electron precipitation events in the magnetosphere, *J. Geophys. Res.*, *88*, 10053, 1983.

Chang, H. C., and U. S. Inan, Lightning-induced electron precipitation from the magnetosphere, *J. Geophys. Res.*, *90*, 1531, 1985.

Cornwall, J. M., Scattering of energetic trapped electrons by very-low-frequency waves, *J. Geophys. Res., 69*, 1251, 1964.

Cousins, M. D., Direction finding on whistlers and related VLF signals, *Tech. Rep. 3432–2*, Stanford Electronics Laboratories, Stanford, Calif., 1972.

Crary, J. H., The effect of the Earth-ionosphere waveguide on whistlers, *Tech. Rep. 9*, Stanford Electronics Laboratories, Stanford, Calif., 1961.

Daniell, G. J., Approximate dispersion formulæ for whistlers, *J. Atmos. Terr. Phys., 48*, 267, 1986*a*.

Daniell, G. J., Analytic properties of the whistler dispersion function, *J. Atmos. Terr. Phys., 48*, 271, 1986*b*.

Davies, K., *Ionospheric Radio Propagation*, Dover Publications, New York, 1966.

Dingle, B., Burst precipitation of energetic electrons from the magnetosphere, Ph.D. thesis, Stanford University, Stanford, Calif., 1977.

Dingle, B., and D. L. Carpenter, Electron precipitation induced by VLF noise bursts at the plasmapause and detected at conjugate ground stations, *J. Geophys. Res., 86*, 4597, 1981.

Dowden, R. L., and C. D. D. Adams, Phase and amplitude perturbations on the NWC signal at Dunedin from lightning-induced electron precipitation, *J. Geophys. Res., 94*, 497, 1989.

Dowden, R. L., and C. D. D. Adams, Location of lightning-induced electron precipitation from measurement of VLF phase and amplitude perturbations on spaced antennas and on two frequencies, *J. Geophys. Res., 95*, 4135, 1990.

Draganov, A. B., U. S. Inan, V. S. Sonwalkar, and T. F. Bell, Magnetospherically reflected whistlers as a source of plasmaspheric hiss, *Geophys. Res. Lett., 19*, 233, 1992.

Dungey, J. W., Loss of Van Allen electrons due to whistlers, *Planet. Space Sci., 11*, 591, 1963.

Edgar, B. C., The upper and lower frequency cutoffs of magnetospherically reflected whistlers, *J. Geophys. Res., 81*, 205, 1976.

Gilbert, W., *De magnete, magneticisque corporibus, et de magno magnete tellure physiologia nova*, London, 1600.—Gilbert Club revised English translation, Chiswick Press, London, 1900.

Gledhill, J. A., The effective recombination coefficient of electrons in the ionosphere between 50 and 150 km, *Radio Sci.*, *21*, 399, 1986.

Glukhov, V. S., V. P. Pasko, and U. S. Inan, Relaxation of transient lower ionospheric disturbances caused by lightning-whistler-induced electron precipitation bursts, *J. Geophys. Res.*, *97*, 16971, 1992.

Goldberg, R. A., S. A. Curtis, and J. R. Barcus, Detailed spectral structure of magnetospheric electron bursts precipitated by lightning, *J. Geophys. Res.*, *92*, 2505, 1987.

Gurnett, D. A., and U. S. Inan, Plasma wave observations with the Dynamics Explorer 1 spacecraft, *Rev. Geophys.*, *26*, 285–316, 1988.

Helliwell, R. A., *Whistlers and Related Ionospheric Phenomena*, Stanford University Press, Stanford, Calif., 1965.

Helliwell, R. A., J. P. Katsufrakis, and M. L. Trimpi, Whistler-induced amplitude perturbation in VLF propagation, *J. Geophys. Res.*, *78*, 4679, 1973.

Helliwell, R. A., T. Mielke, and U. S. Inan, Rapid whistler-mode wave growth resulting from frequency-time curvature, *Geophys. Res. Lett.*, *17*, 599–602, 1990.

Horner, F., The accuracy of the location of sources of atmospherics by radio direction-finding, *Proc. IEE*, *101(III)*, 383–390, 1954.

Ikeda, M., K. Tsuruda, and S. Machida, Exit areas of VLF waves inferred from the multistation measurements at Roberval, Canada, *J. Geomag. Geoelectr.*, *40*, 227–259, 1988.

Inan, U. S., Non-linear gyroresonant interactions of energetic particles and coherent VLF waves in the magnetosphere, *Tech. Rep. 3414–3*, Stanford Electronics Laboratories, Stanford, Calif., 1977.

Inan, U. S., Gyroresonant pitch angle scattering by coherent and incoherent whistler mode waves in the magnetosphere, *J. Geophys. Res.*, *92*, 127, 1987.

Inan, U. S., and T. F. Bell, Pitch angle scattering of energetic particles by oblique whistler waves, *Geophys. Res. Lett.*, *18*, 49, 1991.

Inan, U. S., and D. L. Carpenter, On the correlation of whistlers and associated subionospheric VLF/LF perturbations, *J. Geophys. Res.*, *91*, 3106, 1986.

Inan, U. S., and D. L. Carpenter, Lightning-induced electron precipitation events observed at $L \sim 2.4$ as phase and amplitude perturbations on subionospheric VLF signals, *J. Geophys. Res.*, *92*, 3293, 1987.

Inan, U. S., T. F. Bell, and H. C. Chang, Particle precipitation induced by short-duration VLF waves in the magnetosphere, *J. Geophys. Res.*, *87*, 6243, 1982.

Inan, U. S., H. C. Chang, and R. A. Helliwell, Electron precipitation zones around major ground-based VLF signal sources, *J. Geophys. Res.*, *89*, 2891, 1984.

Inan, U. S., D. L. Carpenter, R. A. Helliwell, and J. P. Katsufrakis, Subionospheric VLF/LF phase perturbations produced by lightning-whistler induced particle precipitation, *J. Geophys. Res.*, *90*, 7457, 1985*a*.

Inan, U. S., H. C. Chang, R. A. Helliwell, W. L. Imhof, J. B. Reagan, and M. Walt, Precipitation of radiation belt electrons by man-made waves: a comparison between theory and measurement, *J. Geophys. Res.*, *90*, 359, 1985*b*.

Inan, U. S., W. C. Burgess, T. G. Wolf, and D. C. Shafer, Lightning-associated precipitation of MeV electrons from the inner radiation belt, *Geophys. Res. Lett.*, *15*, 172, 1988*a*.

Inan, U. S., D. C. Shafer, and W. Y. Yip, Subionospheric VLF signatures of nighttime D region perturbations in the vicinity of lightning discharges, *J. Geophys. Res.*, *93*, 11,455, 1988*b*.

Inan, U. S., T. G. Wolf, and D. L. Carpenter, Geographic distribution of lightning-induced electron precipitation observed as VLF/LF perturbation events, *J. Geophys. Res.*, *93*, 9841, 1988*c*.

Inan, U. S., M. Walt, H. D. Voss, and W. L. Imhof, Energy spectra and pitch angle distributions of lightning-induced electron precipitation: analysis of an event observed on the S81-1 (SEEP) satellite, *J. Geophys. Res.*, *94*, 1379, 1989.

Inan, U. S., F. A. Knifsend, and J. Oh, Subionospheric VLF "imaging" of lightning-induced electron precipitation from the magnetosphere, *J. Geophys. Res.*, *95*, 17,217, 1990.

Inan, U. S., T. F. Bell, and J. V. Rodriguez, Heating and ionization of the lower ionosphere by lightning, *Geophys. Res. Lett.*, *18*, 705, 1991.

Jasna, D., U. S. Inan, and T. F. Bell, Equatorial gyroresonance between electrons and magnetospherically reflected whistlers, *Geophys. Res. Lett.*, *17*, 1865–1868, 1990.

Jasna, D., U. S. Inan, and T. F. Bell, Precipitation of suprathermal (100 eV) electrons by oblique whistler waves, *Geophys. Res. Lett., 19*, 1639–1642, 1992.

Klobuchar, J. A., and P. H. Doherty, The statistics of ionospheric time delay for GPS ranging on L1, *Proc. ION GPS-90, Third International Technical Meeting of the Satellite Division of The Institute of Navigation*, pp. 161–168, September 19–21, 1990.

Laaspere, T., M. G. Morgan, and W. C. Johnson, Some results of five years of whistler observations from Labrador to Antarctica, *Proc. IEEE, 51*, 554, 1963.

Leavitt, M. K., A frequency-tracking direction finder for whistlers and other very low frequency signals, *Tech. Rep. 3456–2,* Stanford Electronics Laboratories, Stanford, Calif., 1975.

Leavitt, M. K., D. L. Carpenter, N. T. Seely, R. R. Padden, and J. H. Doolittle, Initial results from a tracking receiver direction finder for whistler mode signals, *J. Geophys. Res., 83*, 1601, 1978.

Lohrey, B., and A. B. Kaiser, Whistler-induced anomalies in VLF propagation, *J. Geophys. Res., 84*, 5122, 1979.

Lyons, L. R., and R. M. Thorne, Equilibrium structure of radiation belt electrons, *J. Geophys. Res., 78*, 2142, 1973.

Lyons, L. R., and D. J. Williams, The quiet time structure of energetic (35–560 keV) radiation belt electrons, *J. Geophys. Res., 80*, 943, 1975*a*.

Lyons, L. R., and D. J. Williams, The storm and poststorm evolution of energetic (35–560 keV) radiation belt electron distributions, *J. Geophys. Res., 80*, 3985, 1975*b*.

Lyons, L. R., and D. J. Williams, *Quantitative Aspects of Magnetospheric Physics*, D. Riedel Publishing Co., Dordrecht, 1984.

Lyons, L. R., R. M. Thorne, and C. F. Kennel, Pitch-angle diffusion of radiation belt electrons within the plasmasphere, *J. Geophys. Res., 77*, 3455, 1972.

Matthews, S. W., Antarctica's nearer side, *National Geographic, 140*, 622–655, November 1971.

McIlwain, C. E., Coordinates for mapping the distribution of magnetically trapped particles, *J. Geophys. Res., 66*, 3681, 1961.

Merrill, R. T., and M. W. McElhinney, *The Earth's Magnetic Field*, Academic Press, London, 1983.

Mihovilović, D., and R. N. Bracewell, Whistler analysis in the time-frequency plane using chirplets, *J. Geophys. Res., 97*, 17199, 1992.

Nagano, I., and M. Mambo, An evaluation of systematic errors in VLF direction findings via full-wave analysis, *Electronics and Communications in Japan, Part 1 (Communications), 72*, 88–98, 1989.

Okada, T., A. Iwai, and M. Hayakawa, The measurement of incident and azimuthal angles and the polarization of whistlers at low latitudes, *Planet. Space Sci., 25*, 233, 1977.

Orville, R. E., and D. W. Spencer, Global lightning flash frequency, *Mon. Weather Rev., 107*, 934, 1979.

Orville, R. E., R. W. Henderson, and L. F. Bosart, An East Coast lightning detection network, *Bull. Am. Meteorol. Soc., 64*, 1029, 1983.

Park, C. G., and R. A. Helliwell, The formation by electric fields of field-aligned irregularities in the magnetosphere, *Radio Sci., 6*, 299, 1971.

Parkinson, W. D., *Introduction to Geomagnetism*, Elsevier, New York, 1982.

Paschal, E. W., Palmer Station VLF receiving system characteristics (internal report), Stanford Electronics Laboratories, Stanford, Calif., 1977.

Paschal, E. W., The design of broad-band VLF receivers with air-core loop antennas (internal report), Stanford Electronics Laboratories, Stanford, Calif., 1988.

Poulsen, W. L., Modeling of very low frequency wave propagation and scattering within the Earth-ionosphere waveguide in the presence of lower ionospheric disturbances, Ph.D. thesis, Stanford University, Stanford, Calif., 1991.

Poulsen, W. L., T. F. Bell, and U. S. Inan, Three-dimensional modeling of subionospheric VLF propagation in the presence of localized *D* region perturbations associated with lightning, *J. Geophys. Res., 95*, 2355, 1990.

Poulsen, W. L., U. S. Inan, and T. F. Bell, A multiple-mode three-dimensional model of VLF propagation in the Earth-ionosphere waveguide in the presence of localized D Region disturbances, *J. Geophys. Res., 98*, 1705, 1993.

Press, W. H., B. P. Flannery, S. A. Teukolsky, and W. T. Vetterling, *Numerical Recipes in C: The Art of Scientific Computing*, pp. 542–547, Cambridge University Press, Cambridge, 1988.

Ratcliffe, J. A., *An Introduction to the Ionosphere and Magnetosphere*, Cambridge University Press, Cambridge, 1972.

Rees, M. H., Auroral ionization and excitation by incident energetic electrons, *Planet. Space Sci.*, *11*, 1209, 1963.

Rodriguez, J. V., U. S. Inan, and T. F. Bell, *D* region disturbances caused by electromagnetic pulses from lightning, *Geophys. Res. Lett.*, *19*, 2067–2070, 1992.

Roederer, J. G., *Dynamics of Geomagnetically Trapped Radiation*, Springer-Verlag, Berlin, 1970.

Rosenberg, T. J., R. A. Helliwell, and J. P. Katsufrakis, Electron precipitation associated with discrete very low frequency emissions, *J. Geophys. Res.*, *76*, 8445, 1971.

Rycroft, M. J. , Enhanced energetic electron intensities at 100 km altitude and a whistler propagating through the plasmasphere, *Planet. Space Sci.*, *21*, 239, 1973.

Sagredo, J. L., and K. Bullough, VLF goniometer observations at Halley Bay, Antarctica–II. magnetospheric structure deduced from whistler observations, *Planet. Space Sci.*, *21*, 913, 1973.

Schulz, M., and L. J. Lanzerotti, *Particle Diffusion in the Radiation Belts*, Springer-Verlag, Berlin, 1974.

Shafer, D. C., Trimpi data system – software users guide (internal report), Stanford Electronics Laboratories, Stanford, Calif., 1988.

Shawhan, S. D., D. A. Gurnett, D. L. Odem, R. A. Helliwell, and C. G. Park, The plasma wave and quasi-static electric field instrument (PWI) for Dynamics Explorer-A, *Space Sci. Instrum.*, *5*, 535, 1981.

Smith, A. J., and K. H. Yearby, AVDAS – a microprocessor-based VLF signal acquisition, processing and spectral analysis facility for Antarctica, *Br. Antarct. Surv. Bull.*, No. 75, 1–15, 1987.

Smith, E. J., A. M. A. Frandsen, B. T. Tsurutani, R. M. Thorne, and K. W. Chan, Plasmaspheric hiss intensity variations during magnetic storms, *J. Geophys. Res.*, *79*, 2507, 1974.

Stern, D. P., and N. A. Tsyganenko, Uses and limitations of the Tsyganenko magnetic field models, *EOS, 73*, 489, 1992.

Storey, L. R. O., An investigation of whistling atmospherics, Ph.D. thesis, Cambridge University, Cambridge, 1953.

Strangeways, H. J., Systematic errors in VLF direction-finding of whistler ducts, I, *J. Atmos. Terr. Phys., 42*, 995, 1980.

Strangeways, H. J., The upper cut-off frequency of nose whistlers and implications for duct structure, *J. Atmos. Terr. Phys., 53*, 151, 1991.

Strangeways, H. J., and M. J. Rycroft, Systematic errors in VLF direction-finding of whistler ducts, II, *J. Atmos. Terr. Phys., 42*, 1009, 1980.

Strangeways, H. J., M. J. Rycroft, and M. J. Jarvis, Multi-station VLF direction-finding measurements in eastern Canada, *J. Atmos. Terr. Phys., 44*, 509, 1982.

Swanson, E. R., Omega, *Proc. IEEE, 71*, 1140, 1983.

Taranenko, Y. N., U. S. Inan, and T. F. Bell, Optical signatures of lightning-induced heating of the *D* region, *Geophys. Res. Lett., 19*, 1815–1818, 1992.

Tarcsai, Gy., Routine whistler analysis by means of accurate curve fitting, *J. Atmos. Terr. Phys., 37*, 1447, 1975.

Tkalcevic, S., Very-low frequency signals (2–10 kHz) received at Palmer Station, Antarctica, from the 21.4 km dipole antenna at Siple Station, 1400 km distant, *J. Atmos. Terr. Phys., 45*, 353–367, 1983.

Tsuruda, K., and K. Hayashi, Direction finding technique for elliptically polarized VLF electromagnetic waves and its application to the low-latitude whistlers, *J. Atmos. Terr. Phys., 37*, 1193–1202, 1975.

Tsuruda, K., and M. Ikeda, Comparison of three different types of VLF direction-finding techniques, *J. Geophys. Res., 84*, 5325, 1979.

Tsuruda, K., S. Machida, T. Terasawa, A. Nishida, and K. Maezawa, High spatial attenuation of the Siple transmitter signal and natural VLF chorus observed at ground-based chain stations near Roberval, Quebec, *J. Geophys. Res., 87*, 742, 1982.

Tsyganenko, N. A., A magnetospheric magnetic field model with a wrapped tail current sheet, *Planet. Space Sci., 37*, 5, 1989.

Uman, M. A., *The Lightning Discharge*, Academic Press, Orlando, 1987.

Vampola, A. L., Electron precipitation in the vicinity of a VLF transmitter, *J. Geophys. Res.*, *92*, 4525, 1987.

Van Allen, J. A., C. E. McIlwain, and G. H. Ludwig, Radiation observations with satellite 1958ϵ, *J. Geophys. Res.*, *64*, 271, 1959.

Voss, H. D., W. L. Imhof, M. Walt, J. Mobilia, E. E. Gaines, J. B. Reagan, U. S. Inan, R. A. Helliwell, D. L. Carpenter, J. P. Katsufrakis, and H. C. Chang, Lightning-induced electron precipitation, *Nature*, *312*, 740, 1984.

Watts, J. M., Direction findings on whistlers, *J. Geophys. Res.*, *64*, 2029, 1959.

Wave Propagation Standards Committee, *IEEE Standard Definitions of Terms for Radio Wave Propagation, ANSI/IEEE Std 211-1977*, The Institute of Electrical and Electronics Engineers, New York, 1977.

West, H. I., Jr., R. M. Buck, and G. T. Davidson, The dynamics of energetic electrons in the Earth's outer radiation belt during 1968 as observed by the Lawrence Livermore National Laboratory's spectrometer on Ogo 5, *J. Geophys. Res.*, *86*, 2111, 1981.

Wolf, T. G., Remote sensing of ionospheric effects associated with lightning using very low frequency radio signals, Ph.D. thesis, Stanford University, Stanford, Calif., 1990.

Wolf, T. G., and U. S. Inan, Path-dependent properties of subionospheric VLF amplitude and phase perturbations associated with lightning, *J. Geophys. Res.*, *95*, 20997, 1990.

Yip, W.-Y., U. S. Inan, and R. E. Orville, On the spatial relationship between lightning discharges and propagation paths of perturbed subionospheric VLF/LF signals, *J. Geophys. Res.*, *96*, 249, 1991.